UNIVERSITY OF CALIFORNIA,
IRVINE

The Search for New Resonant Phenomena using Dijet Events at the ATLAS Detector

DISSERTATION

submitted in partial satisfaction of the requirements
for the degree of

DOCTOR OF PHILOSOPHY

in Physics

by

Meghan Frate

Dissertation Committee:
Professor Daniel Whiteson, Chair
Professor Tim Tait
Professor Steven Barwick

2017

DEDICATION

To Darren

TABLE OF CONTENTS

LIST OF FIGURES

LIST OF TABLES

ACKNOWLEDGMENTS

I would like to thank... The Department of Energy (DE-SC0009920) for funding my ATLAS research. My advisor Daniel, for all his guidance and support, and creating such a creative and inquisitive group at UCI. Kyle for his mentorship and wisdom, and DIANA-HEP (funding through NSF ACI-1450310) for the funding to create a lasting impact on the field. My UCI crew for their friendship, support, and pizza pockets. My WIPA crew for helping change the world one department at a time. My parents for giving me the opportunity to pursue my dreams. Dom, for being my best friend and support system, and inspiring me every day. And Darren, for following me across the country, always being there when I get back from my adventures, and doing whatever it takes to make my dreams come true. I wouldn't have made it without your love and support.

CURRICULUM VITAE

Meghan Frate

EDUCATION

Doctor of Philosophy in Physics **2017**
University of California, Irvine *Irvine, CA*

Bachelor of Science in Physics & Astronomy **2012**
Bucknell University *Lewisburg, PA*

RESEARCH EXPERIENCE

Graduate Research Assistant **2013–2017**
University of California, Irvine *Irvine, California*

Undergraduate Student Researcher **2011**
Columbia University *New York, New York*

Undergraduate Student Researcher **2010**
Bucknell University *Lewisburg, PA*

TEACHING EXPERIENCE

Teaching Assistant **2012–2013**
University of California, Irvine *Irvine, CA*

REFEREED JOURNAL PUBLICATIONS

Modeling Smooth Backgrounds and Generic Localized Signals with Gaussian Processes — **Sep 2017**
arxiv

Jet Energy Scale Measurements and Their Systematic Uncertainties in Proton-Proton Collisions at s = 13 TeV with the ATLAS Detector — **Mar 2017**
Phys. Rev. D

Search for New Phenomena in Dijet Events using 37 fb-1 of pp Collision Data Collected at s = 13 TeV with the ATLAS Detector — **Mar 2017**
Phys. Rev. D

Properties of Jets and Inputs to Jet Reconstruction and Calibration with the ATLAS Detector Using Proton-Proton Collisions at s = 13 TeV — **Aug 2015**
Phys. Lett. B

Search for New Phenomena in Dijet Angular Distributions in Proton-Proton Collisions at s = 8 TeV Measured with the ATLAS Detector — **June 2015**
Phys. Rev. Lett.

Search for invisible decays of the decays of the Higgs boson produced in association with a hadronically decaying vector boson in pp collisions at s = 8 TeV with the ATLAS detector — **April 2015**
Eur. Phys. J. C

Collider Bounds on Indirect Dark Matter Searches: The WW Final State — **Mar 2014**
Phys. Rev. D

Systematically Searching for New Resonances at the Energy Frontier using Topological Models — **Jan 2014**
Phys. Rev. D

REFEREED CONFERENCE PUBLICATIONS

Search for New Phenomena in Dijet Events with the ATLAS Detector at s = 13 TeV with 2015 and 2016 Data — **Aug 2016**
ICHEP

Search for New Phenomena in Dijet Mass and Angular Distributions from pp Collisions at s = 13 TeV with the ATLAS Detector **Aug 2015**
LHCP

SOFTWARE

Gaussian Process Regression Tutorial `https://github.com/mfrate28/GP_Tutorial/`
Python tutorial on how to impliment a Gaussian Process Regression in LHC analyses.

GP Software Comparison `https://github.com/mfrate28/ComparingGPPackages/`
A comparison of Gaussian Process software.

GP MC Template Smoother `https://github.com/mfrate28/mc-template-smoother/`
Python tutorial on how to use Gaussian Process Regression to estimate the truth distribution from Monte Carlo Simulation.

ABSTRACT OF THE DISSERTATION

The Search for New Resonant Phenomena using Dijet Events at the ATLAS Detector

By

Meghan Frate

Doctor of Philosophy in Physics

University of California, Irvine, 2017

Professor Daniel Whiteson, Chair

A search for new physics resonances in the dijet invariant mass spectrum is presented here. Dijet events are collected at center of mass energy of 13 TeV with the ATLAS detector at the Large Hadron Collider in 2015 and 2016, equating to a total integrated luminosity of 37 fb^{-1}. This data is compared to background predictions, and no significant deviations from the expected is seen. Therefore, the dataset is used to set improved upper limits on the mass of four benchmark signal models and one generic model at 95% CL. These limits exclude excited quarks with masses below 6.0 TeV, quantum black holes below 8.9 TeV, heavy W' boson masses below 3.6 TeV, and W^* bosons masses below 3.4 TeV and between 3.77-3.85 TeV; as well as limits on a range of masses and couplings in a Z' dark matter mediator model. Model-independent limits are also set on signals with a Gaussian shape at various mass resolutions. Finally, a proof of concept study is done on a new method to predict dijet backgrounds, which may be implemented in future analyses.

Chapter 1

Standard Model

1.1 Standard Model

The Standard Model of Particle Physics (SM) is currently the most complete theory of particle physics, describing all known fundamental particles and their interactions. Developed throughout the 1960's and 1970's, the Standard Model proved its merit as the predicted particles were discovered at various experiments, with the most recent being the confirmation of a Higgs Boson in 2012 by both ATLAS and CMS collaborations [1][2]. The Standard Model consists of 12 spin 1/2 particles called fermions, and 5 integer spin (1 or 0) particles called bosons. These groups can be broken down further, with fermions consisting of 6 integer charge leptons and 6 fractional charge quarks, and bosons being a combination of four spin 1 vector bosons and one spin 0 scalar boson. Both leptons and quarks come in 3 generations or families, with two particles paired off in each family. Leptons are paired such that each charged particle has a corresponding neutral particle called a neutrino, i.e. the electron and electron neutrino. Quarks are paired such that there is one 1/3 charge particle and one 2/3 charge particle in each family, i.e. up and down quark. These family pairs have the same

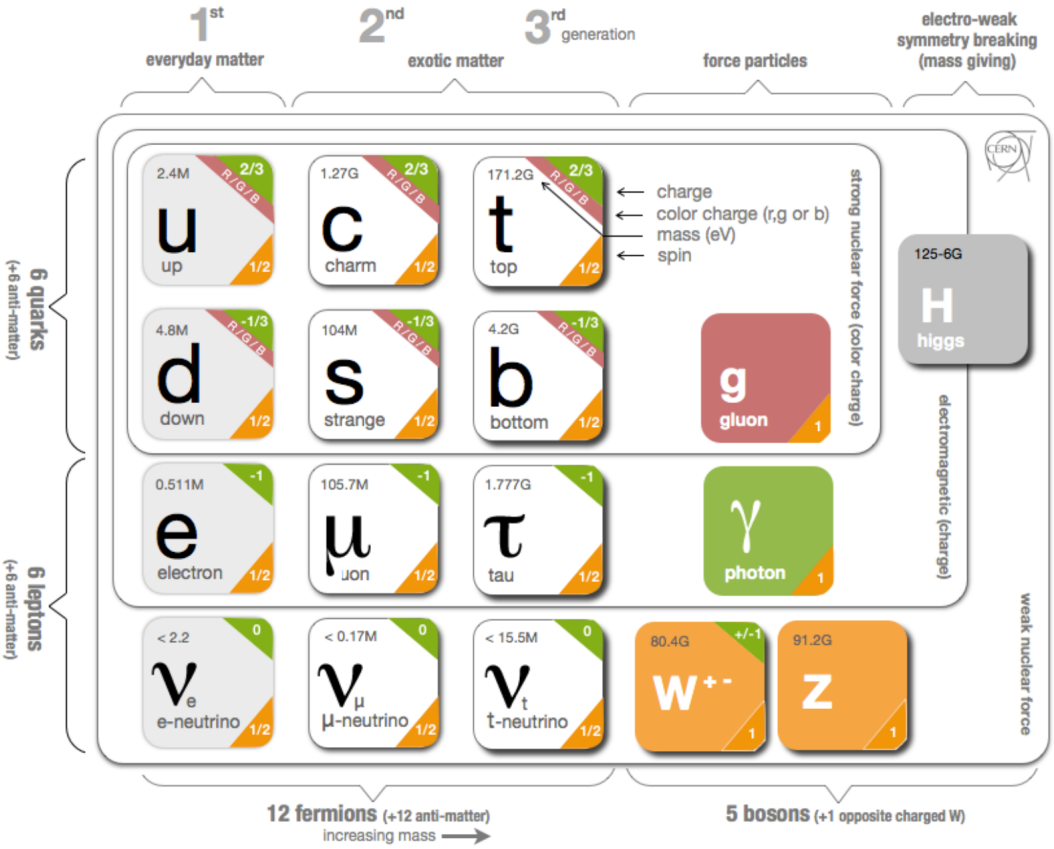

Figure 1.1: The layout of the Standard Model. On the left are fermions, split into their respective groups of leptons and quarks, both of which have three families. On the right, the gauge bosons, as well as the Higgs boson. Within each box the particle's mass, spin, and charge are listed [3].

quantum numbers, and only vary in mass. A graphical representation of the Standard Model is given in Figure 1.1.

The mathematical formulation of the Standard Model is based on three gauge symmetries, each of which corresponds to a physical force and the particles that interact via that force. These symmetries represent some type of gauge invariance, and results in a conserved quantity. For instance, assume a naive Lagrangian for electromagnetism $L = (\partial_\mu \phi(x))^\dagger (\partial^\mu \phi(x)) - V\phi(x)^\dagger \phi(x)$ with $\phi(x)$ the waveform for a lepton and V the potential.

This Lagrangian should be invariant under the global symmetry transformation $\phi(x) \rightarrow e^{i\alpha}\phi(x)$, which will only be true if $\partial_\mu j^\mu = \partial_\mu(i(\partial^\mu\phi^\dagger\phi - \phi^\dagger\partial^\mu\phi)) = 0$. The quantity j^μ is a therefore a conserved quantity, which is associated to charge conservation. If it is then assumed the Lagrangian is invariant under a local transformation $\phi(x) \rightarrow e^{i\alpha(x)Q}\phi(x)$, it can be shown that there is a need to replace ∂_μ with the covariant derivative $D_\mu = \partial_\mu - ieA_\mu$, where A_μ is defined as the photon field. It can be shown similarly with the weak and strong forces that global symmetries indicate a conserved quantity, while local symmetries provide the need for a gauge field. The symmetries in the Standard Model are represented by some set of unitary matrices ($U(N)$) or special unitary matrices ($SU(N)$), where N is the dimensions of the matrices. The three symmetries are U(1) describing the electromagnetic force, SU(2) describing the weak force, and SU(3) describing the strong force. Each of the $SU(N)$ symmetries has $N^2 - 1$ generators while the $U(N)$ has N^2 generators, or gauge bosons, that arise from the gauge fields discussed previously. For the electromagnetic force, there is only the photon. In the weak force, there are the W^+, W^-, and Z bosons. Finally, the strong force has 8 massless gluons. The strong force will be discussed in more depth in Section 1.3. The finally component of the Standard Model is the Higgs boson, a spin 0 massive particle which allows the other particles to have mass. Therefore, any massive particle interacts with the Higgs field, while those that are massless do not.

1.1.1 Higgs

Before the introduction of the Higgs mechanism, it was not possible to have mass terms in the Lagrangian for vector bosons or fermions. In both cases, a mass term would violate gauge invariance. For vector bosons, the field transforms in a particular manner to allow local symmetry, however this transform does not remain invariant with the addition of a mass term. For fermions it is due to the fact that they are doublets of two helicity states, left-handed and right-handed, which transform differently under gauge transformation. The

Higgs mechanism can supply mass to both by assuming there is an additional scalar particle that has a non-zero expectation value and is charged under $U(1)$, which breaks local gauge symmetry.

The Standard Model assumes a complex Higgs doublet $\phi = (\phi^+, \phi^0) = (\phi_1 + i\phi_2, \phi_3 + i\phi_4)$, with only the ϕ_3 component traditionally being referred to as the Higgs Boson. The Higgs Boson is able to provide mass to the vector bosons by breaking the combined $SU(2) \times U(1)$ electroweak symmetry (Section 1.1.2) into $U(1)_{EM}$, or the detectable weak and electromagnetic forces. This comes from the unique nature of the Higgs field, in that it has a vacuum expectation value (vev), which is non-zero. The fact that the Higgs is charged under electroweak theory yet it's field is has some non-zero energy implies that the electroweak theory is not consistent globally, meaning the symmetry is broken. Usually this is said as "the Higgs acquired a vev", meaning at the energy scale where electroweak theory is unified, all components of the Higgs doublet are equally combined, however the Standard Model Higgs can acquire energy and choose a state, therefore breaking symmetry.

1.1.2 Electroweak symmetry breaking

To delve a bit deeper into the symmetry breaking mentioned above, known as Electroweak Symmetry Breaking, it's important to step back to the electromagnetic and weak forces. As mentioned before, the weak and electromagnetic force are unified at higher energies into the electroweak force, which is the true $SU(2) \times U(1)$ symmetry. The gauge boson for $U(1)$ is the B boson, and the gauge bosons for $SU(2)$ are the W_1, W_2, W_3 bosons. The W+ and W- bosons are actually linear combinations of the W_1 and W_2 bosons ($W^\pm = \frac{1}{\sqrt{2}}(W_1 \pm W_2)$), while the photon and Z bosons are combinations of W_3 and B, $B\cos\theta_W + W_3 \sin\theta_W$ and $-B\sin\theta_W + W_3\cos\theta_W$ respectively. As all bosons of the electroweak theory are massless, all of these linear combinations are still lacking mass, which is where the Higgs becomes an

integral part of the theory. An important effect of symmetry breaking is described by the Goldstone theorem [4][5][6], which states that there must be an equivalent number of massless spin-0 particles as there are broken generators. These massless Goldstone bosons are the remaining three components of the Higgs boson (ϕ_1, ϕ_2, and ϕ_4) mentioned in Section 1.1.1. These Goldstone bosons are "eaten" by the combined Ws and B bosons to produce the massive $W^{\pm}$ and Z bosons. More technically, the W and Z bosons have two transverse polarization states, and each of the Goldstone bosons have one scalar degree of freedom. To have a mass, a third longitudinal polarization state must be added to the gauge bosons, which comes from combining with the Goldstone boson. The photon does not "eat" a Goldstone boson, and therefore remains massless.

1.1.3 Problems with the Standard Model

However accurate and elegant the Standard Model is, there are still plenty of unexplained phenomena. This is the foundation for the Exotic Searches at the LHC, including this analysis, as there appears to be more to fundamental physics than the SM predicts.

Gravity

One of the most glaring omissions from the Standard Model is the fourth known fundamental force, gravity. It is predicted that there exists a spin-2 Graviton however there has been no evidence. A leading theory to account for its lack of detection is that gravity extends to extra dimensions. There can be multiple flat dimensions, as in the ADD model [7][8], or a single extra warped dimension, as in the Randall Sundrum (RS) model [9]. The current scale of gravitational forces exists at the Planck scale M_{pl}, but the addition of extra dimensions may dilute the scale of gravity to within the TeV range, which is within the energy scope of the LHC.

Hierarchy Problem

The extreme difference between the Higgs mass (125 GeV) and and the Planck mass (10^{19} GeV) is another troubling piece of the Standard Model. With such an enormous difference in energy, the mass of the Higgs Boson should be much higher than its measured value. The only way to have a mass as low as measured is for cancellations of higher order loop corrections to the Higgs mass. While it is possible this happens naturally, its extremely improbable that the universe exhibits such fine tuning. A solution to this problem is to introduce new physics at TeV energy scales. Theories of gravity involving extra dimensions as mentioned in Section 1.1.3 lower the energy scales of gravity to allow for a more cohesive scale across all forces. Another solution is supersymmetry (SUSY), where the introduction of supersymmetric partners with masses in the GeV-TeV scale will cancel loop diagrams of SM particles, resulting in the Higgs mass that is measured.

Dark Matter

The Standard Model also fails to include dark matter (DM). Though hints of dark matter had been around for decades [10], confirmation of its existence took off in the 1930's with a series of astronomers noticing discrepancies in the mass to light ratio of galaxies [10]. There is not much known about dark matter, besides it interacts gravitationally but not electromagnetically, as well as its relative amount in the universe. Although its not known whether dark matter interacts with the weak force or strong force, a leading theory is that dark matter is a weakly interacting massive particle, or WIMP [10]. Large support for this theory comes from the WIMP miracle, which notes a particle of similar mass and cross section to that of the weak gauge bosons would produce the proper relic density of dark matter. With WIMPS being in the 100 GeV - TeV mass range, they are within reach of the LHC.

Standard Model Extensions

The overall structure of the SM is also rather arbitrary. That there are three families of leptons with seemingly random differences in mass hints that there may be some more underlying structure to make sense of such differences and structure. There may be extensions to the SM as well, such as additional symmetries or heavier particles that would have been out of reach of previous lower energy detectors. Of particular interest that comes in the form of additional symmetries is creating a grand unified theory (GUT). Similar to the combination of the weak and electromagnetic forces into the electroweak force (Section 1.1.2), it is theorized that all fundamental forces, including gravity, may be pieces of a overarching symmetry at high energies. The leading theories for the unification of the strong force with the electroweak force are a unified $SU(5)$ or $SO(10)$, each of which could manifest themselves at the LHC in the form of new gauge bosons.

1.2 New Physics

As can be seen, there is a need for new particles or interactions, or in general "new physics", to exist, and there are many models that can be probed at the LHC. The theories presented here will be those that are specifically searched for by the dijet resonance analysis.

1.2.1 Quantum Black Holes

Gravity can be probed at the ATLAS detector in several ways, and one of these is searching for Quantum Black Holes. As mentioned in Section 1.1.3, if gravity does exist in extra dimensions, this would lower the scale of gravity to some modified gravity scale M_D that is closer to that of the other fundamental forces. The hoop conjecture [11] suggests that if

the impact parameter of two incoming partons is less than that of a Schwarzschild radius r for the combined mass of the two partons, that these two partons can create a Quantum Black Hole (QBH). If this threshold mass is approximately at the order of the modified gravity scale M_D, the QBH will decay into SM particles following quantum conservation laws, rather than classical conservation laws followed by classical black holes [12][13][14]. The QBH will mostly decays to dijets when $M_D \sim M_{th}$, meaning it can be probed with the dijet analysis.

1.2.2 Dark Matter Mediator

A new model that could link SM particles and DM particles is the addition of another U(1) symmetry in the Standard Model. This addition would predict a new particle Z' that can mediate between SM and DM particles [15][16][17]. If this is the case, the two colliding partons may create this Z', which can then decay back into quarks or into two dark matter particles. In the case of a decay to quarks, the dijet analysis can search for the Z' resonance. This model has become the new standard for DM searches at ATLAS, as results can be combined across many searches including multiple dijet analyses, missing energy plus initial state radiation, and dilepton searches [18].

1.2.3 Compositeness

Another new physics model searched for in the dijet analysis is quark compositeness. This seeks to test for more fundamental particles, by assuming that quarks are composite particles, and therefore an excitation of the quarks may become visible at higher energies. This new quark could decay through $q^* \rightarrow qg$, creating a resonance at the q^* mass [19][20].

1.2.4 Heavy Gauge Bosons

In the several theories of GUT mentioned in Section 1.1.3, a decomposition of these higher order symmetries introduces a new SU(2), and with that comes the addition new gauge bosons. The existence of a number of heavy bosons can be probed in the dijet analysis, however as a benchmark model this analysis searches for a Sequential Standard Model (SSM) W', which has the same couplings as the SM W boson but varies in mass [21][22]. The decay to quarks can be searched for in the dijet analysis, while its decay to leptons, or its decay to WZ, are searched for with complimentary exotic analyses.

1.2.5 Excited Chiral Bosons

A specific modification to the SM can be the existence of some $SU(3)_W \times U(1)_W$ extension of the electroweak group, that can spontaneously break down to the Standard Model electroweak symmetries. A weak doublet is then associated with the doublet component of the $SU(3)_W$ group, resulting in new excited weak bosons $\pm W^*$ and Z^* [23][24]. This group of theories is often used to solve the hierarchy problem by predicting the lightness of the Standard Model Higgs, and would also provide evidence that the W boson is a composite particle. W^* can be generated at different mixing angles, $\sin\theta_X$, which predicts either leptophobic or leptophilic final W^*, where the dijet analysis uses the leptophobic ($\sin(\theta_X) = 0$) signal model.

1.3 Quantum Chromodynamics

This section is adapted from information in Ref [25]. Quantum Chromodynamics (QCD) is the theory of the strong force. The only fundamental particles to feel the strong force are

quarks, and the gauge bosons of the strong force are gluons. Quarks have charges in fractions of 1/3 (as can be seen in Figure 1.1) and come in 3 different *flavors*, red, green, and blue. These colors have nothing to do with optics, but are rather an equivalent *charge* for the strong force. Quarks form either pairs or triplets of colorless and integer charge composite particles called hadrons. For example, a red up quark and anti-red anti-up quark, or a red up quark, blue up quark, and green down quark. The combinations of two quarks are called mesons, while combinations of 3 are called baryons. The cross section calculation in QCD is similar to other Standard Model processes, but due to color charge now includes summation (outgoing) or a mean (incoming) over color charge.

There are 8 gluons, representative of the 8 color combinations of quarks that a gluon can propagate between. Similarly it is related to the dimensions of the SU(3) symmetry by $N_C^2 - 1 = 8$. Due to the non-abelian nature of QCD, extra terms pertaining to the mediator particle are added to the Lagrangian. This results in the production of 3 and 4 gluon interactions, which no other mediator particle has. The full Lagrangian is given in Eq. 1.1

$$\mathcal{L}_{QCD} = \bar{\psi}_f^i (i\gamma^\mu)(D_\mu)_{ij}\psi_f^j - m_f \bar{\psi}_f^i \delta_{ij} \psi_f^j - \frac{1}{4} F_{\mu\nu}^a F^{a\mu\nu} \tag{1.1}$$

where $F_{\mu\nu}^A$ is a tensor given by

$$F_{\mu\nu}^a = \partial_\mu A_\nu^a - \partial_\nu A_\mu^a - g_s f_{abc} A_\mu^b A_\nu^b \tag{1.2}$$

and D_μ is the covariant derivative given by

$$(D_\mu)_{ij} = \delta_{ij}\partial_\mu - i g_s t_{ij}^a A_\mu^a \tag{1.3}$$

The quark spinors are represented by ψ with some flavor index $f = 1, 2, 3$, and the gluon fields by A_μ^α, where α runs from 1 to $N_C^2 - 1 = 8$. This Lagrangian can be broken down into five parts:

- quark mass $\bar{\psi}_f^i m_f \delta_{ij} \psi_f^j$, where δ_{ij} is a Dirac delta function
- quark propogator $\bar{\psi}_f^i i\gamma^\mu \delta_{ij} \partial_\mu \psi_f^j$

- quark-gluon interactions $\bar{\psi}^i_f g_s t^c_{ij} A^c_\mu \psi^j_f$, where t^c_{ij} are the SU(3) generators, one of eight 3x3 matrices related to the Gell-Mann matrics by $t^\alpha_{ij} = \frac{1}{2}\lambda^\alpha_{ij}$.

- 3 and 4 point gluon interactions from $\frac{1}{4}F^a_{\mu\nu}F^{a\mu\nu}$, where f_{abc} is related to the field generators by $[t^a, t^b] = if_{abc}t^c$

1.3.1 Renormalization

QCD cross sections contain divergences, which are unphysical. To mend this, many QCD quantities are renormalized; split into perturbative and non-perturbative pieces and separated by an energy scale μ. The coupling constant g_s in Eq. 1.1 is one such quantity, and is related to the strong coupling α_s by $g_s^2 = 4\pi\alpha_s$. Renormalizing the strong coupling creates a running coupling, where the coupling is dependent on the logarithm of the energy scale of the interaction Q^2 by $\frac{d\alpha_s}{dlnQ^2} = \beta(\alpha_s)$. That is, the coupling dependence on the energy scale follows a renormalization group equation (RGE) given by Eq. 1.4

$$\beta(\alpha_s) = -(b_0\alpha_s^2 + b_1\alpha_s^3 + b_2\alpha_s^4 + ...)\,, \tag{1.4}$$

where the LO and NLO coefficients are given by

$$\begin{aligned} b_0 &= (11C_A - 4n_f T_R)/(12\pi) \\ b_1 &= (17C_A - 4n_f T_R(10C_A + 6C_F))/(24\pi^2) \end{aligned} \tag{1.5}$$

In these equations, n_f is the number of quark flavors present at that energy scale, and C_F, C_A, T_R are color constants associated with specific QCD processes. It is clear from the negative in Eq. 1.4 that as momentum transfer Q^2 increases, the coupling becomes weaker. Plotting α_s as a function of the scale Q^2 Fig. 1.2 shows that at high scales, the coupling remains approximately constant and small, something called asymptotic freedom. This means at high energy, or small distances, the coupling becomes so small that quarks and gluons decouple, and can be treated as independent particles. This is an important effect in fragmentation theory, which will be discussed later in this section. Taking the coupling to

low energies, it can be seen that the coupling quickly diverges. A cutoff scale, denoted Λ_{QCD} is therefore required to combat this divergence, removing all non-perturbative calculations which exist below Λ_{QCD} from the perturbative calculations above it, and is calculated to be 200 MeV . This low energy or conversely long distance scale divergence results in a phenomena called confinement, in which any quark beyond a distance $1/\Lambda_{QCD}$ will never be found alone, but always in a colorless pair. This will be discussed in more depth in Section 1.3.2. By solving equation 1.4 directly, it can be shown that the strong coupling can be computed at any energy scale in conjunction with a specific energy scale, usually $Q^2 = M_Z^2$, where M_Z is the mass of the Z boson. This reduces the strong coupling to a more manageable formula given by Eq 1.6.

$$\alpha_s(Q^2) = \alpha_s(M_Z^2)\frac{1}{1 + b_0\alpha_s(M_Z^2)ln\frac{Q^2}{M_Z^2} + \mathcal{O}(\alpha_s^2)} \tag{1.6}$$

1.3.2 Confinement

Similar to a rubber band, as the separation of two quarks increases, the strong coupling increases, until it reaches a point where it requires less energy to pair produce quarks that will pair with the original quarks than it does to keep the two quarks together. This pair production energy comes from energy converted from the strong force holding the two quarks together. The combination of quarks in pairs or triplets to form hadrons and mesons is due to confinement, and confinement also has a large part to play in the creation of jets.

This running coupling has many implications for LHC physics, such as high p_T jets producing less radiation and therefore a more narrow jet than low p_T, and that cross sections for high p_T jets can be calculated directly with perturbative QCD, but low energy collisions such as underlying events (UE) and pileup must rely on non-perturbative calculations.

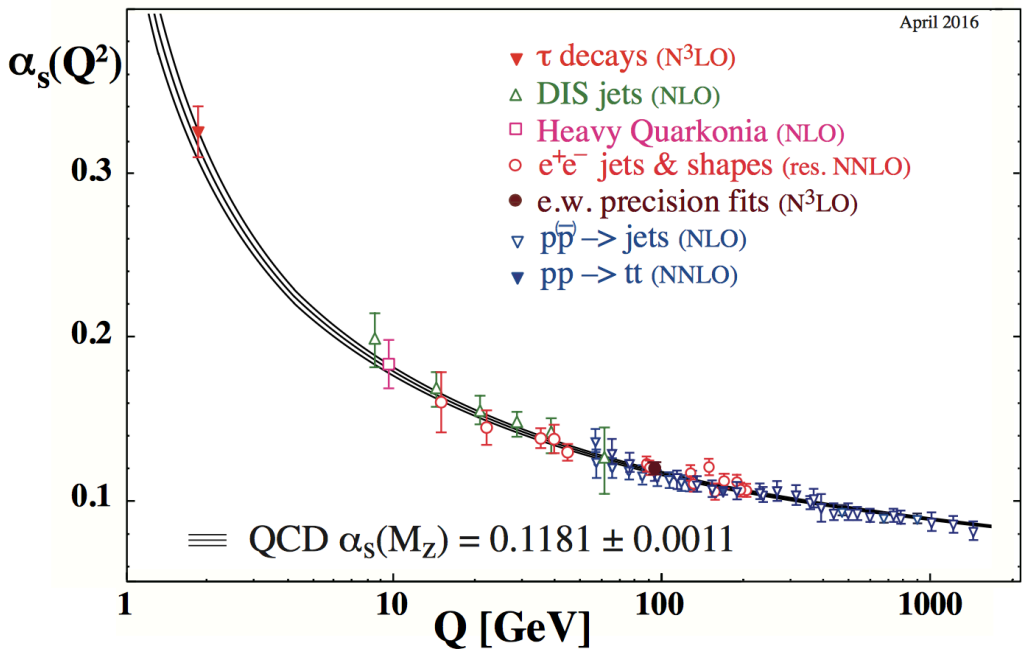

Figure 1.2: Measurements of strong coupling α_S as a function of energy scale Q, with a smooth fit overlaid [26].

1.3.3 Parton Distribution Functions

A second renormalization scheme appears in fragmentation theory [27], which states that non-perturbative hadron cross sections can be fragmented into two independent pieces, non-perturbative and perturbative. The hadron-hadron cross section can then be broken down as follows

$$d\sigma_{h1,h2} = \sum_{ij} \int_0^1 dx_i \int_0^1 dx_j \sum_f d\Phi_f f_{i/h_1}(x_i, \mu_F^2) f_{j/h_2}(x_j, \mu_F^2) \frac{d\sigma_{ij\to f}}{dx_i dx_j d\Phi_f} \tag{1.7}$$

where f is the Parton Distribution Function (PDF), a non-perturbative estimate of the distribution of partons within the proton, and $\frac{d\sigma_{ij\to f}}{dx_i dx_j d\Phi_f}$ is the partonic cross section, which is independent of the hadron and perturbative. This is summed over all possible parton combinations in each hadron, integrated over all possible occurrences of the two partons i, j to some final state f, and integrated over the possible incoming energy of each parton x_i and x_j. All divergences are then grouped into the PDF, which then depends on a user defined factorization scale μ_f. This factorization scale should be at the energy scale in which perturbative calculations are no longer viable. Cross sections can be broken up in this way due to confinement - free quarks will ever exist on their own on timescales less than $1/\Lambda_{QCD}$, however the time duration of a collision is of the order $1/Q << 1/\Lambda_{QCD}$. This means that for colliding hadrons, their makeup is frozen in the eyes of the incoming particle. This allows the cross sections of parton-parton collisions to simply be weighted by the probability that that parton existed at the time of collision in the hadron, which is the PDF.

PDFs are estimated from data measurements. There are currently three different groups combining experimental results to produce a set of PDFs at various orders; MSTW2008[28], CT10 [29], and NNPDF2.3 [30]. All of these collaborations have different forms of the PDF and different tunes, or treatment and values of parameters impacting the PDF, such as the factorization scale. All use the renormalization group equation DGLAP (Eq. 1.8)[31], which provides a series of equations that allows the evolution of a PDF from one scale to another. This means that a PDF does not have to be derived at every user set scale, but can be

inferred. The DGLAP equation depends on splitting functions, listed below in Eq 1.9, which perturbatively define the probability P_{ab} of any parton collinearly radiating another parton, resulting in two partons a and b with fraction z and $(1-z)$ of the initial parton energy.

$$\begin{aligned}
\mu^2\frac{\partial}{\partial\mu^2}f_i(z,\mu^2) &= \sum_j\int_x^1\frac{dz}{z}\frac{\alpha_s}{2\pi}P_{ij}(z)f_j(x/z,\mu^2)\\
\frac{\partial q_i(x,\mu^2)}{\partial log\mu^2} &= \frac{\alpha_s}{2\pi}\int_x^1\frac{dz}{z}[P_{q_iq_j}(z,\alpha_s)q_j(\frac{x}{z},\mu^2)+P_{q_ig}(z,\alpha_s)g(\frac{x}{z},\mu^2)]\\
\frac{\partial q_i(x,\mu^2)}{\partial log\mu^2} &= \frac{\alpha_s}{2\pi}\int_x^1\frac{dz}{z}[P_{gq_i}(z,\alpha_s)q_j(\frac{x}{z},\mu^2)+P_{gg}(z,\alpha_s)g(\frac{x}{z},\mu^2)]
\end{aligned} \tag{1.8}$$

$$\begin{aligned}
P_{qq}(z) &= C_F\left[\frac{1+z^2}{(1-x)_+}\right]+2\delta(1-x)\\
P_{qg}(z) &= T_R[z^2+(1-z)^2]\\
P_{gq}(z) &= C_F\left[\frac{1+(1-z)^2}{z}\right]\\
P_{gg}(z) &= 2C_A\left[\frac{z}{(1-z)_+}+\frac{1-z}{z}+z(1-z)\right]+\delta(1-z)\left[\frac{(11C_A-4n_fT_R)}{6}\right]
\end{aligned} \tag{1.9}$$

For dijet events, the possible final states are all $2\rightarrow 2$ scattering amplitudes from partons to quarks or gluons. The cross section for dijet production from parton-parton collisions is given by Eq. 1.12. At leading order, these matrix elements can be computed through Feynman rules.

1.3.4 Feynman diagrams

All cross sections of SM processes are computed through an S-matrix, in which each element gives the probability amplitude of a specific SM process occurring. If there are multiple processes that give the same initial to final state, those amplitudes must be summed to give the correct contributions to the cross section. Feynman diagrams are a pictorial tool and a set of rules which aids in leading order calculations of cross sections. Each matrix

element given from a Feynman diagram has a quantity related to the incoming particles, the propagator, the interaction points, and the outgoing particles. The final cross section is then summed over all possible incoming and outgoing particles, i.e. over all possible quark colors. A simple example that is relevant for this analysis is quark t-channel scattering. The Feynman diagram representing this process is shown in Figure 1.3, with looped lines indicating gluons, and straight lines representing quarks. The matrix elements are created from the following set of rules:

- incoming quark $u_{q_f}(p)$ where p is the quark momentum and q_f is the flavor
- incoming anti-quark $v_{q_f}(p)$ where p is the quark momentum and q_f is the flavor
- incoming gluon e^{μ}
- quark propogator $\delta^{ik}\frac{i(\not{p}+m)}{\not{p}-m^2-i\epsilon}$
- gluon propogator $\delta^{ab}\frac{-ig^{\mu\nu}}{q^2}$ where q is the momentum, and a, b are color indices
- quark-quark-gluon vertex $-\frac{1}{2}ig_s\lambda^a_{ji}\gamma^{\mu}$ where i, j is the color indices or the quarks
- outgoing gluon $e^{\mu *}$
- outgoing quark $\bar{u}_{q_f}(p)$ where p is the quark momentum and q_f is the flavor
- outgoing anti-quark $\bar{v}_{q_f}(p)$ where p is the quark momentum and q_f is the flavor

The matrix element M can be calculated from the above rules as Eq. 1.10.

$$-iM = [\bar{u}_{q_1}(p_3)(-\frac{1}{2}ig_s\lambda^a_{ji}\gamma^{\mu})u_{q_2}(p_1)]\frac{-ig_{\mu\nu}}{q^2}\delta^{ab}[\bar{u}_d(p_4)(-\frac{1}{2}ig_s\lambda^b_{lk}\gamma^{\nu})u_{q_3}(p_2)] \tag{1.10}$$

where the Kronecker delta function (δ^{ab}) enforces the allowable color states (color-anticolor pairs), which then reduces to Eq. 1.11. The next step is to average over all possible color combinations of the quarks by $|M|^2 = \frac{1}{N_C}\frac{1}{N_C}\sum_{i,j,k,l=1}^{3}|M(ij \rightarrow kl)|^2$, where i, j, k, l are

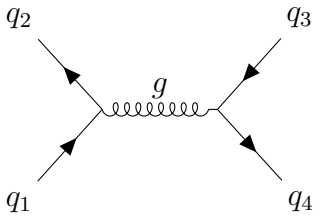

Figure 1.3: Feynman diagram of a qq scattering event [32].

allowable color combinations. Finally, for each incoming ($\bar{u}_{q_1}$ and u_{q_2}) and outgoing combination of quark ($\bar{u}_{q_3}$ and u_{q_4}) *flavors*, there is similarly an additional matrix element, all of which will be summed together. At first order this is how cross sections are computed.

$$M = -\frac{g_s^2}{4}\lambda^a_{ji}\lambda^a_{lk}g_{\mu\nu}[\bar{u}_{q_1}(p_3)\gamma^\mu u_{q_2}(p_1)][\bar{u}_d(p_4)\gamma^\nu u_{q_3}(p_2)] \tag{1.11}$$

1.3.5 NLO corrections

At next to leading order, loop diagram and initial and final state radiation (ISR/FSR) must be taken into account, with several examples shown in Figure 1.4. The addition of higher order terms results in a diverging cross section in two ways. The first is ultraviolet (UV) divergences which are a result of virtual loop diagrams. The second is infrared (IR) divergences, which includes collinear and soft radiation. Regularization is a way to group these divergent terms and remove the section of phase space most effected, and does so by the introduction of a user defined scale. UV divergences are regularized with the regularization scale μ_R included in the running coupling. This cuts off the summation of infinitely low energy loops. IR divergences are regularized in PDFs through the factorization scale μ_F, resulting in the absorption of any soft radiation into the PDF. For the dijet analysis, per

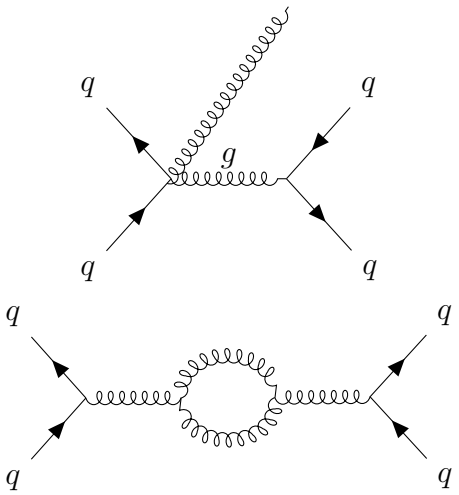

Figure 1.4: Feynman diagrams of next-to-leading order qq scattering events, with the top diagram being an example of initial state radiation and the bottom an example of a loop correction [32].

ATLAS recommendation, the renormalization and factorization scales are set to the average of the two leading jet p_T, $\mu_R = \mu_F = (p_{T1} + p_{T2})/2$.

$$\frac{d^3\sigma}{dy_3 dy_4 dp_T^2} = \frac{1}{16\pi s^2} \sum_{a,b,c,d=q,\bar{q},g} \frac{f_{a/A}(x_a,\mu^2)}{x_a} \frac{f_{b/B}(x_b,\mu^2)}{x_b} \times \sum |M(ab \to cd)|^2 \frac{1}{1+\delta_{cd}} \quad (1.12)$$

Two IR divergences have large consequences in LHC physics - collinear and infrared. Collinear divergence comes from collinear ISR or FSR, where a gluon is emitted parallel to its parent particle. The distinction between a single particle of the sum of energy of the gluon and parent particle and the split version is meaningless, and causes a divergence in the cross section. Infrared divergences result from soft radiation, as cross section calculations are ill defined for energies approaching zero. In cross section calculations, the KLN [33] theory states that as long as cross sections are inclusive, as in they include all radiation and loops, these divergences should cancel each other. These divergences may still play a part if other observables used in the analysis are sensitive to IR or collinear radiation however.

It is therefore important to use IR and collinear safe variables, which are unchanged by the inclusion or removal of these forms of radiation. This will play an important role in the choice of jet algorithms in Section 3.1.1.

1.4 Collision events

The final cross section between the two colliding hadrons is given in Eq 1.13, where $f_{j/J}(x_j)$ is once again the PDFs and the cross section is summed over all possible partons in the hadron (a, b). The resulting particles of the collision, or in the case of a dijet event, the two scattered partons, are what determine the defined "event". A majority of collisions result in t-channel scattering, where the two incoming quarks exchange a gluon with relatively small energy transfer, and continue is slightly modified trajectories. This fact will come into play in event selections in the dijet analysis.

$$\sigma_{AB\to X} = \sum_{a,b} \int dx_a dx_b f_{a/A}(x_a) f_{b/B}(x_b) x d\hat{\sigma}_{ab\to X}(\alpha_S(\mu_R^2), \mu^2) \tag{1.13}$$

In order to properly explain the collision events, its important to note some terminology:

Hard Scatter: The hard scatter event is taken as the highest energy collision between two partons in a bunch crossing. This is shown as a red disk in Figure 1.5

Underlying Event: Underlying events (UE) are lower energy parton collisions that occur within the proton. Being of low energy, these cross sections are included in the PDF portion of the total cross section. This is shown in purple in Figure 1.5

Pileup: Pileup can be hard or soft collisions either from other proton collisions in the bunch crossing, or from collisions with remnants left from previous bunch crossings. Pileup needs to be removed from the overall event, and is discussed in section 3.1.3.

1.4.1 Parton Shower

Once the partons collide, any resulting partons will accelerate into the detector, resulting in the radiation of gluons, which will then split into quarks and other gluons. The modeling of this is called a parton shower, and is described by the same splitting functions used in PDFs. The splitting functions are combined to give the probability of a parton splitting at a time t and no other splitting occurred up to that point, and is given in Eq. 1.14. Partons are split until their energies are low enough for confinement effects to take over. This is shown in red in Figure 1.5.

$$\frac{dP_a}{dt} = (\sum_{b,c} I_{a\to bc}(t))exp(-\int_{t_0}^{t} dt' \sum_{b,c} I_{a\to bc}(t')) \tag{1.14}$$

1.4.2 Hadronization

Now that the partons have reached a sufficiently low energy, they will pair up to create hadrons and mesons. Many of these are unstable, immediately decaying into a combination of other hadrons and leptons, and continuing to create a spray of particles as seen in Figure 1.5. Different Monte Carlo generators use different schemes, however the two most common are cluster [34] and string [34][35] models. These both step through pairing nearby quarks into final stable hadrons.

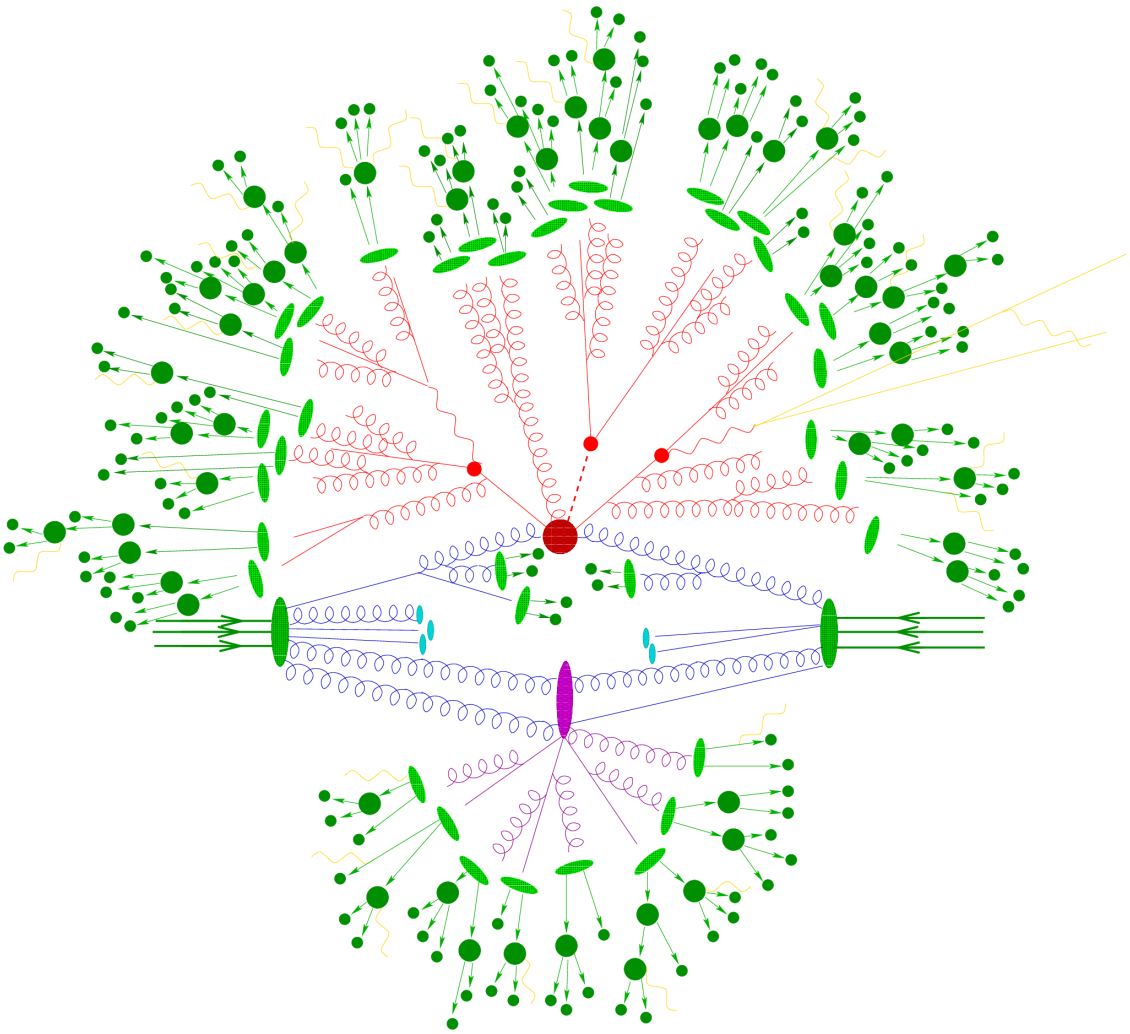

Figure 1.5: Schematic drawing of parton showering and hadronization. The hard scatter is the red disk. Purple disk is secondary hard scatter. Red and purple lines are the corresponding parton shower. Hadronization is in green, with parton groupings to hadrons in light green disks, dark green disks are hadron decays, and yellow is photon radiation [36].

Chapter 2

The ATLAS Detector

2.1 CERN and the LHC

2.1.1 CERN

The Center for European Nuclear Research (Conseil Europen pour la Recherche Nuclaire) or CERN is a nuclear and particle physics research lab in Meyrin, Switzerland that was founded in 1954. At its creation, the collaboration consisted of 12 European countries, and has since grown to 22 member nations, with countless other countries involved in research at CERN. Although there has been a variety of experiments run at CERN, it has always been a leading institute in particle accelerators. The first accelerator at CERN was the Sychrocylcetron, followed shortly by the Proton Synchrotron and then the Super Proton Synchrotron in the 1960's and 1970's. Next came the Large Electron-Positron Collider, or LEP, at the end of the 1980's, which was built in the same tunnel used by the Large Hadron Collider today.

2.1.2 The Large Hadron Collider

The Large Hadron Collider (LHC) is a 26 km round proton proton collider at CERN, and is thoroughly explained in Ref. [37]. Protons are first collected from Hydrogen atoms into bunches of approximately 1.15×10^{11} protons. These bunches of protons are accelerated through three separate synchrotrons built off the main ring to a small fraction of their final energy. The bunches are then injected into the beam pipe in 25ns bunch spaces and continually accelerated and compacted until reaching the desired 7 TeV energy. A series of magnets bend the protons around the ring, with extra layers of magnets used to correct protons at various distances in the bunch. The two beams of protons are crossed at four points along the ring to create collisions at the corresponding LHC experiments: ATLAS, CMS, ALICE, and LHCb (Figure 2.1).

The LHC was built for a maximum center of mass (COM) energy of 14 TeV, bunch spacing of 25ns, and an instantaneous luminosity of $10^{34} cm^{-2} s^{-1}$. At full running conditions, this equates to $1e^6$ collisions per second. Due to some difficulties at the start of the LHC in 2010, the LHC was started at half of the full spec running, having a COM energy of 7 TeV and 50ns bunch crossings, resulting in half the expected luminosity for Run I. The COM was increased to 8 TeV in the middle of Run I, but bunch spacing was kept at 50ns. Collectively, this resulted in $26 fb^{-1}$ integrated luminosity. Run I ended in 2012, where the detector was shut down for upgrades until summer of 2015. After this first Long Shut Down, the LHC started back up at 13 TeV COM energy and bunch spacing at 25ns. This analysis, the second dijet paper of Run II, is the full luminosity of Run II, equating to a total of 37 fb^{-1} integrated luminosity. During Run II, it is expected to increase to full COM energy of 14 TeV, and expected luminosity by the end of Run II in 2018 is $150 fb^{-1}$ [39], although current condition suggest its possible to reach $300 fb^{-1}$. The LHC will then go through its second long shut down of 2 years, and start up for Run III in 2020 for 3 years. Finally, after a two and a half year long shutdown with major improvements, the High Luminosity LHC

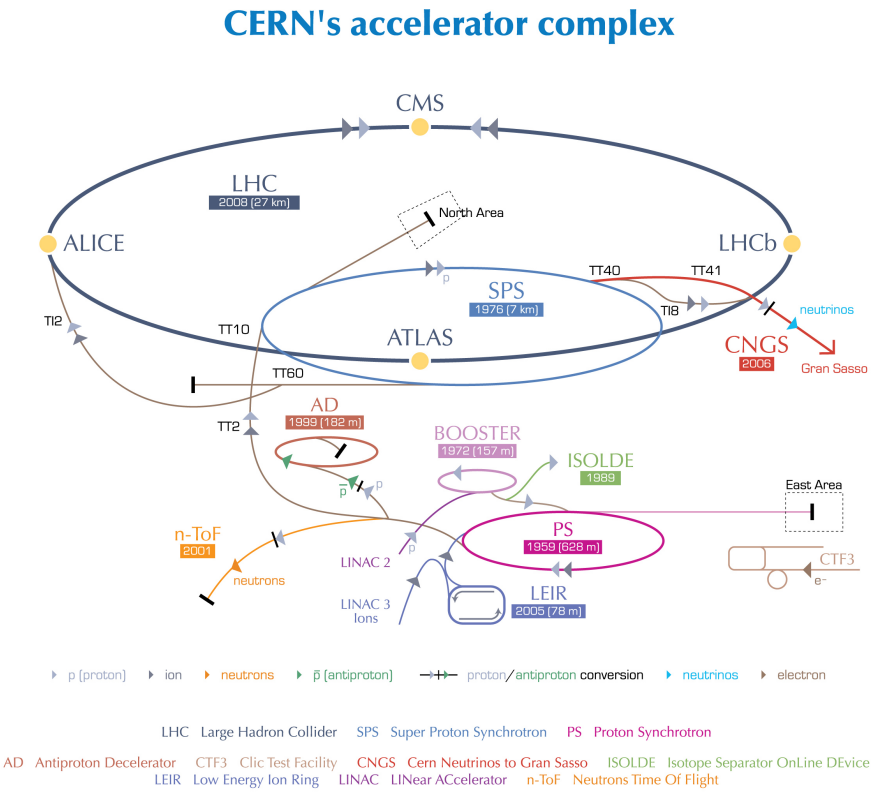

Figure 2.1: The LHC layout with all four detectors, ALICE, CMS, LHCb, and ATLAS, as well as acceleration rings [38].

will be operational, and run with a peak luminosity more than double then that of the first three runs. This will continue for the remainder of the LHC lifetime, until 2035.

2.1.3 Luminosity

The components of the beams and detector size are all factors in determining the final luminosity and center of mass energy allowed at the LHC, with luminosity and COM energy having the largest impact in the possible new particles accessible at the LHC. Beam quantities such as number of protons in each beam N, the rate of bunch crossings f, and cross sectional area A are related to the instantaneous luminosity L by $L = \frac{N^2 f}{A}$. This instantaneous luminosity is what determines the number of events of some interaction, with the rate of interactions given by $R = L\sigma$, with σ being the cross section of that event. The center of mass energy directly relates to energy available for new particle production. The LHC is therefore expected to probe new physics at the GeV-TeV energy scales, and one detector built to measure these new particles is the ATLAS detector.

2.2 ATLAS Detector

The ATLAS detector is one of two general purpose detectors along the LHC, with its design outlined in Ref. [40]. Its a 46 m long by 25 m diameter cylinder detector consisting of 6 subdetector systems located under Point 1 on the LHC ring. It consists of 4 magnets - a solenoid which is situated outside of the inner detector, used to bend particles through the inner detector to get an estimate of charge and momentum, and 3 toroidal magnets outside the calorimeters to accelerate particles through the muon system. A sketch of the layout of the detector can be found in Figure 2.2.

Running is broken up into *run blocks* and *luminosity blocks*. *Run blocks* contain the same

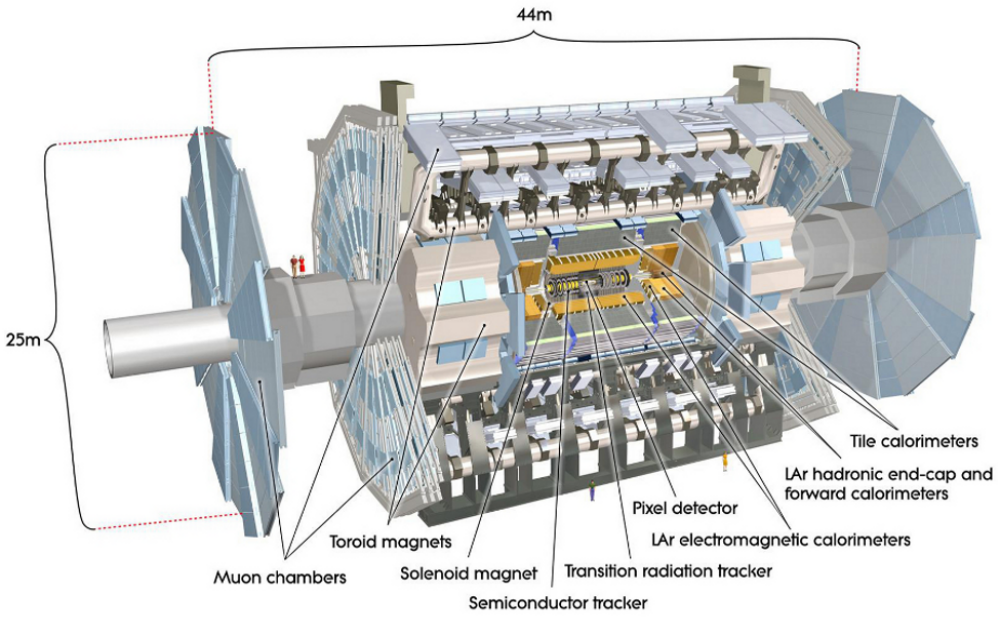

Figure 2.2: An overview of the ATLAS detector with the three inner detectors, Pixel detector, semiconductor tracker, and transition radiation tracker, as well as the central LAr electromagnetic calorimeters and tile calorimeters. It also displays the location of the calorimeter end caps or the LAr hadronic end-cap and forward calorimeter, as well as the muon spectrometer and the inner detector solenoid magnet and the muon spectrometer toroid magnet [40].

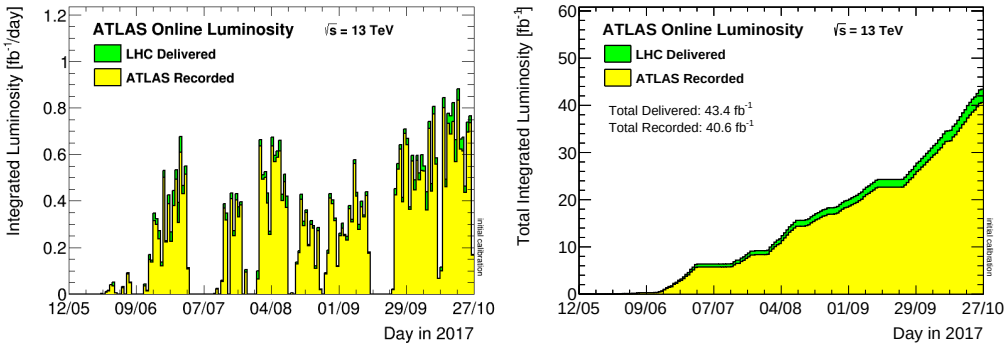

Figure 2.3: Integrated luminosity per day shown in (a) and running total of luminosity shown in (b) for 2017, where (b) is the cumulative sum of (a) [41].

proton bunches, continually colliding until the bunches have lost approximately 50% of their luminosity, typically 12-24 hours later. *Luminosity blocks* are the smallest interval of time within a *run block* where the instantaneous luminosity can be accurately calculated. This integrated luminosity per day is shown in Figure 2.3. All running conditions are assumed to be constant during this period. A good runs list (GRL) is a collaboration wide set of what are deemed "good runs" blocks, i.e. with all parts of the detector working correctly, and because of this only runs in the GRL are used for physics analysis. The total integrated luminosity is also recorded, with the total luminosity collected in 2017 shown in Figure 2.3.

In Cartesian coordinates, the ATLAS detector is laid out such that the z-axis is along the beam pipe, the x-axis points radially inward to the center of the ring from the detector, and the y-axis points directly upwards. A more obvious choice of coordinates for the detector is a cylindrical coordinate system, and is whats used in analyses. In this system, the z-axis remains the same, the azimuthal angle ϕ is in the x-y plane parallel to the end caps of the detector, with $\phi = 0$ pointing in the positive x direction, and the azimuthal angle θ is in the y-z plane with $\theta = 0$ in the positive z direction. A layout can be see in Figure 2.4. Often, pseudorapidity, or η is used in place of θ, and is given by $\eta = -\ln[\tan(\theta/2)]$ which can also

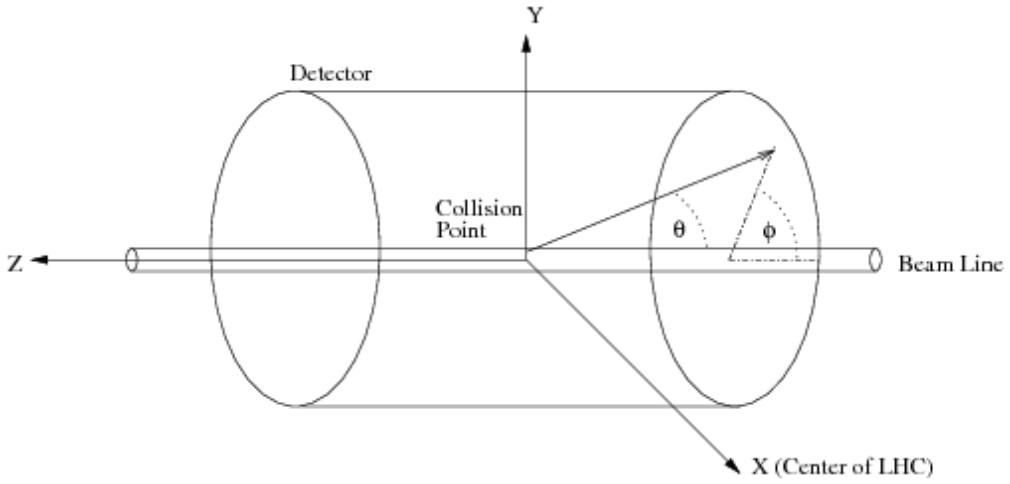

Figure 2.4: ATLAS detector coordinate system. The z-axis is along the beam pipe, the x-axis points radially inward to the center of the LHC ring, and the y-axis points directly upwards. In cylindrical coordinates, the azimuthal angle ϕ is in the x-y plane parallel to the end caps of the detector, and the azimuthal angle θ is in the y-z plane [40].

be expressed in terms of momentum by $\eta = \frac{1}{2}ln(\frac{|\mathbf{p}|-p_z}{|\mathbf{p}|-p_z})$. This produces a Lorentz invariant quantity that directly translates to the COM frame of the collisions. A representation of values of η are shown in Figure 2.5, with increasing η pointing more towards the beam pipe.

2.2.1 Detector Layout

The detector is built to determine the types of particles and their energy and momentum. It's broken down into three layers - inner tracking detectors, calorimeters, and a muon spectrometer. The inner detectors measure momentum, charge, and precision tracking of any charged particle. The calorimeters measure energy of electromagnetic particles and hadrons. Finally, muons will have minimal interaction with either calorimeter, as they are minimally ionizing particles, so a dedicated muon spectrometer will measure muon momentum. Neutrinos will not interact with any part of the detector, and therefore will pass through undetected. Their

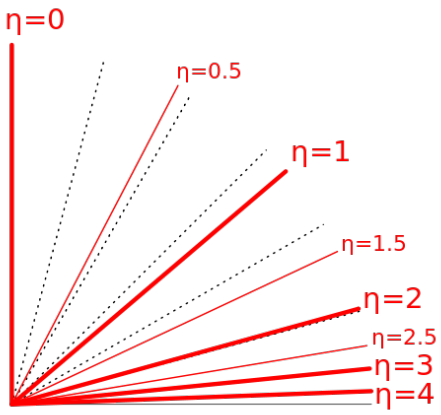

Figure 2.5: Representation of pseudorapidity η in the x-y plane of the detector [42].

presence in collisions can be determined by the amount of missing momentum, usually called missing transverse energy (MET or E_T). A cross sectional view of the detector with examples of which particles will be detected in each piece of the detector is shown in Figure 2.6.

2.2.2 Inner detector

The inner most region of the detector, used to measure impact parameters, momentum, and charge, has three main components. There are two precision trackers, the pixel detector and semiconductor tracker (SCT), with the main purpose to resolve impact parameters and vertex position, as well as identify b-quarks. The third component of the inner detector is the transition radiation tracker (TRT), which allows for longer tracks and therefore better momentum resolution. Throughout all pieces of the inner detector, the readout electronics must be fast enough to keep hits from each bunch crossing separate. Finally, the inner detector is surrounded by a superconducting solenoid field of 2T, which allows for momentum calculation and particle identification. The layout can be seen in Figure 2.7. Information in

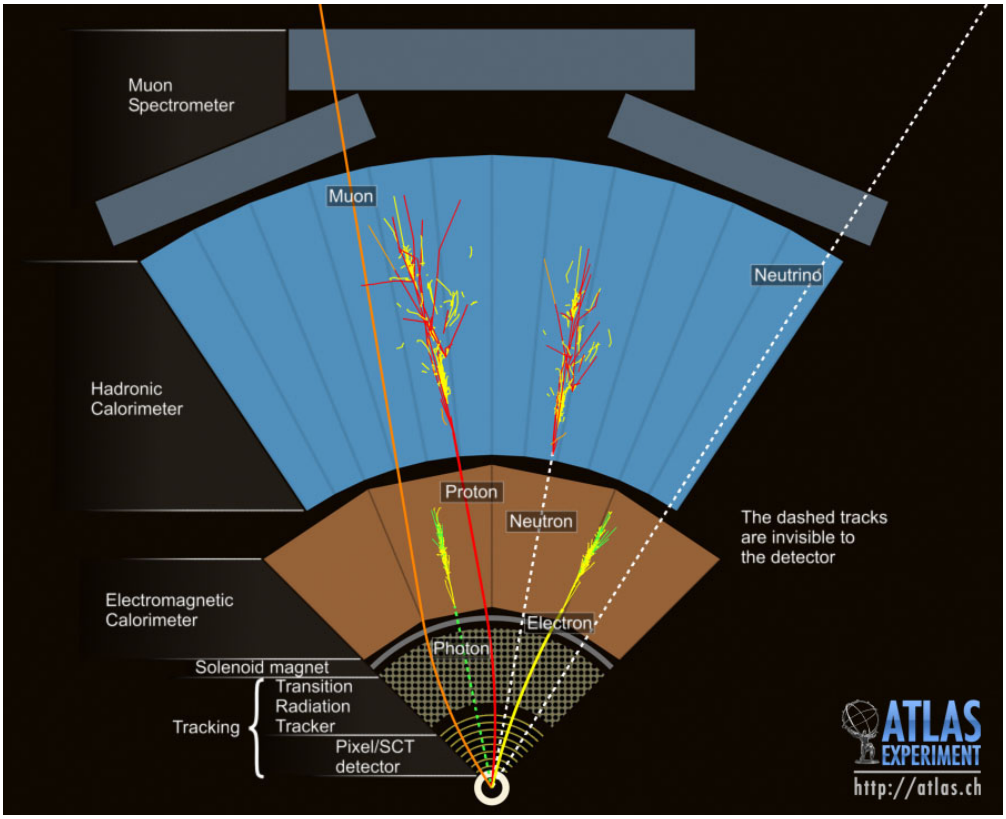

Figure 2.6: A cross sectional view of the ATLAS. Neutral particles such as neutrons and photons do not leave tracks in the inner detector, while charge particles are bent with the solenoid field. Electromagnetic particles such as electrons and photon deposit their energy in the electromagnetic calorimeter, while hadrons deposit energy in the hadronic calorimeter. Muons are detected in the inner detector due to their charge, but are minimally ionizing through the calorimeters, and gets detected in the muon spectrometer. Neutrinos escape undetected. Image under CERN copyright.

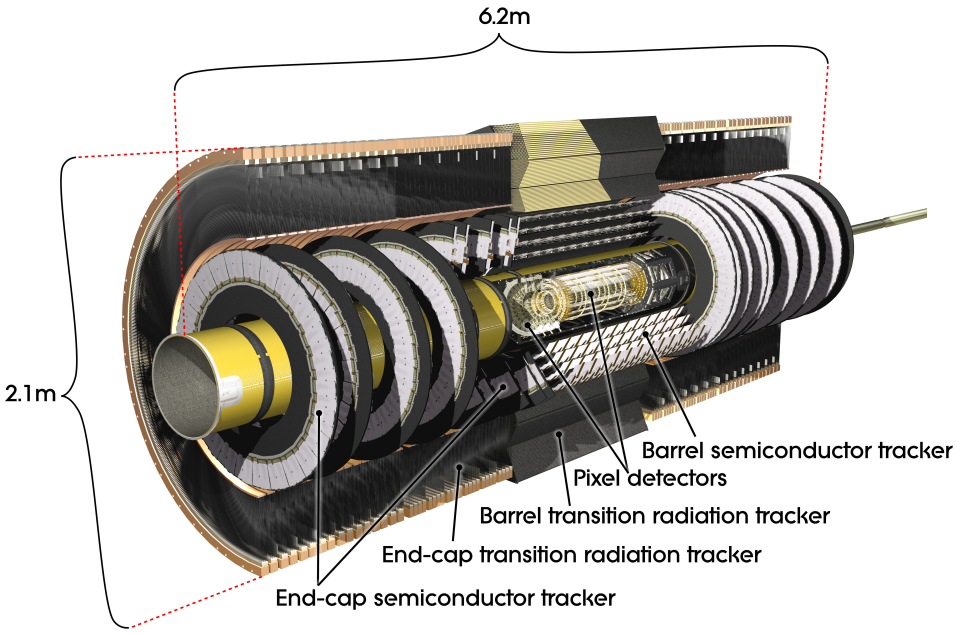

Figure 2.7: The ATLAS inner detector with barrel and endcap pieces of the pixel detector, semiconductor tracker, and transition radiation tracker [40].

this section is borrowed from the inner detector technical design report [43].

Pixel Detector

The pixel detector measures 50.5 - 150mm radially and covers the range of $0 < |\eta| < 2.5$. It consists of three barrel layers and six disks, with three disks on each end cap, as can be seen in Figures 2.9. This allows for 3 hits per particle, which are read out if above some noise threshold. The detector is made of modules, where each module is 6x2cm and consists of $\sim$ 45000 pixels, where each pixel is 50×400 microns in $\phi - z$. Each module is pitched in ϕ about 20 degrees and slightly overlapping to have complete coverage in ϕ as seen is Figure 2.8. The endcap modules are also pitched about 20 degrees, but modules are laid out radially from the beam pipe, with modules on both sides of the disk and slightly offset from each other. Each

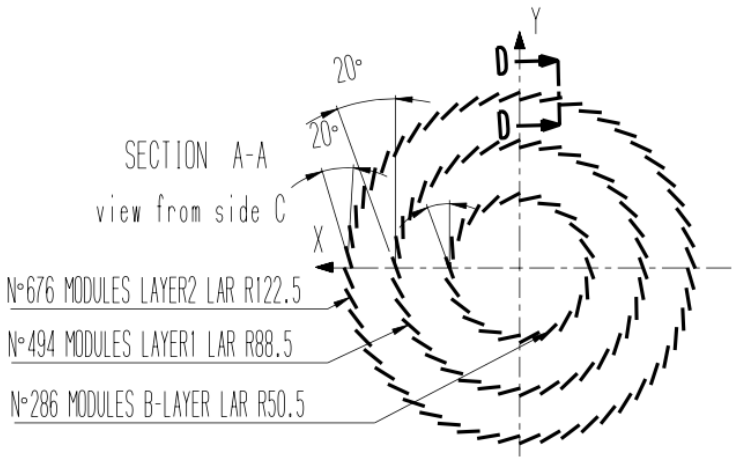

Figure 2.8: The Pixel detector module layout, where modules are placed in concentric cycles and pitched at 20 degrees [44].

module has these silicon sensors, 16 front end chips, and a module controller chip. All details presented here and more can be found in the pixel detector technical design report [44]. To protect the first layer of the pixel detector from getting too much damage from radiation, an additional pixel detector as inserted between it and the beam pipe in the first long shut down [45]. The insertable b-layer (IBL) is 33mm out from the center of the detector, and covers out to $|\eta| < 3$. It has a reduced pixel size and its proximity to the collision make it better at impact parameter measurements, and therefore better at detecting b-quarks.

Semiconductor Tracker

The SCT sits at 288-560mm, covering out to $\eta < 2.5$. It is similar in design to the pixel detector, but uses silicon strips rather than pixels to gather tracking information. It consists of 4 barrels, and 9 disks on each endcap, once again as seen in Figures 2.9. Two silicon strips

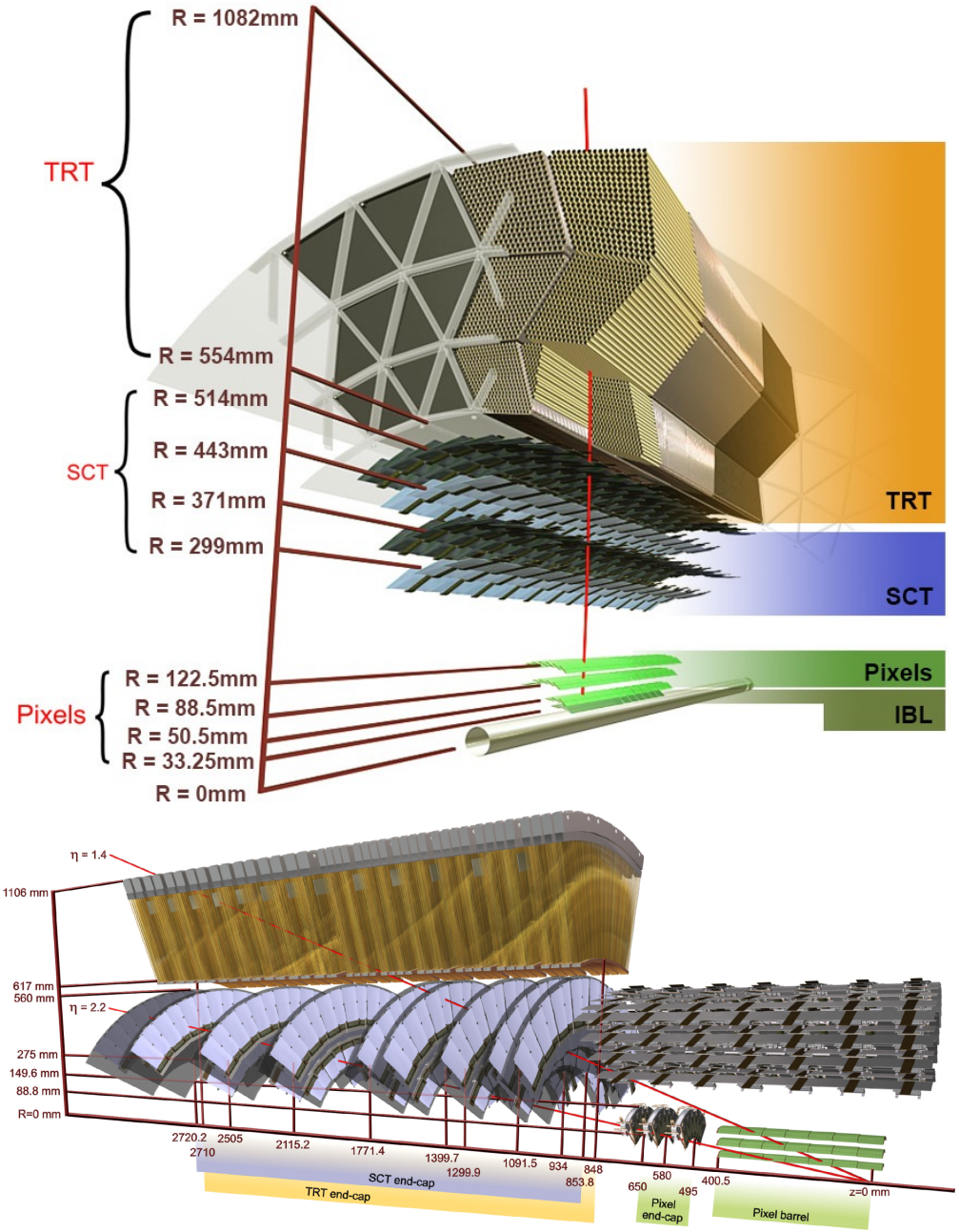

Figure 2.9: All components of the ATLAS inner detector laid out radially (top) and longitudinally (bottom) with radial depth information of each component [46].

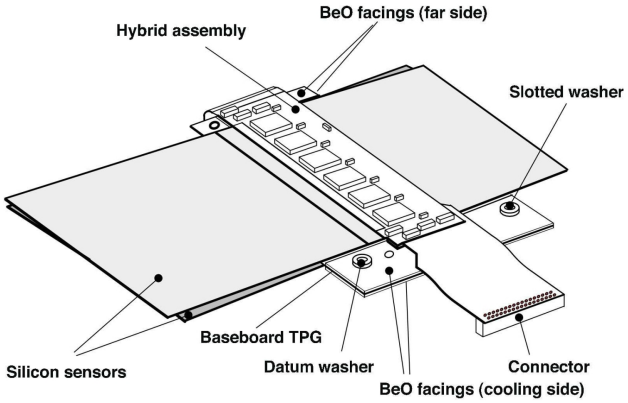

Figure 2.10: SCT module with silicon strips placed back to back at a tilt of 40mrad, as can be seen in the slight offset of the silicon sensors [46].

are connected on one side of each module, and two others are places on the backside, tilted at 40 mrad from the front, as seen in Fig. 2.10. This assures particles will hit at least 8 strips to produce 4 space point measurements. The front layer strips are parallel to the solenoid field and beam axis, which allows measurement of $R - \phi$, while the stereo angle of the back allows for measurements in z. Each strip is 80 microns x 12 cm, and pitched at 80 microns, and in total there are 768 such strips. The end cap is similar to the barrel, however strips radiate out from the beam pipe rather than being parallel.

Transition Radiation Tracker

The final layer of the Inner Detector is the TRT. It sits farthest out at 563-1066mm, and covers a smaller range in η out to $|\eta| < 2$. The TRT has 3 cylindrical layers in the barrel and 9 wheels in each endcap, both of which are filled with drift tubes that are 4mm in diameter (Figures 2.9). These are parallel to the beam axis in the barrel, and radial in the end caps. The straws are filled with a gas mixture of xenon, CO_2, and O_2, with polypropylene fibers in between in the barrel, and polypropylene foil in the end caps. The change in this

material causes the transition radiation, which is used to discriminate between pions and electrons. On top of particle discrimination, the TRT greatly aids in the determination of the momentum of particles. Particles hit on average 30 straws and extends farther out, giving a longer track length for which to calculate the momentum.

2.2.3 Calorimeters

There are two calorimeters in the ATLAS detector, the liquid argon (LAr) and hadronic (Figure 2.11). Both calorimeters are sampling calorimeters, layering passive materials that facilitates the showering of particles with active material that is used to measure the energy deposited. In these calorimeters, active material will be liquid argon or plastic scintillators, while passive layers are lead or tungsten. Interwoven with the active material will be a read out method that passes an analog signal proportional to the resulting radiation to front end electronics. The LAr calorimeter was built to contain the full shower of electrons and photons, while hadronic showers will continue to extend through to the hadronic calorimeter. Much of the technical information in these sections can be found in the technical design reports, Ref. [47] and Ref. [48].

EM Calorimeter

The EM calorimeter is the inner most calorimeter, bordering the inner detector. It has LAr as the active material and lead as the passive material, with these layers being folded in an accordion shape radially for azimuthal symmetry. There are three main components to the LAr calorimeter, a barrel (EMB) extending out to $|\eta| < 1.475$, and two end caps (EMEC), covering the region $1.375 < |\eta| < 3.2$. The EMB extends radially out between 1.15 - 2.25 m, and has three sampling layers. The first sampling layer, closest to the ID, has a granularity of 0.003 x 0.1 in $\eta - \phi$ and an interaction length of 4.3 X_0. This layer has a higher granularity

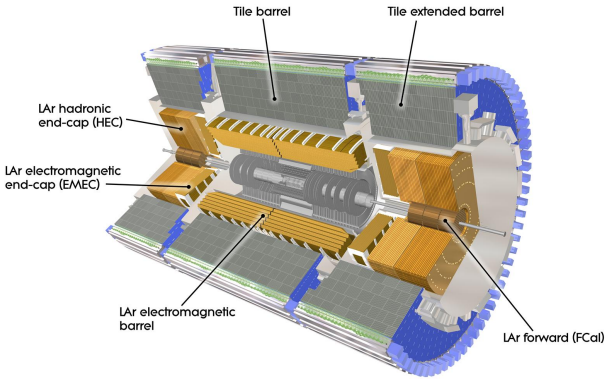

Figure 2.11: A sketch of the EM and Hadronic calorimeters [49].

in η then the rest the calorimeter to distinguish between photons and π_0, while elongating through ϕ to keep the number of channels low. The bulk of the calorimeter (16 X_0) consists of square cells of 0.025 x 0.025 in $\eta - \phi$, and make up the second sampling layer, and the third sampling layer contains strips of 0.025 x 0.05 in $\eta - \phi$ with a radiation length of 2 X_0. A slice of the EMB can be seen in Figure 2.12. The EMEC are of a similar layout, with three sampling layers of varying granularities (Table 2.1). Finally, there is a presampler layer, which consists of only an active LAr layer to recover and correct for energy lost in dead material before the calorimeters. This layer exists between both the barrel and end caps, and covers a range of $\eta < 1.475$ in the barrel and $1.5 < \eta < 1.8$ of the end cap. Beyond $\eta > 1.8$ the higher energies and smaller amounts of dead material make the presampler layer unnecessary.

As charged particles pass through the lead layers, they interact with nuclei in two ways - through bremsstrahlung radiation, where an electron radiates a photon, or pair production of ee^-. This creates a shower of particles that continue on into the LAr. Copper electrodes are run through the liquid argon, and as the particles ionize the argon, the resulting electrons move to the electrodes by an applied magnetic field. The number of electrons is proportional

Sampling	**Barrel Granularity** ($\Delta\eta \times \Delta\phi$)	**Endcap Granularity** ($\Delta\eta \times \Delta\phi$)
Presampler	0.025 x 0.1, $\|\eta\| < 1.52$	0.025 x 0.1, $1.5 < \|\eta\| < 1.8$
Sampling 1	0.003 x 0.1, $\|\eta\| < 1.475$	0.025 x 0.1, $1.375 < \|\eta\| < 1.5$
		0.003 x 0.1, $1.5 < \|\eta\| < 1.8$
		0.004 x 0.1, $1.8 < \|\eta\| < 2.0$
		0.006 x 0.1, $2.0 < \|\eta\| < 2.5$
		0.1 x 0.1, $2.5 < \|\eta\| < 3.2$
Sampling 2	0.025 x 0.025, $\|\eta\| < 1.475$	0.025 x 0.025, $1.375 < \|\eta\| < 1.5$
		0.1 x 0.1, $2.5 < \|\eta\| < 3.2$
Sampling 3	0.05 x 0.025, $\|\eta\| < 1.475$	0.05 x 0.025, $1.5 < \|\eta\| < 2.5$

Table 2.1: Sampling layers of the EM calorimeter, showing the part of the detector in η covered by each layer, and the granularity of each layer.

to the energy deposited, and creates a triangle shaped pulse that is fed to readout electronics [50]. This pulse is then shaped using a bipolar filter, sampled at 4 points that are 25ns apart, and stored in analog form until the Level 1 trigger decision (Section 2.3). If the event is accepted, it is passed through an analog to digital converter and stored.

2.2.4 Hadronic Calorimeter

The hadronic calorimeter is built to contain the energy of hadronic showers. While approximately 2/3 of the hadron shower's energy is deposited in the LAr calorimeter, showers still extend past the 2 nuclear interaction lengths in the LAr calorimeter. The hadronic calorimeter extends to 10 interaction lengths, enough to contain a large majority of showers. The hadronic interaction length is longer than the EM interaction length, resulting in the design of the HCAL being denser and deeper than the LAr calorimeter, with a depth approximately twice as long as the LAr calorimeter at 2.3-4.8m. Similar to the EM calorimeter, there is a central and end cap piece of the calorimeter. The Tile calorimeter, or central calorimeter, consists of the barrel ($|\eta < 0.8$) and extended barrel ($0.8 < \eta < 1.7$). They are composed of plastic scintillator tiles layered with steel absorbers pieced together in wedges that surround the beam pipe. The Tile calorimeter also contains three sampling layers, ranging in interac-

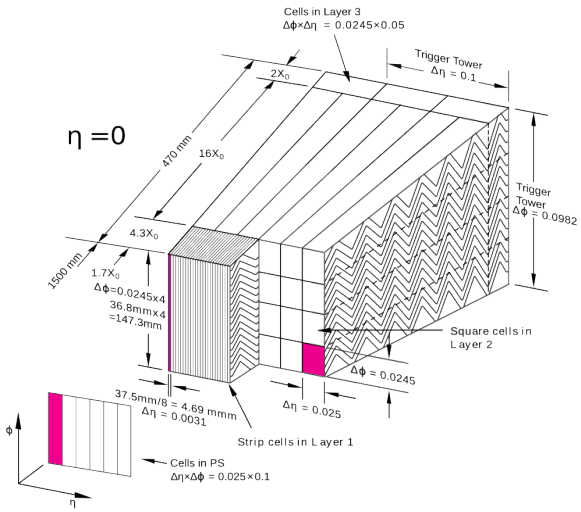

Figure 2.12: A slice of the EM barrel calorimeter, showing granularity and radiation lengths of the sampling layers [47].

tion length and granularity, as seen in Table 2.2 [51]. In the active phase, incoming particles will excite molecules within the scintillator material, which will in turn emit UV light upon de-excitation. This light is then reabsorbed by a secondary material and re-emitted at a lower wavelength, which will then be sent through optical fibers to photomultiplier tubes (PMTs) outside the calorimeter. The light produced will be proportional to the energy of the incoming particle - the resulting analog pulse from the PMTs with have an amplitude proportional to the energy. This pulse is then passed to a shaper and compressor, and digitized. This signal is sampled 7 times and sent to read out electronics for further use. In the passive layers, the steel showers electromagnetic particles produced from hadronic showers in the same way the lead layers of the LAr calorimeter did. Strongly interacting particles in the shower will deposit energy through ionization, nuclear breakup, nuclear recoil, neutron generation, and photon generation. In the more forward region of $|\eta| > 1.5$, the hadronic end caps (HEC) replace the barrel, with LAr used in place of scintillator tiles and copper plates are layered in between, perpendicular to the z-direction.

Sampling	**Barrel Granularity** ($\Delta\eta \times \Delta\phi$)	**Endcap Granularity** ($\Delta\eta \times \Delta\phi$)
Barrel Sampling 1	0.1 x 0.1, $\lvert\eta\rvert < 1.0$	0.1 x 0.1, $0.8 < \lvert\eta\rvert < 1.7$
Barrel Sampling 2	0.1 x 0.1, $\lvert\eta\rvert < 1.0$	0.1 x 0.1, $0.8 < \lvert\eta\rvert < 1.7$
Barrel Sampling 3	0.2 x 0.1, $\lvert\eta\rvert < 1.0$	0.2 x 0.1, $0.8 < \lvert\eta\rvert < 1.7$
Endcaps Sampling 1-4	- -	0.1 x 0.1, $1.5 < \lvert\eta\rvert < 2.5$ 0.2 x 0.2, $2.5 < \lvert\eta\rvert < 3.2$

Table 2.2: Sampling layers of the hadronic calorimeter, showing the part of the detector in η covered by each layer, and the granularity of each layer.

Sampling	**Barrel Granularity** ($\Delta\eta \times \Delta\phi$)	**Endcap Granularity** ($\Delta\eta \times \Delta\phi$)
Sampling 1-3	- -	0.2 x 0.2, $3.1 < \lvert\eta\rvert < 4.9$

Table 2.3: Sampling layers of the forward calorimeter, showing the part of the detector in η covered by each layer, and the granularity of each layer.

Finally, there is a forward calorimeter (FCAL) [52] to cover the most forward region of the detector, from $3.1 < |\eta| < 4.9$, built to handle large amounts of radiation from the high flux of particles in the forward region. There are three layers to handle electromagnetic and hadronic showers; the first layer is composed of copper absorbers, and the second two composted of tungsten, all 45cm thick. Because of the onslaught of particles, the FCAL must be extremely dense to capture all radiation, so LAr is used as the active material and is placed in channels parallel to the z-axis cut into the passive material. A rod is placed in the middle of each channel and is held at high voltage, and a small layer of space between the rod and the passive material is used as the active gap. A layout can be seen in Figure 2.13, and the schematics are shown in Table 2.3.

2.2.5 Muon spectrometer

The outer most region of the ATLAS detector is the muon spectrometer (MS) [53][54], build to exclusively measure muon momentum and position. The MS is split into a central region composed of three concentric cylinders at radii of 5m, 8m, and 10m, and covering the range

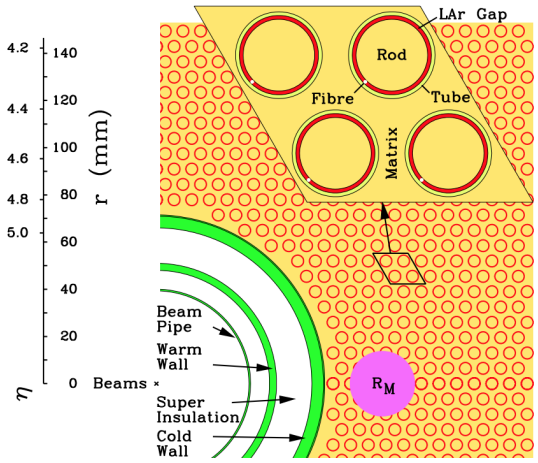

Figure 2.13: Layout of the FCAL, with rods surrounded by a layer of LAr, then a gap, interwoven in a dense passive material around the beam pipe [47].

$|\eta| < 1.4$, and two end caps made of four wheels each covering the region from $1.4 < |\eta| < 2.7$. The muon chamber is split into two functions, triggering and tracking. Monitored drift tubes (MDT)[55] are the main tracking mechanism, providing precision tracking information for momentum measurements. It is composed of 3 cm diameter drift tubes containing a mixture of argon and CO^2, and a tungsten-rhenium wire to measure drift time of ionization charge produced by muons. MDTs are used in the barrel and the three outer wheels of the end caps, out to $|\eta| < 2$. In the more forward region, in the inner most end cap wheel, cathode strip chambers (CSC)[56] are used for tracking, as there is a need for higher precision to combat the higher background. The CSC is a multi-wire proportional chamber[57], with anode wires that run radially out and cathode strips parallel to the beam pipe, surrounded by a gas mixture of Ar and CO_2. The inner most wheel is composed of 8 small and 8 large overlapping wedges of CSC.

The time for precision readings from the tracking components can take upwards of 700 ns, far longer than the bunch spacing. There is therefore a need for fast measurements, which

are collected by the trigger components of the MS. The resistive plate chamber (RPC) [58] is used for finer spatial measurements, and is layered in the middle and outer cylinders of the barrel out to $\eta < 1.05$. Parallel electrode plates filled with a gas mixture, in which any charged particle crossing through the gas will create electron cascades. In the end caps thin gap chambers (TGC) replace the RPCs for tracking. TGCs are also multi-wire proportional chambers[57], with graphite cathode strips and a gas mixture of CO_2 and $n - C_5H_{12}$. All components can be seen in Figure 2.14.

The MS has three toroidal magnets, one around the barrel and one for each end cap. These magnets provide an average magnetic field of 0.5 T. The bending of the muons through these fields allows for measurement of the momentum. Three hits in the tracker create an arc, and the sagitta is directly proportional to the muon momentum. In the end caps, the direction between the interaction point and the inner layer is compared to that of the middle and outer layer to get momentum measurements.

2.3 Trigger

Not all collisions can be saved, and even then all information from "good" collisions cannot be saved. Therefore, a system of hardware and software was constructed to quickly save only interesting data, while discarding all other events. The level 1 trigger (hardware)[59] accepts reduce the rate from 40MHz to 100 kHz, and is built for speed. It performs a low resolution search for physics objects, such as jets, MET, and leptons, and quickly computes the total energy deposited for that object, using information from the calorimeters and muon spectrometer. The triggered object must pass some unique selection, or trigger item, such as at least one jet with $E_T > 50$ GeV. Muons are chosen from a coincidence of hits in several layers of the MS, while other particles are determined through construction of trigger towers. Trigger towers are the analog summation of cells within 0.1 x 0.1 (or larger, in

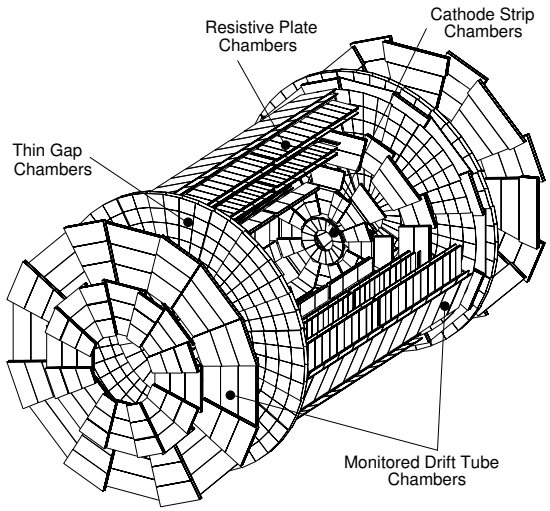

Figure 2.14: Layout of the muon spectrometer [54].

forward regions) $\eta - \phi$ slices of the detector, that extend radially to the full length of the shower (Fig. 2.15). Sliding bunches of 4x4 trigger towers are used to determine if a particle of interest is present. Electron and photon triggers sum all 1x2 or 2x1 pairs of trigger towers in the center of this 4x4 window. If the E_T threshold is large enough to pass the trigger criteria, the shower does not extend into the hadronic calorimeter, and the shower is isolated, meaning the 12 cells surrounding the 2x2 core have a sufficiently low energy deposit, the trigger is considered passed. Taus and hadrons are triggered similarly, however these 1x2 or 2x1 pairs are then added to the 2x2 core of trigger towers in the hadronic calorimeter.

Wherever an object is detected in the Level 1 trigger it is defined as a region of interest (ROI)[60], which is used to seed level 2 trigger reconstruction. If the unique combination of physics object and kinematic selection are not met, the event is discarded. If the event is selected, it is relayed to the front end electronics to read out the digitized collected information. This information is then passed to the software based high level trigger (HLT)

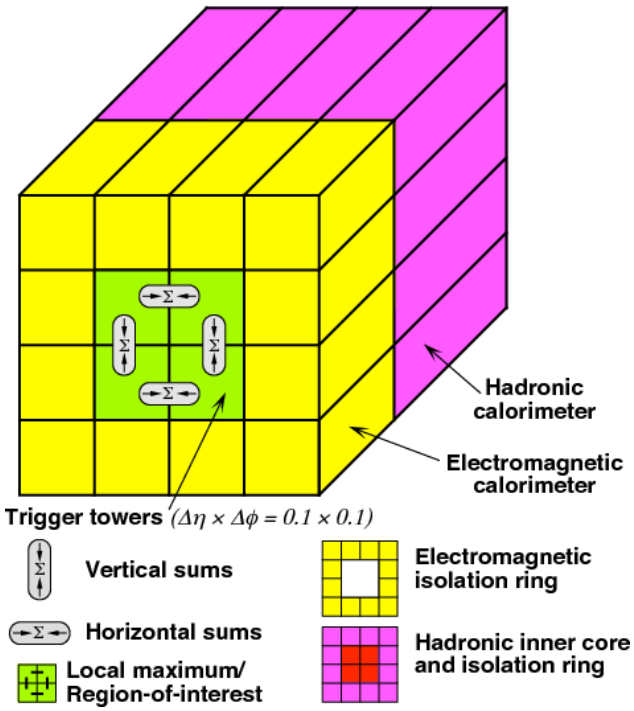

Figure 2.15: Trigger tower layout, where each trigger tower is a 0.1×0.1 block in η and ϕ. The trigger region of interest is surrounded by a 4×4 window of trigger towers [59].

[61], that saves events at a rate of 1 kHz. The HLT iteratively attempts to reconstruct the event, pulling more information from the ROI and read out electronics as it goes if it is determined the object is worth keeping. Due to improvements in triggering in Run II, high level jet triggers now make use of the entire calorimeter. Jets are constructed using the anti-kT algorithm [62], the same algorithm used for offline jet reconstruction (Section 3.1.1), and take topological clusters as inputs. Topological clusters start from a seed cell that has a signal to noise ratio (S/N) above 4 [63]. Any cells surrounding the seed cell with a $S/N > 2$ are added into the cluster, and finally the next closest cells are added in.

At the HLT, the particle may be required to pass an even higher energy threshold to be kept. These unique trigger requirements from both level 1 and the HLT form a trigger chain, and each analysis uses at least one such trigger chain to reduce their dataset [64]. For example, the dijet analysis uses the trigger HLT_j380 seeded with the L1_j100 trigger, meaning events where there was at least one jet with $E_T > 100$ GeV in the L1 trigger and at least one jet with $E_T > 380$ GeV recorded in the HLT are kept. Most events are written to the "main" steam, but some that may take longer to reconstruct are written to the "debug" stream to be processed later.

Even after the trigger system reduces the amount of saved events, this still doesn't reduce the collected data to a storable amount. For instance, jets are produced with such abundance that saving all lower momentum jets would still crowd the bandwidth. Therefore, each unique trigger may also be assigned a prescale (p), where every 1/p events are saved. The lowest unprescaled trigger is then the lowest in E_T a trigger can go without being prescaled.

2.4 Monte Carlo

A prediction of SM physics is needed for many stages of ATLAS analyses. It is used in background predictions, as signal model templates, for calibration purposes, and as a test set for analysis decisions, so as to remain unbiased with real data. ATLAS uses Monte Carlo (MC) simulators to predict the physics events seen at the detector, using probability distributions at discrete steps to produce the entirety of the collision. This analysis uses Pythia 8.186 [65] with leading-order PDF set NNPDF2.3 LO [30]. Pythia uses the DGLAP splitting functions as described in Section 1.3 to model parton showers, and the Lund string fragmentation model [31] as its hadronization model. Pythia steps through an event in three generalized steps. The first is the hard process, calculating matrix elements perturbatively. The next step includes all other parton level activity, from ISR/FSR, to multiple parton interactions and beam remnants. Finally, hadronization and the subsequent decay of unstable particles is modeled, both of which are non-perturbative in nature. As mentioned in section 1.3, there are many parameters in PDF and MC generations that must be tuned to real data, and have the ability to change even within PDF and MC generators. The tune used for this analysis is the A14 tune [66], which is based on data collected in the earlier runs of ATLAS data taking at $\sqrt{s} = 7$ TeV.

Besides modeling the physics processes, simulations should also include detector response effects to accurately model the collected data. This is done with GEANT4 [67][68]. GEANT4 has a collection of data from many collaborations and experiments to help model everything from particle interaction in detector material, to particles in electromagnetic fields, to the physics processes governing all particle interactions. At this stage, both MC and data are run through the same reconstruction software package called ATHENA [69].

2.4.1 Signal Models

The new physics models searched for in this analysis have dedicated MC production of their own. Excited quark and W' are produced similarly in PYTHIA 8 with the same tunes and PDF sets as listed above. For the excited quark model, all possible final states (gq, $q\gamma$, qW, qZ) are allowed, and production of the q^* are allowed from both light flavors and b quarks. The compositeness scale is set to the q^* mass, and all couplings are assumed to be the same as SM quarks. MC templates for mass points from 2 TeV to 7 TeV in steps of 500 GeV are simulated. The Z' model samples are produced at various Z' masses ($m_{Z'}$= 1500, 2000, 2500, 3000, 3500) and couplings to quarks (g_q=0.1, 0.2, 0.3, 0.4, 0.5) using both MADGRAPH [70] and Pythia. The dark matter mass is fixed to 10 TeV, and the coupling to dark matter is fixed at $g_{DM} = 1.5$. W' is restricted to decay to only qq pairs for all six quark flavors, and is assumed to have SM couplings. W' samples are generated at (1, 1.2, 1.5, 1.7, 2, 2.5, 3, 3.5, 4, 4.5, 5, 5.5, 6, and 6.5) TeV masses. QBH models use the generator BLACKMAX [14] with PDF set CTEQ6L1 [71] to produce QBH at M_D energy thresholds of (4, 5, 5.5, 6, 6.5, 7, 7.5, 8, 8.5, 9, 9.5, and 10 TeV) with an ADD model with n=6 extra dimensions. Finally, W^* samples are generated with the CALCHEP 3.6 generator [72] with NNPDF2.3_NLO PDF, and passed to PYTHIA 8 for hadronization. Leptophobic W^* of masses 1.8 - 4 TeV in steps of 200 GeV were produced.

Chapter 3

Jet calibration

3.1 Jet calibration

Quarks and gluons form jets, a spray of particles from hadronization and parton showers that must be grouped together and calibrated to get the correct energy, momentum, and direction of the initial quark or gluon. The process starts with the formation of a jet through clustering particles together, then goes through a series of energy calibrations.

3.1.1 Jet algorithms

As discussed in Section 2.3, topological clusters are the building blocks for jets, and are an attempt to represent individual particles that shower through the calorimeter. To combine them into a jet, a clustering algorithm must be used. The requirements of a clustering algorithms are that they be infrared and collinear safe, meaning algorithms should give the same jet regardless of the hadronization process. The clustering algorithms cluster topoclusters based on distance between the topocluster and pseudo jet (d_{ij}), and the topocluster

and beam (d_{iB}), where the pseudo jet is the clustered jet up until step. These are given by $d_{ij} = min(k_{ti}^{2p}, k_{tj}^{2p})\frac{\Delta_{ij}^2}{R^2}$ and $d_{iB} = k_{ti}^{2p}$, where $\Delta_{ij} = (y_i - y_j)^2 - (\phi_i - \phi_j)$, and k_{ti}, y_i, and ϕ_i are the transverse momentum, rapidity, and azimuthal angle of particle i, and R is some chosen radius of the jet, usually 0.4 or 0.6. $p = 1$ corresponds to the k_T algorithm [73], $p = 0$ the Cambridge/Aachen (C/A) algorithm [74], and $p = -1$ to the anti-kt algorithm [62], which is currently used. After each topocluster is added the momentum and position of the pseudo jet is recalculated. The algorithm compares d_{ij} and d_{iB}; if d_{ij} is the smallest of the two, the topocluster is added into the jet, and if d_{iB} is the smallest, the topocluster i is considered a jet and removed from further computations. The k_T algorithm clusters soft particles together first, building from lowest p_T topoclusters to highest p_T. This causes an irregular shape in the jet area, as soft particles can be scattered around the center of the jet. The $p = 0$ C/A algorithm has no relation to the particle p_T, and so only clusters based on proximity. This results in close particles being clustered first, and also an irregular shape in the final jet area. By having $p = -1$, the anti-kt algorithm clusters soft particles to hard particles first, resulting in a circular shape jet area, as the particles cluster around a central hard particle. Therefore if a hard particle has no neighboring hard particles within $\Delta_{12} < 2R$, a perfectly conical jet centered around the hard particle is formed. If a second hard particle is within $R < \Delta_{12} < 2R$, there will be two jets with uneven boundaries. And finally, if two hard particles exist within the same radius $\Delta_{12} < R$, the two will be clustered together to form one jet, with the cone of the jet being some combination of the cones around each particle. The anti-kT algorithm has the advantage of being circular, and while not required of a jet, makes the jet easier to calibrate, as jet shape does not have to be taken into account.

3.1.2 Truth Jets, Track Jets, Calorimeter Jets, Reconstructed Jets

The purpose of calibrating jets is to get the reconstructed energy as close to the truth energy as possible, and for parts of the calibration truth jets are used as the reference object to compare to.

Truth jets are formed from anti-kt clustering stable, final state particles from MC. These particles must have a lifetime of $c\tau > 10mm$ and excludes muons and neutrinos. In order to accurately compare MC and data, truth jets will have the same calibration applied as that applied to data.

Track jets are formed from charged particle tracks in the ID that originate from the primary vertex. These tracks must pass a series of quality criteria to be considered, including p_T and η requirements ($p_T^{track} > 500MeV$ and $|\eta| < 2.5$), impact parameter selections to ensure the track originated from the primary vertex, and a criteria on the number of hits in both the pixel and SCT detectors. To use as a comparison tool, these jets are similarly clustered using anti-kt. As these jets are not sensitive to pileup, they are used in pileup calibration of calorimeter jets, and there are no corrections applied to these measurements.

Reconstructed jets (or reco jets) are jets built from topoclusters, and go through the full calibration procedure. The steps below explain the calibration procedure of these jets.

3.1.3 EM+JES calibration

Jet energies are calculated at the EM scale, meaning there are no corrections for hadronic loses that cause lower response to hadrons then EM particles (non-compensation). A p_T and η dependent scaling based off a comparison of truth jets in MC to reconstructed jets coverts

the EM calibration to a hadronic scale [75]. There are several areas where energy is lost or miscalculated that needs to be taken into account in this calibration sequence. One area is in the clustering of the jet itself, where energy can be left outside of the final clustered object. Or, there can be a deficit of energy from energy deposits below the noise threshold, resulting in them being left off the topocluster. Another area of loss is the calorimeter, where energy can be lost to dead material such as malfunctioning modules or cracks, or energy can leak out of the edges of the calorimeter or into the muon spectrometer. Particles can also lose energy in the inner detector, or other upstream material. Finally, energy measurements are disrupted by pileup, that must be estimated and removed from the jet [76].

Local Cluster Weighting

Local Cluster Weighting (LCW) is an alternative initial step in jet calibration, applying corrections to topoclusters rather than the entire jet, bringing topoclusters to the hadronic energy level [77]. This more accurately corrects jets as calibrations are applied at a finer resolution. Things like energy deposits outside of the jet are now calculated on a cluster level, as well as the response of the calorimeter and dead modules. These jets still go through the same calibration procedure, with the following methods being applied to both EM and LCW jets. A comparison of the energy response between LCW and EM jets before any calibration is shown in Figure 3.1, where it can be seen that the energy response is more uniform in LCW due to the corrections applied at topocluster level.

Origin Correction

The calorimeters only measure energy, so when 4-vectors are assigned to a topocluster or trigger tower, it is assigned to point to the center of the detector until the full event is reconstructed. There then must be a correction to point the jet back to its creation point,

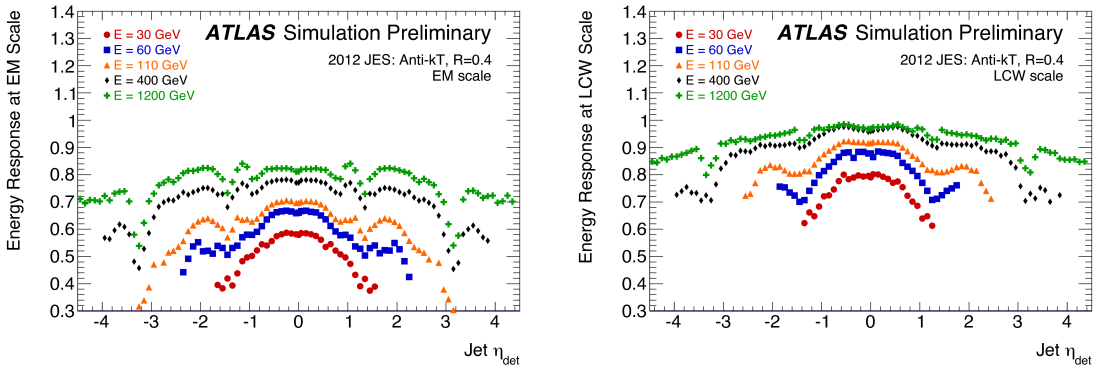

Figure 3.1: Energy response of EM jets (a) and LCW jets (b) before any calibration. As LCW calibration hasn't been done at 13 TeV, this presents these quantities as simply a comparison at 8 TeV [76].

or the primary vertex, and this is done as the first step of the calibration. The energy is kept the same, but the 4-vector is modified to point to the hard scatter vertex.

Pileup Suppression

The energy of the jet must be corrected for any pileup that may have deposited energy in or around the jet. The first step is to measure an "ambient" pileup energy ρ, which is an estimate of the soft elements of pileup [78][79]. This is assumed to be distributed evenly throughout the detector, so an area correction is applied as $p_T^{corr} = p_T^{jet} - \rho \times A$ where A is the area of the jet. ρ is the median p_T density of jets in the region $|\eta < 2$, that are clustered with the k_T algorithm instead of anti-kT, as this clusters soft radiation together first (see Section 3.1.1). A residual correction is applied based on the number of primary vertices (N_{PV}), also known as in time pile up, and pileup from older collisions, or out of time pileup (μ) as some correlation between the two remains [78]. The full correction is then $p_T^{corr} = p_T^{ref} - \alpha \times (N_{PV} - 1) - \beta \times \mu$, where α and β are the coefficients relating the residual p_T dependence to N_{PV} and μ respectively. These corrections are shown in Figure 3.2.

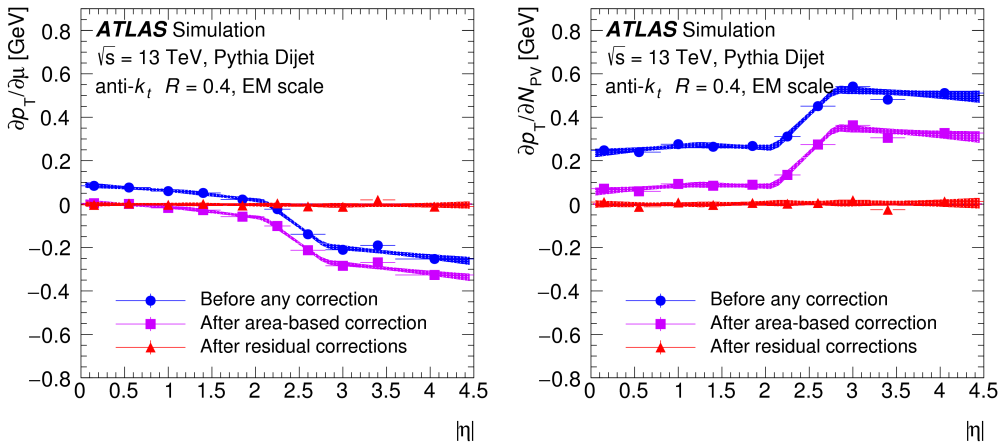

Figure 3.2: The p_T dependence on out of time (a) and in time (b) pileup corrections as a function of $|\eta|$ before any corrections, after area based corrections, and after residual corrections [80].

To handle hard QCD pileup, a second approach is taken. The Jet Vertex Tagger (JVT) [81] combines several variables in a likelihood estimation to decide if a jet is pileup or not. These variables contain track momentum information (P_T^{trk}), which can discriminate if the jet came from the hard scatter of the primary vertex (PV_0) or a secondary vertex (PV_n). $corrJVT$ and R_{pT} are the two variables used in the JVT calculation, and are described in Eq. 3.1. JVF is applied to jets only up to 60 GeV, as hard pileup only manifests at this lower energy range.

$$
\begin{aligned}
corrJVF &= \frac{\sum_k P_T^{trk_k}(PV_0)}{\sum_k P_T^{trk_l}(PV_0) + \frac{\sum_{n\geq 1}\sum_l P_T^{trk_k}(PV_n)}{k.n_{trk}^{PU}}} \\
R_{pT} &= \frac{\sum_k P_T^{trk_k}(PV_0)}{P_T^{jet}}
\end{aligned}
\tag{3.1}
$$

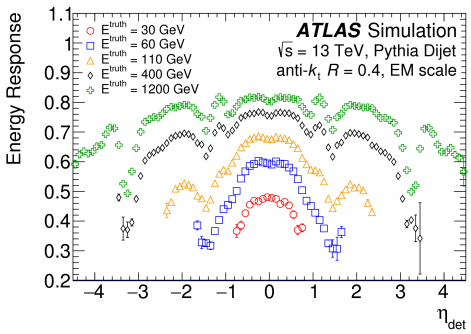

Figure 3.3: The energy response ($R = E_{reco}/E_{truth}$) as a function of $|\eta_{det}|$. The calibration constant applied to the jet energy is then 1/R for each (E_T^{truth}, $|\eta_{det}|$) bin [80].

MC JES

The next step adjusts the jet 4-vector to particle level using MC truth information to calibrate energy across p_T and η, where η biases mostly come from different detector geometry having varying response [75]. Truth jets have pile up and origin corrections applied, to bring them to the same calibration of reconstructed jets. Reconstructed jets are matched to truth jets geometrically in $R = 0.3$ cones, where only isolated jets are matched. To calculate the calibration scale, a Gaussian is fit to the energy response $R = E_{reco}/E_{truth}$ in bins of (E_T^{true}, η_{det}), where η_{det} is the η position in the detector, rather than the η of the jet, so it is consistent across all jets. The response is now a function of p_T^{truth}, and must go through the process of numerical inversion to obtain the response as a function of p_T^{reco}. For every p_T^{truth} point, the corresponding p_T^{reco} can be calculated by $p_T^{reco} = p_T^{truth} \times R$, shifting each response value down to the reconstructed momentum. Therefore, response $1/R$ is applied to reconstructed jets as a function of E_{reco} as a correction. Some bias is still seen in the forward region, so a separate η calibration is derived. $\eta^{reco} - \eta^{truth}$ is parameterized as a function of E^{truth} and η_{det}, where the same numerical inversion technique is applied to get this correction as a function of E_{reco}. The jet is then said to be at the EM+JES calibration.

3.1.4 GSC

The initial particle, either quark or gluon, results in a different energy distribution and width of the jet. Quarks tend to produce jets with fewer and harder hadrons, while gluons will have softer hadrons, creating a wider jet which travels a shorter distance in the calorimeter. The calorimeter response and therefore jet reconstruction are shown to still depend on these quantities of the jet, so a further calibration is done to smooth out these dependencies while still maintaining the overall jet energy. This calibration is called the Global Sequential Calibration (GSC) [82][75]. The quantities used in this correction are the fraction of jet energy measured in the first layer of the hadronic calorimeter f_{Tile0}, the fraction of jet energy measured in the final layer of the EM calorimeter f_{LAr3}, the number of tracks associated to the jet with $p_T > 1$ GeV n_{trk}, the p_T weighted transverse distance between jet axis and tracks with $p_T > 1$ GeV W_{trk}, and finally the number of muon segment hits associated with the jet $n_{segments}$. It can be seen that all of these variables have to do with measuring width and depth of the jet, as well as number of hard hadrons, all which highlight the differences between gluon and quark jets. These corrections are once again applied by measuring the response as a function of each variable in bins of (p_T^{truth}, η_{det}) and applying the inverted response to the reco jet 4-momentum, in a similar method to the MC JES corrections. An example response is shown in Figure 3.4. These are applied iteratively, applying the correction of a variable before deriving the response for the next.

Punch through correction

The energy of the jet must also account for such high energy particles that they "punch through" the calorimeter and into the muon spectrometer. Here, the number of muon segments behind the jet are matched to the jet through geometric matching. The energy of the jet is then corrected by applying the jet response (p_T^{reco}/p_T^{truth}) as a function of the number

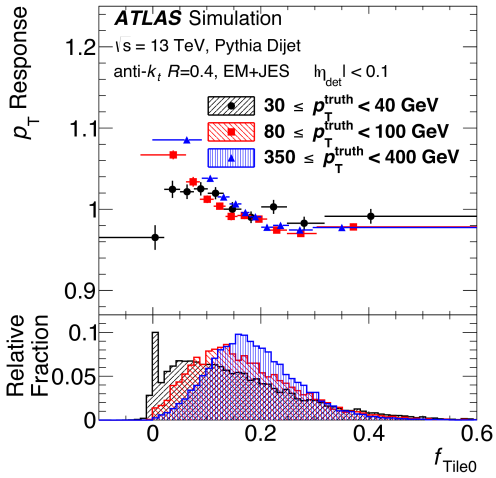

Figure 3.4: One variable used in the global sequential calibration. Jet momentum response as a function of the fraction of jet energy deposited in the first layer of the tile calorimeter. The calibration constant applied to jet momentum is then the inverse of the p_T response for each p_T^{truth} and $|\eta_{det}|$ bin [80].

of muon segments hit.

3.1.5 In-situ technique

The final stage of calibration is used to correct for data and MC differences [75]. MC can never be written to exactly mirror the chaotic collisions and imperfections of the detector, so a method is devised to account for these discrepancies. This is done by balancing a well measured object with a jet, and comparing the ratio of reference object and jet p_T in both data and MC, using this double ratio in Eq. 3.2 as the response. The correction is once again derived as a function of p_T and η. The full momentum range is divided up into 3 reference objects - a Z boson for low p_T jets, photon for mid p_T jets, and multijets for high p_T jets. There is also a single particle response calculated for the very highest p_T range, above 2 TeV. These uncertainties are combined *in-situ* to provide a smooth response across

p_T. A similar response is calculated to smooth out deviations in η, where a well measured central jet is the reference object and is compared to a forward probed jet. The propagation of uncertainties from the reference object to the probed jet also provides a total uncertainty on the jet energy scale measurement.

$$\frac{p_T^{reco,ref}/p_T^{reco,jet}}{p_T^{MC,ref}/p_T^{M,jet}} \tag{3.2}$$

η-intercalibration

This calibration corrects for the differences in detector resolution in the central ($\eta < 0.8$) and forward region ($0.8 < |\eta| < 4.5$) [83]. Dijet events that are back to back in ϕ are chosen, with the reference jet being central and the probe jet being in the forward region. This method is called the central reference method. To better use all data available and increase statistical precision, a second method can be used, called the matrix method. Here, many reference regions are compared to the forward region, and the response for each is calculated. Instead of a probe and reference jet, there is instead a right and left jet defined by $\eta^{left} < \eta^{right}$. The response relative to the central region is then determined by a set of linear equations for each jet η and p_T^{avg} bin. This means any dijet event, rather than those with one central and one forward jet, can be used. Although both method provide similar results, the matrix method is used for final response estimates while the central reference method is used for validation. Any difference in jet p_T across η is attributed to the varying calorimeter response. To quantize this difference in p_T , the asymmetry given by $A = \frac{p_T^{probe} - p_T^{ref}}{p_T^{avg}}$ is used, where p_T^{avg} is the average of the reference and probe jet p_T. Similarly to what is done in the EM+JES calibration, this asymmetry quantity is fit with a Gaussian in bins of p_T^{avg}. This then leads to an estimation of the average response being $\langle \frac{p_T^{probe}}{p_T^{ref}} \rangle \approx \frac{2+\langle A \rangle}{2-\langle A \rangle}$ where $\langle A \rangle$ is the mean of the Gaussian fit. This response in data is then divided by the equivalent response in MC to find a calibration constant. The η-intercalibration is applied before any further *in-situ*

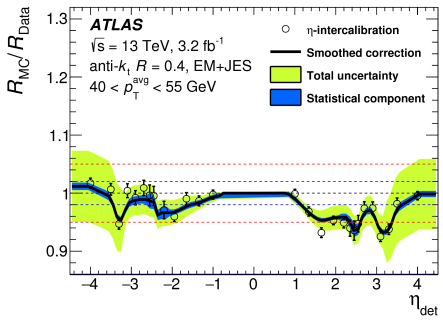

Figure 3.5: η-intercalibration correction as a function of η_{det} [80].

calibrations.

The η-intercalibration comes with several uncertainties. The MC modeling uncertainty comes from the difference in smoothed response of two generators, Pythia+Powheg and Sherpa. The systematic uncertainties come from changes in selections, such as varying the $\Delta\phi$ separation of the two jets and requiring a veto on third jets, and then recalculating the response. There is also a statistical uncertainty and finally a non-closure uncertainty, which comes from an observed non-closure in the range $2 < |\eta_{det}| < 2.6$ and estimated as the difference between data and nominal MC generator after applying the η-intercalibration correction to data. The response with total uncertainties can be seen in Figure 3.5.

Z+jet

The lowest p_T jet range of the *in-situ* calibration is covered by Z+jet balance [84]. Events with a Z boson decaying leptonically back to back with a jet are used to calibrate jets up to 500 GeV. Leptonically decaying Z bosons are excellent calibration objects, as the combination of tracking information for electrons and muons and the small contained showers of electrons results in much more precisely measured objects than jets, and therefore have relatively small

uncertainties. The balance between jet and Z boson is determined through the Missing E_T Projection Fraction (MPF), where the total hadronic recoil is used to balance the Z boson. The response uses the missing transverse energy from all topoclusters along the direction of the Z and compares it to the Z momentum $R_{MPF} = \langle 1 + \frac{\hat{n}_{ref} \cdot \vec{E}_T^{miss}}{p_T^{ref}} \rangle$. Since MPF uses the full hadronic recoil instead of a reconstructed jet, its not sensitive to characteristics of the jet, such as radius and out-of-cone radiation. Once again the response is plotted in bins of p_T^{ref}, but is fit with a modified Poisson distribution that extends to non-integer values, and the mean of the Poisson is taken as the average response. To get a response as a function of p_T^{jet}, the average jet p_T in each p_T^{ref} bin is used. This response is computed for both data and MC, with the ratio of the two taken as a calibration factor.

The uncertainties from this analysis are broken down to MC uncertainty, statistical uncertainty, topological selections, and uncertainty on lepton measurements. The MC uncertainty is done the same as for η-intercalibration, where two MC generators are used, and the difference in response between the two is used as an uncertainty. The topological selections include varying the second jet p_T and $\Delta\phi$ selection, and well as the JVT cut. Finally, uncertainties on electron energy scale and resolution, as well as muon momentum scale and resolution are taken from independent studies of $Z \to ee$ and $Z \to \mu\mu$ events. The $\pm 1\sigma$ uncertainties are propagated through to the calibration ratio. A final out of cone uncertainty is calculated via the direct balance method, which is described in Section 3.1.5. Although MPF doesn't use a jet definition, the uncertainty on the estimate of jet radiation not included in the jet cone is still applied as an estimate for the reconstructed jet topology.

γ+jet

For a higher range of jet p_T, a photon is used in place of a Z boson, and covers the range of $50 < p_T < 950$ GeV [84]. The overlap in p_T range with the Z + jet analysis is combined and smoothed out in the final stage of the *in-situ* analysis (section 3.1.5). The concept behind

this balance is the same at the Z+jet, however the response is calculated differently. Here, the Direct Balance (DB) method is used. Rather than using the full hadronic shower, DB uses a more conventional approach, by taking the jet calibrated up to η-intercalibration and balancing the photon momentum along the direction of the jet $p_T^{ref} = p_T^{\gamma} \times cos(\Delta\phi_{jet,\gamma})$. The response is then taken to be the usual p_T^{jet}/p_T^{ref}. In the same manner as Z+jet, the response is calculated in bins of p_T^{ref} and a Poisson distribution is fit to this distribution, with the mean of the Poisson distribution taken as the response for the average p_T^{jet} within that p_T^{ref} bin. The statistical, MC, out-of-cone, and topological uncertainties are calculated the same as in Z+jet. The γ+jet analysis however does not have to take into account electron and muon uncertainties, but does need to included photon uncertainties. This comes in the form of a purity uncertainty, accounting for jets misidentified as photons, which is derived from relaxing photon identification criteria.

Multijet balance

To calibrate high p_T jets, the jet is balanced off a collection of lower p_T jets, as there is no single particle balance available [83]. These lower p_T jets are already fully calibrated, meaning the corrections due to η-intercalibration and V+jets (Z and γ+jets) is already applied. The highest p_T jet is taken as the single jet, and the 4-vectors of all other jets are combined into a single recoil object. These events must have all jets besides the leading with p_T below the calibrated range of 950 GeV. The response is then $\langle \frac{p_T^{leading}}{p_T^{recoil}} \rangle$. MJB covers the momentum range of $300 < p_T < 2000$ GeV. The distribution is initially binned in p_T^{recoil}, then as with the V+jet analyses is rebinned it terms of $p_T^{leading}$ after taking the mean $p_T^{leading}$ in each p_T^{recoil} bin.

The MC uncertainty is similar to V+jets, but the comparison is with the nominal Pythia generator and Herwig++. There are several event selections that produce an uncertainty. The first being an asymmetry requirement on the subleading and recoil system's p_T, so that

the subleading jet doesn't account for more than 80% of the total recoil p_T, removing dijet events. The azimuthal angle between leading jet and recoil system (α^{MJB}) must also be close to back to back. Finally, the azimuthal angle between leading jet and the next closest jet with $p_T > 0.25 \times p_T^{leading}$ (β^{MJB}) must be also be sufficiently large, as to not contaminate the leading jet. These selections are varied to give a 1σ variation. All 1σ uncertainties from the previous calibrations, V+jet and η-intercalibration, are propogated through as uncertainties on the subleading jets. Finally, EM+JES uncertainties related to pile-up, punch-through, flavor composition, and flavor response from the GSC are also propogated through to the MJB.

in-situ Combination

The final step of the *in-situ* calibration is combining Z+jets, γ+jet, and multijet balance into one smooth calibration across jet p_T [85]. First, a fine p_T binning is introduced, and each *in-situ* method is interpolated using second order polynomial splines. Next, the calibration factor in each large p_T bin is determined from the weighted average of the interpolated contributions from the various methods. Weights are obtained by a χ^2 minimization of the response ratios and their uncertainties in each small p_T bin, and is therefore inversely proportional to the square of the uncertainties. These weights therefore favor the most precise measurement in each bin. To reduce statistical fluctuations, a sliding Gaussian kernel is used to smooth the distribution. Finally, to account for any tension between *in-situ* methods in a bin, if $\sqrt{\chi^2/DoF} > 1$ then each uncertainty is scaled by $\sqrt{\chi^2/DoF}$. The inverse of the final calibration factor is then applied to data to complete the calibration.

Each uncertainty for a given *in-situ* method are treated as fully correlated across p_T and η bins, but uncertainties between different *in-situ* methods are treated as independent. Each uncertainty in each method is shifted by 1σ, and the interpolation and combination are then repeated. The difference between the calibration factor when the uncertainty is shifted

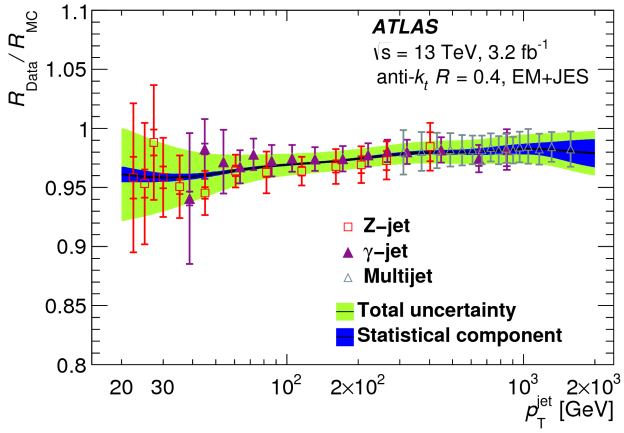

Figure 3.6: Total JES *in-situ* calibration factor and uncertainty. Error bars show combined systematic uncertainties and statistical uncertainties on each measurement, with the combined total and statistical uncertainties shown in green and blue bands, respectively [80].

compared to the nominal is then taken as the 1σ variation for that uncertainty. The χ^2/DoF smoothing procedure is also applied to the uncertainties. The calibration as a function of p_T with uncertainties is shown in Figure 3.6.

E/p

To reach the highest ranges of jet p_T, beyond 2 TeV, yet another method must be used [86][87][88]. This method looks at responses of single hadrons and compares the energy of the hadron measured in the calorimeter to the track p_T measured in the ID. E/p measurements capitalize on the fine momentum resolution of the ID to determine the calorimeter response. To reduce contamination of other hadrons, only isolated tracks are used. A cone starting from the extrapolated entrance point to the EM calorimeter from the exit point in the ID and extending out to the hadronic calorimeter is used to encapsulate the energy of the hadron. Topological clusters calculated at the EM scale that fall within this cone are summed to provide a final energy estimate. A cone size of 0.2 is used to minimize shower and background

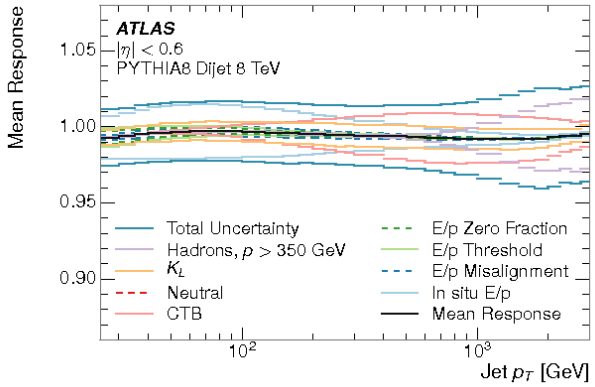

Figure 3.7: E/p response and uncertainties as a function of p_T for $\eta < 0.6$. As this hasn't been repeated for 13 TeV data, this result is shown for 8 TeV [88].

contamination. The final mean estimation of E/p is corrected for background contamination and compared to MC for various bins of η and p_T, as shown in Figure 3.7.

To calculate an uncertainty, simulated dijet events are selected with good separation, and the jet is decomposed into its individual hadrons. The E/p uncertainties for each hadron are then combined to give an estimate of the JES uncertainty. To calculate this uncertainty numerically, a set of MC pseudo-experiments are used. For each pseudo-experiment, the energy response of one hadron is shifted randomly within its E/p uncertainty, and the JES is recalculated. The final JES uncertainty is then the width of the resolution distribution of all the pseudo-experiments. The summed energy measurements of individual hadrons with uncertainty is then compared to the energy of the jet. The uncertainties from E/p measurements are propogated through to the final JES response.

3.1.6 Systematic uncertainties

A final set of 88 uncertainty terms come out of the combination, with groupings of these uncertainties shown in Table 3.1, with a break down of uncertainties as a function of p_T and η shown in Figure 3.8. 88 uncertainties are too many for each analysis to evaluate and implement separately, and reduced sets of nuisance parameters (NP) are provided as a final recommendation. To determine these sets, the correlation between all uncertainties is evaluated using Pearsons correlation coefficient (Eq. 3.3). The full correlation matrix is shown in Figure 3.9. It can be seen that there are regions of higher correlation, corresponding to the various ranges of the *in-situ* analyses. The first step to this reduction of NPs is an eigen-decomposition [85] on the 75 *in-situ* uncertainties, where the seven most dominant eigenvectors are kept, and the remaining are summed in quadrature, reducing to only 8 NPs. There are still 13 untouched uncertainties - 9 listed in the baseline 88, and 4 more from flavor composition, flavor response, b-jets, and punch through jets. A second iteration proceeds to reduce these remaining 13 NPs with the initially reduced 8 NPs to sets of 3 strongly correlated NPs [89], where once again weakly correlated NPs are quadratically combined into one NP. An additional NP was added for η-intercalibration nonclosure, making it a group of 4 strongly reduced NP. This results in four possible sets of reduced NP with 4 NP in each. All four sets of reduced NP were tested in the dijet analysis and gave similar results, so the ATLAS recommended first reduced set of NP was used for this analysis.

$$C(p_T, \eta_1, p_T, \eta_2) = \frac{Cov(p_T, \eta_1, p_T, \eta_2)}{\sqrt{Cov(p_T, \eta_1, p_T, \eta_1) \times Cov(p_T, \eta_1, p_T, \eta_2)}} \tag{3.3}$$

3.1.7 JER

Jet energy resolution (JER) is the measure of how precise jet energy is calibrated. JER is parameterized by Eq. 3.4, where N parameterizes pileup and electronic noise, S parameterizes

Name	Description
Z+jet	
Electron scale	Uncertainty in the electron energy scale
Electron resolution	Uncertainty in the electron energy resolution
Muon scale	Uncertainty in muon momentum scale
Muon resolution (ID)	Uncertainty in muon momentum resolution in the ID
Muon resolution (MS)	Uncertainty in muon momentum resolution in the MS
MC generator	Difference between MC event generators
JVT	Jet vertex tagger uncertainty
$\Delta\phi$	Variation of $\Delta\phi$ between the jet and Z boson
2nd jet veto	Radiation suppression through second-jet veto
Out-of-cone	Contribution of particles outside the jet cone
Statistical	Statistical uncertainty over 14 regions of jet p_T
γ+jet	
Photon scale	Uncertainty in the photon energy scale
Photon resolution	Uncertainty in the photon energy resolution
MC generator	Difference beween MC event generators
JVT	Jet vertex tagger uncertainty
$\Delta\phi$	Variation of $\Delta\phi$ between the jet and photon
2nd jet veto	Radiation suppression through second-jet veto
Out-of-cone	Contribution of particles outside the jet cone
Photon purity	Purity of the sample in γ+jet balance
Statistical	Statistical uncertainty over 15 regions of jet p_T
Multijet balance	
α^{MJB} selection	Angle between leading jet and recoil system
β^{MJB} selection	Angle between leading jet and closest subleading jet
MC generator	Difference between MC event generators
$p_T^{asymmetry}$ selection	Second jet's p_T contribution to the recoil system
Jet p_T threshold	Jet p_T threshold
Statistical components	Statistical uncertainty over 16 regions of $p_T^{leading}$
η-intercalibration	
Physics mismodeling	Envelope of the MC, pile-up, and event topology variations
Non-closure	Non-closure of the method in the $2.0 < \lvert\eta_{det}\rvert < 2.6$ region
Statistical component	Statistical uncertainty over 25 regions of $p_T^{leading}$
Pile-up	
μ offset	Uncertainty of the μ modeling in the MC simulation
N_{PV} offset	Uncertainty of the N_{PV} modeling in the MC simulation
ρ topology	Uncertainty of the per-event p_T density modeling in the MC simulation
p_T dependence	Uncertainty in the residual p_T dependence
Jet flavor	
Flavor composition	Uncertainty in the jet composition between quarks and gluons
Flavor response	Uncertainty in the jet response of gluon-initiated jets
b-jet	Uncertainty in the jet response of b-quark-initiated jets
Punch-through	Uncertainty in GSC punch-through correction
AFII non-closure	Difference in the absolute JES calibration using AFII
Single-particle response	High-p_T jet uncertainty from single-particle and test-beam measurements

Table 3.1: Descriptions of uncertainties included in the final jet energy scale uncertainty measurements.

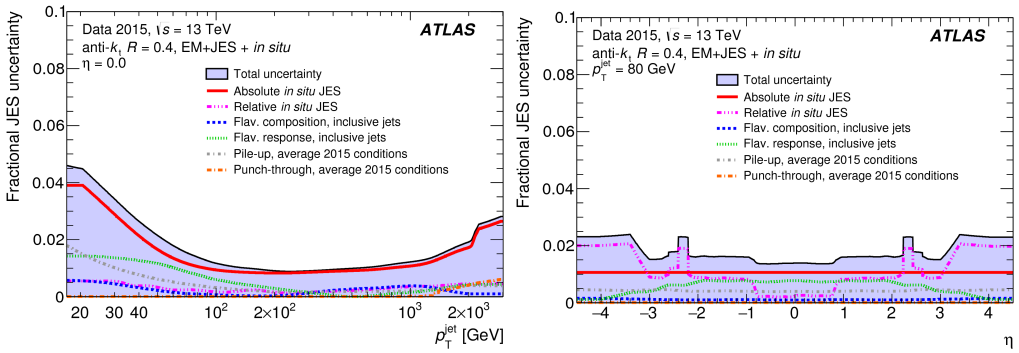

Figure 3.8: Total jet energy scale uncertainties across jet p_T and η [80].

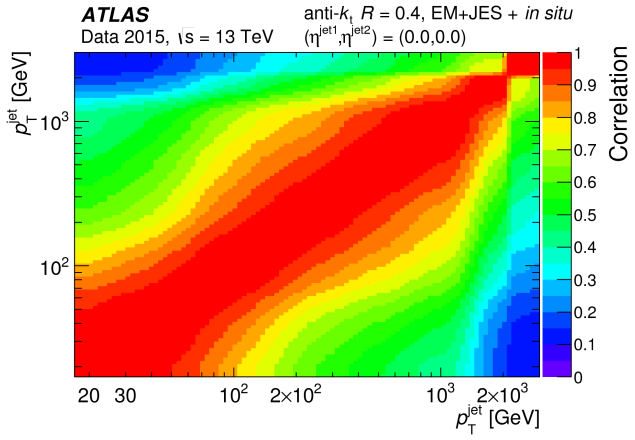

Figure 3.9: Correlation matrix between JES uncertainties over jet p_T [80].

the stochastic effect from sampling of the calorimeters, and C is a constant. JER is similar to JES measurement in that the resolution is determined from several *in-situ* analyses to cover the entire range of jet p_T. At the low to mid p_T range, Z+jet and γ+jet analyses are used as before. In the high p_T region, a dijet balance is used. The resolution for Z+jet and γ+jet is taken as the variance of the fitted Gaussians on the distributions of response. The JER is then computed as a function of p_T and η, and Eq. 3.4 is fit to these results.

$$\frac{\sigma(p_T)}{p_T} = \frac{N}{p_T} \oplus \frac{S}{\sqrt{p_T}} \oplus C \tag{3.4}$$

For JER computed from dijet events, there are two methods. The first is the Dijet Balance method, where back to back dijet events are selected, and the asymmetry (Eq. 3.5) in the transverse momentum of the two jets is computed [90]. A Gaussian is then fit to the asymmetry distribution, and the p_T resolution is taken as σ_A of the Gaussian, resulting in a relationship between σ_A and the relative jet resolution as given in Eq. 3.6.

$$A = \frac{p_{T,1} - p_{T,2}}{p_{T,1} + p_{T,2}} \tag{3.5}$$

$$\sigma_A = \frac{\sqrt{(\sigma(p_{T,1}))^2 + (\sigma(p_{T,2}))^2}}{\langle p_{T,1} + p_{T,2} \rangle} \simeq \frac{\sigma_{p_T}}{\sqrt{2} p_T} \tag{3.6}$$

The second method is called the Bisector Technique, and is what's currently used [90]. Once again dijet events are selected, however their imbalance is now characterized by the vector $\vec{P}_T$, which is the sum of the momentum vectors of the dijet event. This vector is then projected onto a traverse plane (ψ, η), where η is perpendicular to $\Delta\phi$ of the two jets. The assumption taken here is that the resolution in both the ψ and η direction at truth level are equivalent, and any discrepancy is taken as an uncertainty. This leads to the jet resolution as being defined as Eq 3.7, where the variation σ_ψ and σ_η are taken from Gaussian fits to $P_{T,\psi}$

and $P_{T,\eta}$. Once again, these are produced in bins of p_T and fit with Eq 3.4 to get constraints on the fit parameters.

$$\frac{\sigma(p_T)}{p_T} = \frac{\sqrt{(\sigma_{\psi}^{calo})^2 - (\sigma_{\eta}^{calo})^2}}{\sqrt{2}p_T\sqrt{\langle cos\Delta\phi_{12}\rangle}} \tag{3.7}$$

The noise term is determined outside of the *in-situ* methods, as it dominates in the low p_T region, below the reach of *in-situ* analyses. This noise term is then kept constant in the various *in-situ* fits. The first method for estimating N is the zero cone method. A random cone selection on minimum bias samples is performed, where a random cone in $\eta - \phi$ is chosen and the energy within that cone is assigned to be the sum of all energy clusters within [76]. Another cone opposite in ϕ and within the same η slice is similarly determined. The difference in energy of the two cones is assumed to be noise, and is therefore measured as a function of η. For each η bin, the width of the distribution is taken as the 68% confidence interval of a Poisson fit.

A second method of predicting the noise term is also performed. The Soft Jet Momenta method uses the jet energy density ρ as defined in Section 3.1.3. The distribution of $r = (p_T - \rho A)/\sqrt{A}$ is then expected to be Poisson in nature. The 68% CI is once again computed for this distribution to give a final estimate of $\sigma = \sigma_\rho\sqrt{A}$. The difference in estimation of N between these two methods is taken as a systematic uncertainty, as well as the degree of non-closure.

To get a better handle on noise from electronics and threshold effects, MC resolution at $\mu = 0$ is fit with the parameterization Eq. 3.4. The total noise term is then quoted as the quadratic summation of the noise term due to pile up (zero cone method) and the noise term in a no pile up sample (MC).

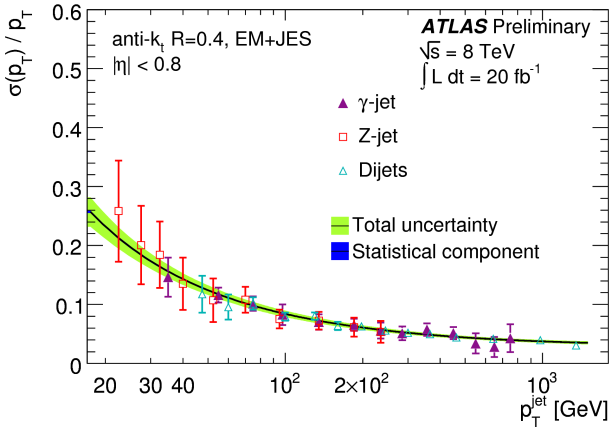

Figure 3.10: JER correction and uncertainty as a function of p_T for $\eta < 0.8$. The total uncertaintyon the combined results is shown in green, and the statistical uncertainty shown in blue. As this hasn't been repeated for 13 TeV data, this result is shown for 8 TeV [76].

3.1.8 Jet Cleaning

By the recommendation of the JetEtMiss group [91], if any jet in the event is considered "bad", the entire event should be rejected. There are two versions of jet cleaning, "tight" and "loose". Tight cleaning has more stringent selections and is used for analysis that are sensitive to more non-collision backgrounds, and so as recommended the loose cleaning was applied here. The selections used to determine a bad jet are there to protect against sporadic noise, hardware issues, cosmic muon showers, and beam induced backgrounds. The quantities used are described here:

- f_{HEC} (f_{EM}): Fraction of jet energy deposited in the HEC (EM) calorimeter. Very high or very low values are indicative of bad jets
- f_{max}: the fraction of jet energy deposited in the calorimeter layer with the maximum energy fraction. Very high values point to a hardware malfunction.
- $\langle Q \rangle$: the average of the quadratic difference between observed and expected LAr cell

pulse (Q_{cell}^{LAr}) over the entire jet. High values correspond to electronic or pileup noise.

- $f_Q^{HEC}(f_Q^{LAr})$: Fraction of energy in HEC (LAr) calorimeter cells of a jet with $Q_{cell}^{LAr} > 4000$.

- E_{neg}: Sum of energy in cells with negative energy. Noisy cells can sporadically deposit large amounts of negative energy.

A jet is considered BadLoose if any of the following are true:

- $f_{HEC} > 0.5$ and $|f_Q^{HEC}| > 0.5$ and $\langle Q \rangle > 0.8$.
- $|E_{neg}| > 60$ GeV
- $f_{EM} > 0.95$ and $f_Q^{LAr} > 0.8$ and $\langle Q \rangle > 0.8$ and $|\eta| < 2.8$
- $f_{max} > 0.99$ and $|\eta| < 2$
- $f_{EM} < 0.05$ and $f_{ch} < 0.05$ and $|\eta| < 2$
- $f_{EM} < 0.05$ and $|\eta| \geq 2$

3.1.9 Trigger

The trigger used in this analysis is the lowest unprescaled single jet trigger. This is the HLT_j380 trigger, as detailed in Section 2.3. Turn on curves show the trigger efficiency, or number of events that pass selection divided by the number of events without the selection, as a function of jet p_T, and depends on the resolution of p_T/E_T. Trigger turn on curves are made to determine at what jet p_T and therefore what m_{jj} the trigger becomes at least 99.5% efficient. As shown in Figure 3.11, this is a jet p_T of 420 GeV and an m_{jj} selection of 1100 GeV, where these are applied as analysis selections.

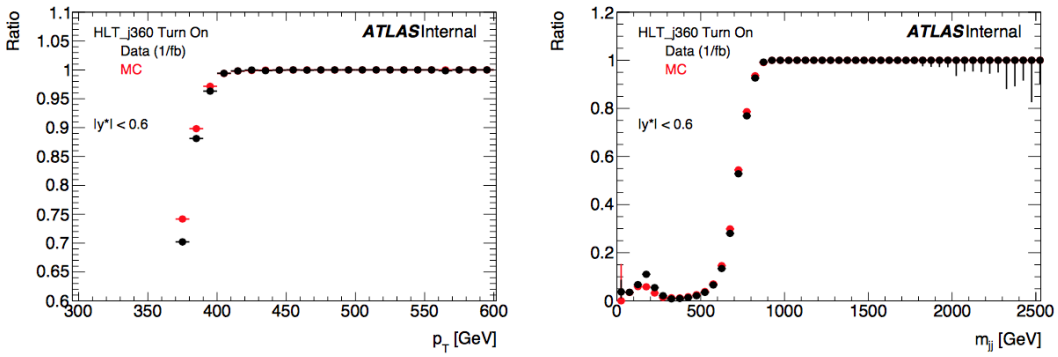

Figure 3.11: Trigger turn on cruves for HLT_j360 for p_T and m_{jj}. The efficiency shown in defined as the number of jets passing the trigger over the number of jets in that p_T bin [92].

Chapter 4

Resonant Dijet Analysis

4.1 Introduction

The resonant dijet analysis looks for a localized excess in the dijet mass spectrum as a sign of new particle production. The background is dominated by QCD scattering events, which produce a smoothly falling distribution over mass. The event selection to optimize signal production is given below.

4.2 Event selection

- Good Run List (GRL)
- LAr: LAr error rejected
- Tile: Tile error rejected
- SCT: SCT single events rejected

- Core: Incomplete event build rejected
- Primary Vertex: PV has at least two tracks associated with it
- all jets have $p_T > 60$ GeV and pass cleaning cuts [91]
- Trigger is HLT_j380
- Leading jet $p_T > 440$ GeV
- $m_{jj} > 1100$ GeV
- $|y^*| < 0.6$
- W^*: $|y^*| < 1.2$, $m_{jj} > 1717$ GeV

The first several selections are cleaning criteria based on ATLAS recommendations. The trigger selection and the leading jet and m_{jj} selections are detailed in Section 3.1.9. The $|y^*|$ selection results from the fact that background QCD events are mainly t-channel scattering, which tend to be in the forward region, while new physics is s-channel scattering, which tends to be more central. QCD production is proportional to $(1 - \cos\theta^*)^{-2}$ while q^* production is flat in $\cos\theta^*$, where θ^* is the polar scattering angle in the COM frame [93]. Based on this, the q^* signal is used to optimize the $|y^*|$ cut by looking at the signal significance ($S\sqrt{B}$) as a function of $|y^*|$ selections. Finally, the event selections are re-optimized for the W^* signal. This leads to the $|y^*|$ selection increasing to $|y^*| < 1.2$ due to the W^* having an additional $\cos^2\theta$ dependence that reduces production in the central region. This change in $|y^*|$ selection also increases the mass selection, with the trigger becoming fully efficient past $m_{jj} > 1600$ GeV, and the m_{jj} cut used being the next closest bin in the mass distribution.

4.3 Binning

The mass binning must find balance between the detector resolution and signal widths. To prevent any smearing of events across bins, the bins must be wider than the detector mass resolution, given by the standard deviation of $m_{jj}^{reco}/m_{jj}^{truth}$ in bins of m_{jj}^{reco} [94]. To get a smooth resolution R across all m_{jj}, a 6^{th} order polynomial is fit to the binned resolution. The bins must also not be too wide, as signals must be present over multiple bins to be statistically significant. After a series of tests [95], the goal was set to maximize the number of bins, which corresponds to selecting bins as close to detector resolution as possible. An iterative process was done to determine the final binning, and is outlined as follows:

- Taking an initial bin boundary $m_{initial}$, guess the bin center to be $m_{center} = m_{initial} \times R(m_{initial})$
- Calculated the bin width for a bin centered at m_{center} as width $= m_{center} \times R(m_{center})$
- Check if $m_{low} = m_{center} - \frac{1}{2}(m_{center}) \times m_{center}$ is in agreement with $m_{initial}$ - does the upper boundary of bin i and lower boundary of bin $i+1$ agree within 0.1%?
- if $m_{low} > m_{initial}$, shift $m_{initial}$ by -0.01 GeV and go back to step 2
- if $m_{low} < m_{initial}$, shift $m_{initial}$ by 0.01 GeV and go back to step 2
- if $|m_{low} - m_{initial}| < 0.001$, round $m_{upper} = m_{center} + \frac{1}{2}(m_{center}) \times m_{center}$ to the nearest 1 GeV
- Repeat with m_{upper} as the new m_{inital}

Beyond the available MC up to approximately 8 TeV, it appears the dijet mass resolution becomes constant, and so the binning is extended out to 13 TeV based on the width of the last calculable bin. QCD MC was used to validate these studies.

4.4 Background estimation

The dominant and therefore only relevant background to model for the dijet search is QCD events. These events are predominately t-channel scattering events, where the two quarks within each proton exchange a gluon and continue on. As noted by Section 4.2, these events tend to have small scattering angles, resulting in more events in the forward region. Even after the y^* section, there is still a large amount of these events in the search phase. The resulting mass spectrum is a smoothly falling distribution, extending out to very high mass. Due to the complexity of QCD, it has been shown that MC estimates of these events do not perform well enough to use in the analysis. Also, with the increasing luminosity of the LHC, to get the statistical power from MC that is equivalent to data would require an enormous amount of time and space. Therefore, for many iterations this analysis has used a polynomial fitting function to extract a background estimate from data [96][97][98][99][100][101]. The fit function models the general structure of the desired background, and over the years the set of usable functions has grown as more terms are added to achieve a better fit. As data collection has continued, however, the statistical uncertainty on the data grows smaller, meaning even more features previously hidden by error bars start to show. To address this, the current fit function approach would need to add even more terms to fit these details, growing even more complex. For this reason, an alternative but related approach was used to provide a background estimate.

4.4.1 SWiFt

A Sliding Window Fit (SWiFt) was instead used as a background estimate. SWiFt breaks the mass distribution up into windows, fits a function to the data in that window, and finally pieces together a full background estimate. This allows some flexibility to the polynomial fit functions to better express the features within each window. SWiFt uses a four parameter

fit function Eq. 4.1 in each window, the same dijet fit function used to fit the entire spectrum in the previous iteration of the analysis [94]. The fitting is done using MINUIT minimizer [102], where the negative log Poisson likelihood is minimized. The fit result in the middle bin of the window is used as the background estimate for that bin. The optimal window size was determined to be 30 bins to the left of the bin and 20 bins to the right. For the low mass end, bins without 30 bins to the left are filled in with an extended background estimate from the the last window that does allow the full window size. This same method is done in the high mass region, with bins within 20 bins from the right most edge of the mass spectrum being filled in from the last available window. The only deviation from this procedure is for the W^* version of this analysis, in which the window size was re-optimized to instead be 15 bins to the left and 10 bins to the right. Tests for the development of SWiFt are found in [92].

$$f(x) = \theta_1(1-x)^{\theta_2}x^{\theta_3+\theta_4 lnx} \tag{4.1}$$

4.5 Search Phase

The dijet analysis can be broken down into two parts, the first being a generic search, scanning the mass spectrum for any signs of an excess, and the second setting limits on specific signal models. The first piece, often called the search phase, uses BUMPHUNTER [103] to search for excesses in the data, and simultaneously gives an estimate to how well the background describes the data. Many typically goodness of fits tests are done in this analysis, including a χ^2 and negative log likelihood (NLL) test. These tests do provide insight into how well the background agrees with the data, however both methods fail when looking to quantify discrepancies the dijet analysis would be looking for - mainly several adjacent bins fluctuating up together. Goodness of fits likes χ^2 and NLL only account for differences in

individual bins, not sets of bins. For this, the BumpHunter algorithm was devised.

4.5.1 BumpHunter

The BumpHunter algorithm compares the data to background in varying windows, ranging from two bins wide to half the mass spectrum. In each window, the log likelihood between the summed data across all bins in the window, d, and the summed background estimate, b, are computed. For each window, the Poisson likelihood between these two quantities is calculated as listed in Eq 4.2, where Eq 4.2 can be written in terms of Gamma functions as shown in Eq. 4.3. The final BumpHunter test statistic, describing the agreement of the whole spectrum, is then the log of the smallest likelihood across all windows, $t_0 = -\log t_{min}$. This method is therefore a theory agnostic search for any signal like excess. The window corresponding the t_0 is then considered the most discrepant region.

$$t = \begin{cases} \sum_{n=0}^{d} \frac{b^n}{n!} e^{-b} & \text{for} \quad d < b \\ \sum_{n=d}^{\infty} \frac{b^n}{n!} e^{-b} & \text{for} \quad d \geq d \end{cases} \tag{4.2}$$

$$t = \begin{cases} 1 - \gamma(d+1, b) & \text{for} \quad d < b \\ \gamma(d, b) & \text{for} \quad d \geq d \end{cases} \tag{4.3}$$

The look elsewhere effect is something the plagues all LHC analyses. If an experiment is repeated a large number of times, there is always some probability that statistical fluctuations can cause signal like excesses. If one is not careful when the dealing of this possibility, it can lead to false claims of discovery. BumpHunter combats this with its search across all possible window sizes and locations, as well as its p-value calculation which will be discussed here [104].

Given any test statistic, a p-value can be calculated that quantifies the disagreement between two datasets on a range of 0-1. For hypothesis testing, the p-value states the probability of getting a result at least as extreme as the one seen, given the null hypothesis. This means a value of 0 equates to there being no possibility of getting the result given the null hypothesis is true, and therefore the alternate hypothesis is the better descriptor of the data.

To estimate a p-value using BumpHunter, pseudo data is produced from the background estimate - in each bin, the pseudo data is a draw from a Poisson distribution with expected value equal to the background estimate in that bin. For each pseudo data estimate, the BumpHunter test statistic is calculated between the pseudo data and the original background estimate. This ensemble of test statistics is then compared to the test statistic between data and background estimate (observed test statistic), with the final p-value being the fraction of test statistics which are greater than the observed test statistic. This is based off the frequentist notion of probability, in which if a hypothesis is true, the probability of getting a result is the fraction of true results out of an ensemble of repeated experiments. The distribution of test statistics and the visual representation of the p-value is shown in Figure 4.1. As seen in the figure, the p-value obtained is 0.83. A p-value of less than 0.05 would indicate that there is a 2σ deviation, and therefore evidence that there is significant deviation in data from the background estimate, which is not the case here.

4.5.2 Results

The final fit overlaid with data is shown in Figure 4.2, with the most discrepant window as determined by BumpHunter highlighted with blue vertical lines. The middle panel is the bin by bin significance [105]. Significance is the number of standard deviations of the difference between estimate and observation, assuming Poisson distributed data in a

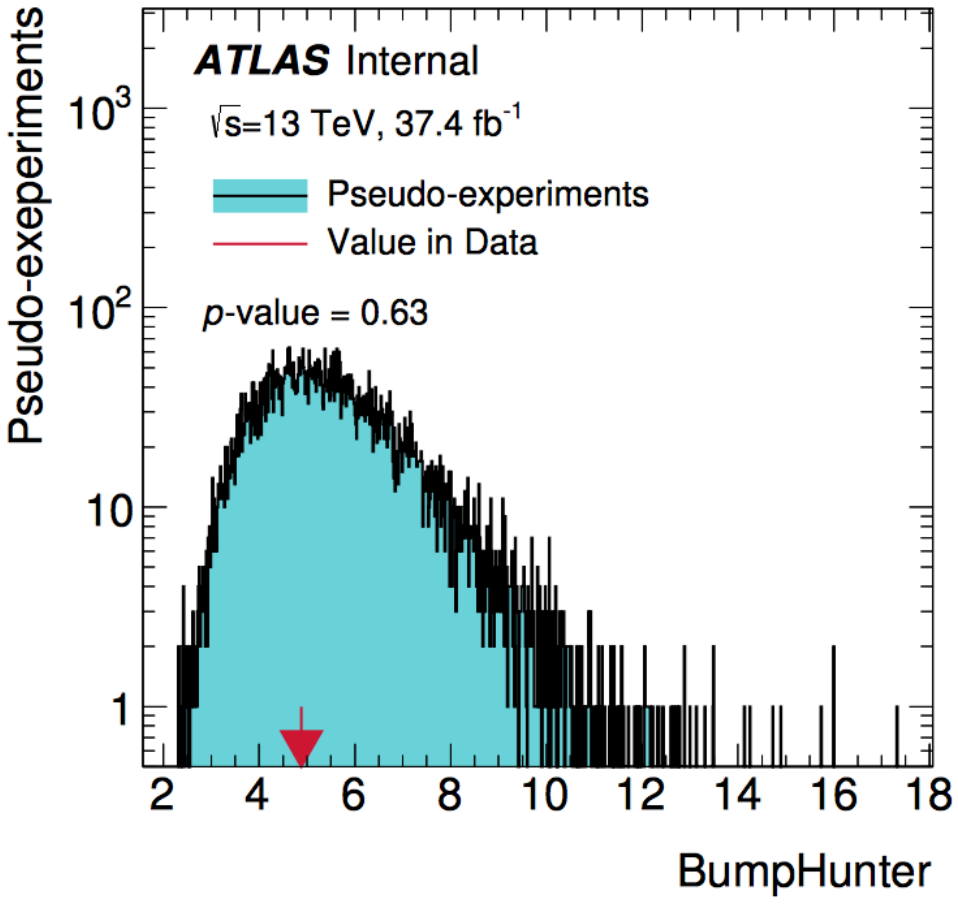

Figure 4.1: Distribution of BumpHunter test statistics from the fit to 10000 pseudo datasets. The Bump Hunter test statistic from the nominal background fit to data is shown as a red arrow. The p-value is then quoted as the fraction of test statistics below the data test statistic [92].

Gaussian approximation. In each bin, the Poisson p-value is calculated (Eq. 4.2). The p-value can be converted to a z-value, or significance, which is the number of standard deviations of a standard Gaussian that would correspond to the same probability given by the p-value, and is given in Eq. 4.4. As defined, values less than 0 correspond to no interest and those at 3σ equate to somewhat significant deviation. When plotting the z-values however, it is more intuitive to assign a sign to the value, with negative values corresponding to the case when expected is above observed, and positive values when observed is greater than expected. Therefore, any z-value less than zero is drawn at zero to state there is no disagreement within the bin, and any z-value above 0 is given a sign based on its observed to expected comparison. Finally, the relative difference between data and QCD MC simulation with JES uncertainty bands is shown in the bottom panel. The MC is not used in any other portion of the analysis, and is simply used for a visual reference.

$$p = \int_{z_{value}}^{\infty} \frac{1}{\sqrt{2\pi}} e^{-\frac{x^2}{2}} dx \tag{4.4}$$

4.6 Background Uncertainties

SWiFt uses the same process of background uncertainty estimate as has been done in previous dijet searches. The background uncertainty is broken down into two pieces, the first being an uncertainty on the fit function parameters, and the second being the choice in fit function.

4.6.1 Fit parameter uncertainty

The fit parameter uncertainty is a measure of how accurate the fit is. This uncertainty would ideally be a confidence interval that is determined by the covariance matrix of the fitted parameters. Using MIGRAD algorithm within MINUIT [102] in the fitting procedure,

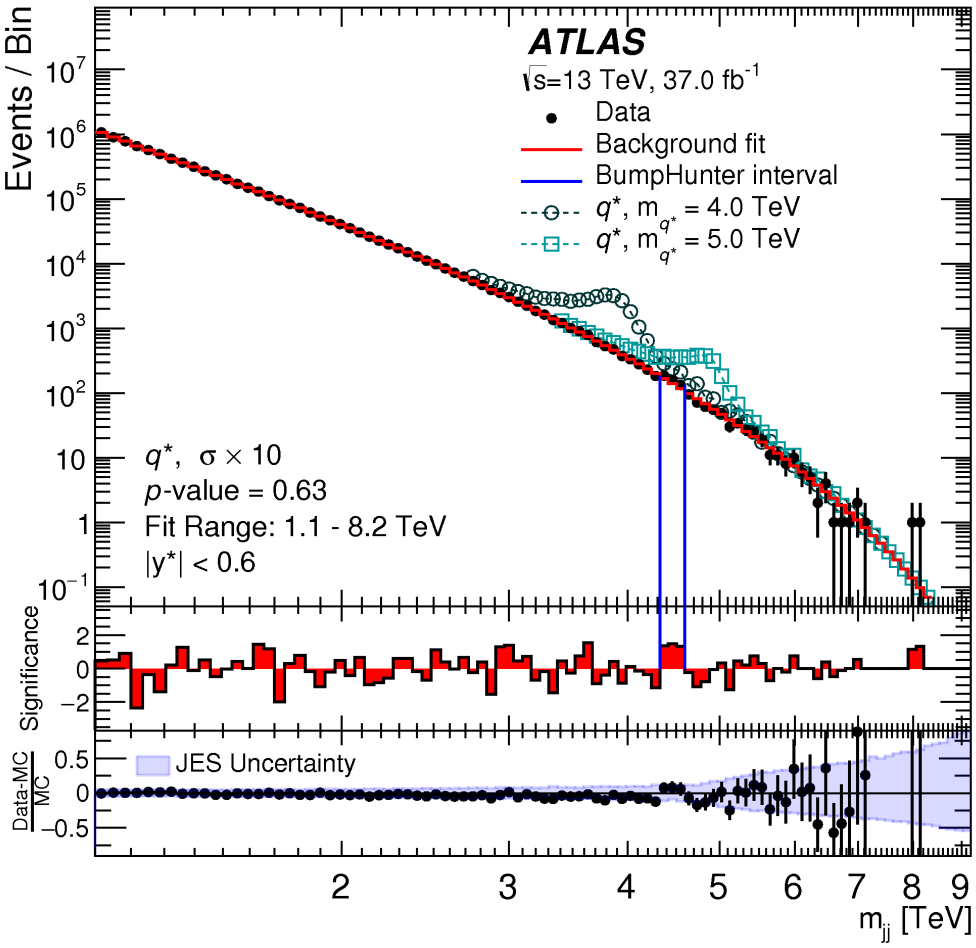

Figure 4.2: The SWiFt background fit to data in red with two q^* signals overlaid. The most discrepant window as determined by BumpHunter is highlighted with blue vertical lines, and gives a p-value of 0.63. The middle panel is the bin by bin significance, and the bottom panel shows the difference between data and MC with JES uncertainty bands, as comparison only [106].

however, the covariance matrix will not be accurately calculated for parameters that are strongly correlated or a poorly behaved log likelihood function. Therefore, an estimate of a 1σ band is calculated via pseudo experiments. 10000 pseudo experiments are generated by adding Poisson noise in each bin of the nominal SWiFt background estimate, similarly to what was done to calculate the BumpHunter p-value in Section 4.5.1. This set of pseudo data is then refit via the SWiFt fitting procedure, starting with the same initial conditions as the fit to data. The error is then quoted as the RMS of the fit values on all pseudo experiments for that bin.

4.6.2 Fit Choice uncertainty

Another uncertainty comes from the fact that the fit function used was a choice, and several other functions could have been used in its place. To provide an estimate on how much the background would differ with another fit function, the SWiFt background fitting procedure is done with a fit function of one degree more than the nominal fit function, in this case the 5 parameter fit function (Eq. 4.5). To get a 1σ uncertainty, a similar procedure to the fit parameter uncertainty is done. Pseudo data thrown from the nominal background fit is then refitted with both the 4 and 5 parameter fit function. The RMS of the difference between the two fits for each pseudo experiment is then taken as the uncertainty in that bin. This uncertainty is kept as a single sided uncertainty, where the difference between the two is always taken in the direction of nominal minus alternate fit. The background uncertainties can be seen in Figure 4.3.

$$f(x) = \theta_1(1-x)^{\theta_2}x^{\theta_3+\theta_4\ln x+\theta_5(\ln x)^2} \tag{4.5}$$

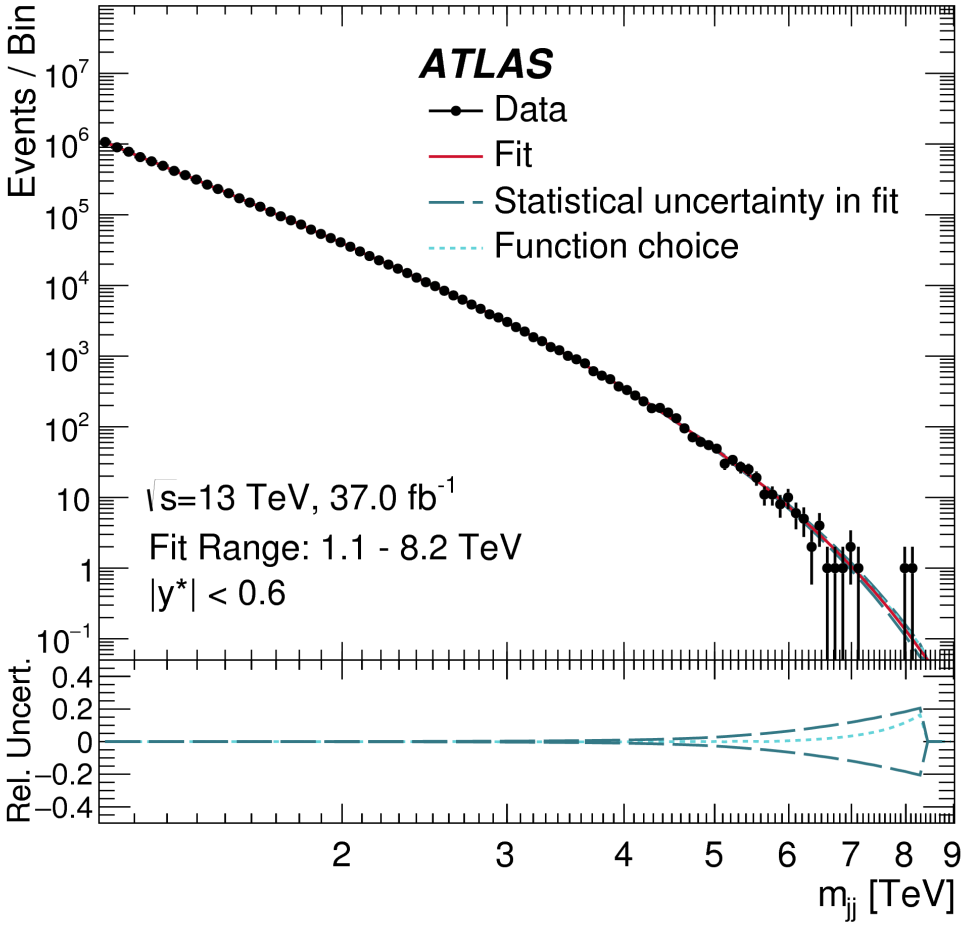

Figure 4.3: Uncertainties on the background fit. The background fit is in red, with the light blue band representing the uncertainty on the fit function choice and the dark blue representing the uncertainty on the fit parameters [92].

4.7 Uncertainties

The fit function choice and fit function parameters are the only two uncertainties on the background, but there are several that effect the signal. All of these uncertainties must be taken into consideration in the limit setting phase.

4.7.1 JES

The strongly reduced set of JES nuisance parameters from Section 3.1.6 are used as uncertainty on the signal templates. As discussed, there was found to be little difference in limit results when each reduced set of NP was used, so the first set was chosen as the final uncertainty.

4.7.2 Luminosity

The procedure for determining luminosity uncertainty is detailed in Ref. [107]. The luminosity can be quantified in terms of several parameters (Eq. 4.6), where f_r is the revolution frequency of the bunches, n_b is the number of bunches, σ_{vis} is the visible cross section, and μ_{vis} is the visible bunch rate per crossing. f_r and n_b are known quantities, but μ_{vis} and σ_{vis} are measured quantities that depend on run conditions and choices in algorithms. σ_{vis} is measured during van der Meer scans [108], the last of which was in 2016, then assumed to be constant for the remainder of the data taking period. μ_{vis} is determined during data-taking via various detectors. The sources of uncertainty on luminosity come from both the calibration of σ_{vis} and μ_{vis}. These include the assumption that these are valid for the entire data-taking period, as well quantities such as pileup and background estimations. Combined,

these given a total uncertainty of 2.1%.

$$L = \frac{f_r n_b \mu_{vis}}{\sigma_{vis}} \tag{4.6}$$

4.7.3 PDF

PDF uncertainties arise from the choice of one PDF set over another. To estimate this uncertainty, the NNPDF set used is compared to two other sets, MSTW and CDF. The differences in PDFs can cause two effects on the signal - the first being a change in acceptance, which would change the normalization of the signal, and second is a change in shape. It has been determined that the shape changing component is not viable to include, and is therefore not ATLAS policy to use it. The shape changing uncertainty is included, and produces only a flat 1% uncertainty.

4.8 Limits

The limit setting procedure is when specific models are tested. Given a new physics model, we seek to understand what the probability of that model existing is given the data available. To do this, normalized histogram templates of the new physics models at evenly spaced mass points are created by MC, as given in Section 2.4.1. An additional parameter, the signal strength ν, is introduced, and is the scale of the normalized histogram. The signal strength is directly related to the maximum number of signal events (N_{signal}) that can fit in the data, producing an upper bound on the cross section (σ) by $N_{signal} = L\sigma$, where L is luminosity. The final limit is then stated as the mass at which the theory predicted cross section intersects the maximum allowed cross section based on the observations. The limits in this analysis are produced and interpreted through a Bayesian framework.

4.8.1 Bayesian Framework

Bayesian probabilities follows Bayes theorem, which states that any probability can be broken down as shown in Eq. 4.7, where $P(B|A)$ is the likelihood, $P(A|B)$ is the posterior, and $P(A)$ is the prior. Priors are the cornerstone of Bayesian statistics, containing some prior belief in the probability distribution of A. To extend this to a more robust explanation, the posterior is the probability that a hypothesis is true, given the data. The likelihood is therefore the probability of getting the data, given the hypothesis, and the prior is some previous believe of what the probability distribution for the hypothesis is. There are several expansions that need to be made to this equation to be accurately implemented in the dijet analysis. First, as all probabilities must be less than 1, $P(B)$ is simply a normalization constant, and can therefore be replaced with Eq. 4.8. Second, there can be many parameters in a hypothesis model, and in general there is only one of interest, while the rest are called nuisance parameters. If the parameters are all independent, there needs to be a prior for each separate parameter. Finally, the posterior will need to be evaluated only on the parameter of interest to get limits on that parameter. This then leads to the final equation used in this analysis Eq. 4.9, where θ are the nuisance parameters, ν is the parameter of interest, and $L(x|\nu,\theta)$ is the likelihood, written as standard notation. The integration over the nuisance parameters is called marginalization [109], so that the final posterior is only with respect the the parameter of interest.

$$P(A|B) = \frac{P(B|A)P(A)}{PB} \tag{4.7}$$

$$P(B) = \int P(B|A')P(A')dA' \tag{4.8}$$

$$p(\nu|x) \sim \int L(x|v,\theta)\pi(\nu)\prod_i \pi(\theta_i)d\theta \tag{4.9}$$

In the case of the dijet analysis, ν is the signal strength parameter, θ are parameters related to the uncertainties, and the likelihood is a Poisson likelihood between the observed data and the background plus signal template. The prior used for the signal strength, $\pi(\nu)$ is set to be a uniform prior given by Eq. 4.10. This means that any signal strength is equally probable, making for easier interpretations. To get a meaningful result, the 95% CL is calculated. In the Bayesian framework, it is interpreted as there is a 95% probability that the true signal strength value lies below the upper limit. The 95% probability is then the posterior integrated over the credibility interval [110], which is from 0 signal strength to the upper limit as seen in Eq. 4.11.

$$\begin{aligned} \pi(\nu) =& 1/\nu_{max} \quad \text{for} \quad x \quad \text{in} \quad [0,\nu_{max}] \\ & 0 \quad \text{else} \end{aligned} \tag{4.10}$$

$$0.95 = \int_0^{\mu_{up}} p(\nu|x)d\nu \tag{4.11}$$

This upper limit is calculated for each mass point that was simulated with MC, and limits are interpolated linearly between mass points. This is also done for expected limits. Expected limits provide insight into what the limits would be given a perfectly null hypothesis, and allow some idea as to how much the observed limits can fluctuate due to statistical uncertainties before being incompatible with the null hypothesis. Expected limits are therefore determined from pseudo data thrown from the nominal background fit, with the signal strength set to 0. 1σ and 2σ bands are then the quantiles of the collection of upper limits from the pseudo data at each mass point.

To machinery used to calculate the limits is called the Bayesian Analysis Toolkit (BAT)

[111]. BAT takes as inputs a likelihood function and priors for all parameters. The likelihood function passed into BAT is a Poisson likelihood (Eq. 4.12), where d_i is the number of data events in bin i, and b_i is the number of background events in bin i. It then uses a Markov Chain Monte Carlo (MCMC) for numerical integration, and for each parameter marginalizes out all others, returning a posterior distribution for each parameter. MCMC works in a way that for each step in parameter space, the new parameter value depends only on the step before it. The particular MCMC algorithm used in BAT is Metropolis [112]. It chooses the next point in parameter space off a jumping algorithm, which is dependent only on the step number and current parameter value. If the new values are an improvement in probability, the new values are accepted. If not, they are rejected with some probability. The MCMC is initiated with 10000 chains, and when the chains all coverage to the same values, the integration finishes.

$$L(\theta|x) = \prod_i \frac{b_i^{d_i} e^{-b_i}}{d_i!} \tag{4.12}$$

4.8.2 Limit background

The SWiFt background for limit setting is slightly different than the nominal background fit. Instead, for each signal template, a background plus signal fit is performed on the data. The background used in the limit setting is then the background only component of this fit. The uncertainties are recalculated as they are done in the search phase.

4.8.3 Uncertainties

The systematic uncertainties are broken down into three categories, which must be applied in order. These are template uncertainties, which are mass dependent changes; shape shifting,

which change the overall shape of the mass spectrum; and scale changing, which change the overall normalization of the distribution.

Template uncertainties are the fit function uncertainties. The fit function choice and fit function parameter uncertainties are recalculated in 0.5σ shifts between -3.5σ and 3.5σ to allow for a linear interpolation of the nuisance parameter between significances. For each uncertainty, the nominal histogram is normalized to one, and the varied histograms are adjusted accordingly. The adjustment for each bin in the nominal histogram is then in terms of the negatively shifted template and positively shifted template. The final uncertainty histogram for the combination of these two uncertainties is the nominal histogram plus adjusted histograms for each uncertainty.

Shape changing systematics are the JES systematics. For this, a set of transfer matrices is determined, where each transfer matrix corresponds to a JES reduced nuisance parameter and a significance. The significances are in steps of every 0.5σ from $[-3.5\sigma, 3.5\sigma]$. These transfer matrices relate events in the nominal histogram to those in the shifted, where each entry $[i, j]$ is the fraction of events in bin i that transfered to bin j. The content in each bin is linearly interpolated, just as the template based systematics. To apply multiple shape changing systematics, the matrices are multiplied together and applied to the initial vector of bin contents.

Scale changing systematics are applied last. Luminosity and PDF uncertainties fall in this category. This is the simplest implementation of uncertainties, as only the percentage uncertainty across the whole spectrum is needed, and represent the 1σ change in θ. Therefore, the combined change on the bin content due to both luminosity and PDF uncertainties is the product of the percent values times the nominal bin content.

Model	**Observed** [TeV]	**Expected** [TeV]
q*	6	5.8
W'	3.6	3.7
W*	3.4	3.6
	3.77 - 3.85	
QBH	8.9	8.9

Table 4.1: Lower limits on mass of four benchmark models at 95% CL. When an additional range is included, as in the W^* model, the masses between those points are also excluded [106].

4.8.4 Results

The limits for each signal model are shown in Figure 4.4. The observed and expected limit on each model are quoted as the crossing point of the theory line with observed and expected limits lines, and are listed in table 4.1. Limits between mass points are interpolated linearly.

The Z' limits are presented differently, as there are two free parameters in the model. The limits are instead shown in a $2D$ grid of mass of the Z' and coupling to quarks shown in Figure 4.5. Each $(m_{Z'}, g_q)$ point is run through the standard limit setting procedure, however the plot now indicates exclusion as the direction of the dashed line, as cross section rises with increased coupling. The limits are interpolated in g_q^2 and then in $m_{Z'}$ to give a smooth limit curve. As this model is a standard for dark matter searches at ATLAS, these limits can be combined with the limits of other analyses, and is shown in Figure 4.6.

4.9 Gaussian Limits

A useful study, particularly for theorists, is to set limits on a generic signal shape. For this analysis, a Gaussian is used for this shape. Five Gaussian signals of various widths are used, from an infinitely narrow ($\sigma/m = 0$) to $\sigma/m = 15\%$. A new procedure is used to evaluate the limits of a Gaussian signal at particle level, separating out detector effects from the signal.

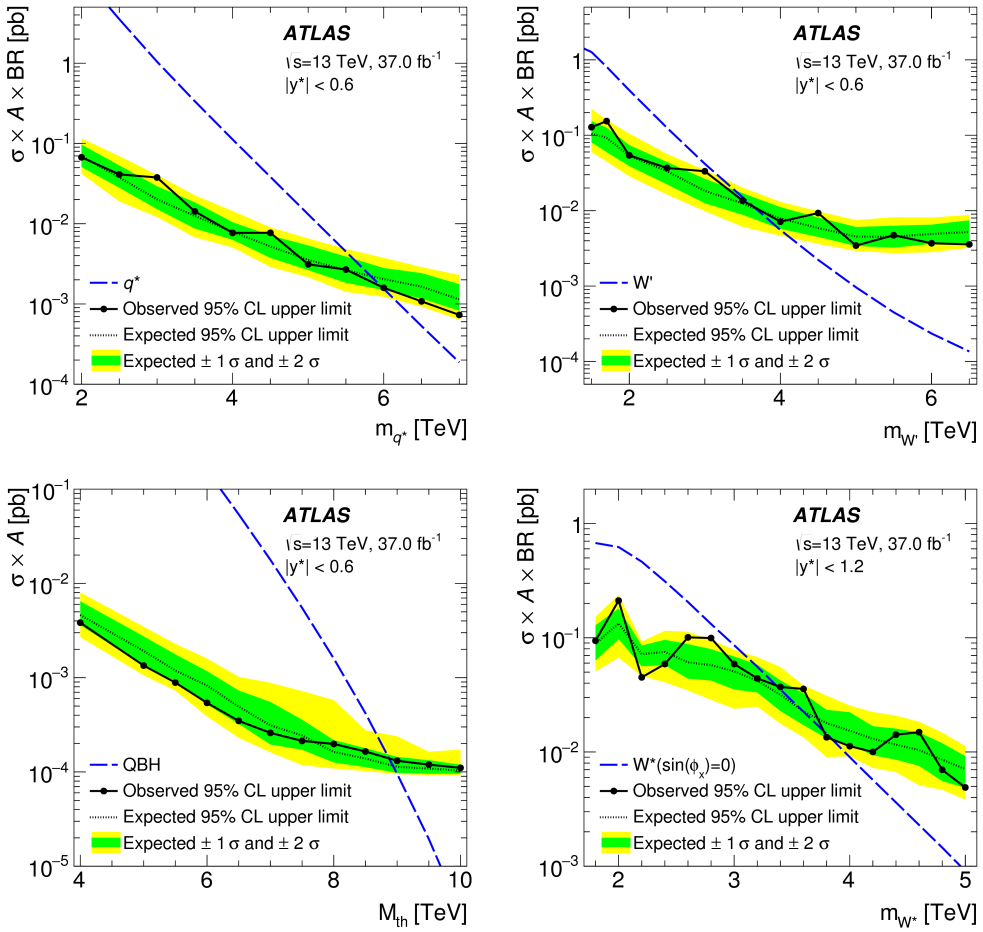

Figure 4.4: The 95% CL upper limits on cross section times acceptance times branching ratio, $\sigma \times A \times B$, on the four benchmark models with the top left q^*, top right W', bottom left quantum black holes, and bottom right W^*. Limits are interpolated linearly between simulated mass points [106].

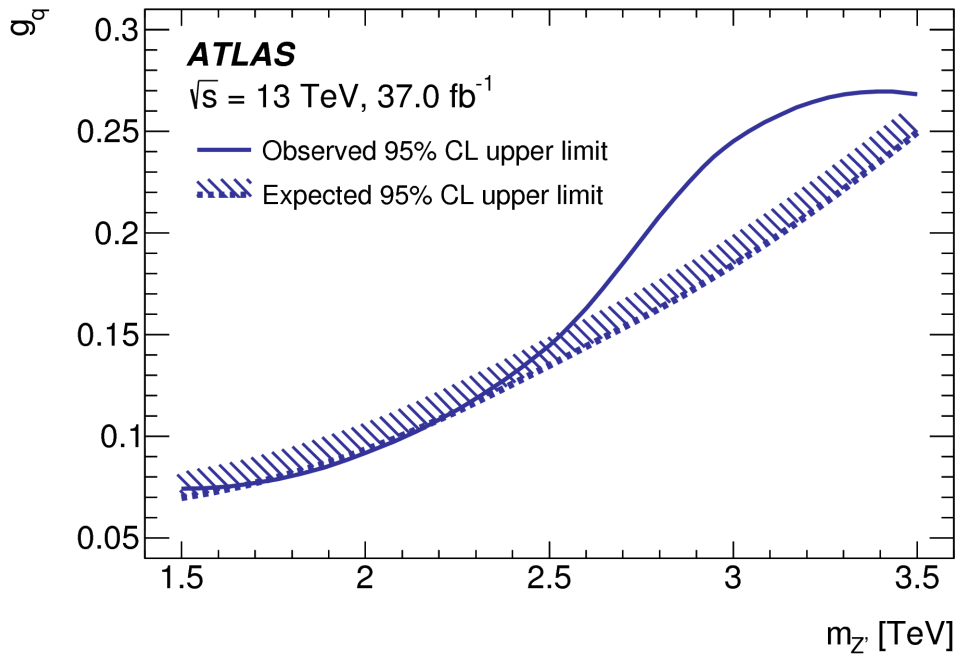

Figure 4.5: 95% CL exclusion limits on Z' mass, $m_{Z'}$, and couplings to quarks, g_q, with mass of the dark matter particle M_{DM} and coupling to dark matter g_{DM} kept fixed at 10 GeV and 1.5, respectively. Cross section increases as g_q increases, resulting in exclusions above the lines being excluded, as indicated by the dashed lines. A smooth curve is drawn between simulated points by interpolated in g_q^2 then $m_{Z'}$ [106].

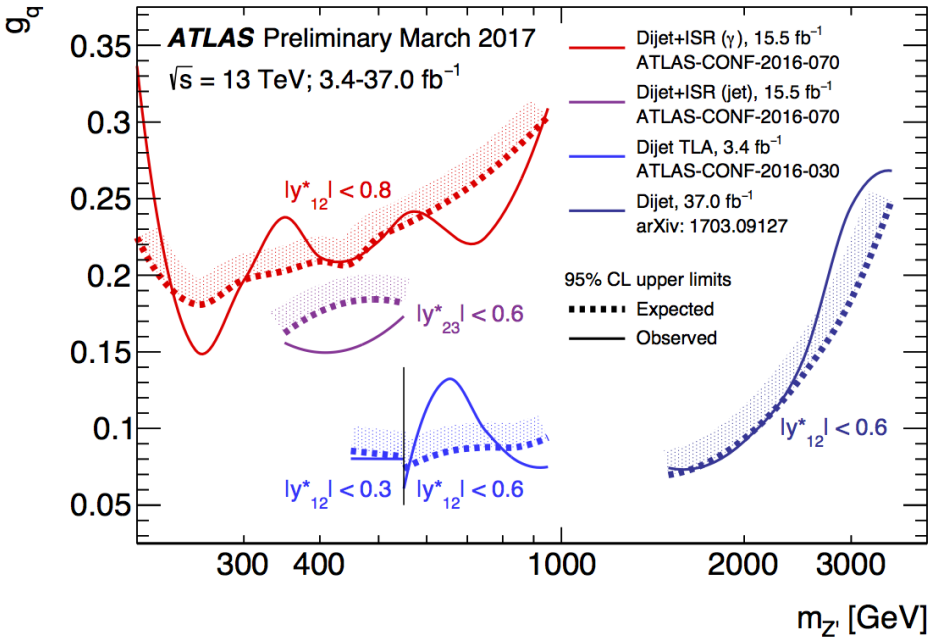

Figure 4.6: Combined 95% CL exclusion limits on Z' mass, $m_{Z'}$, and couplings to quarks, g_q, across multiple analyses. The dijet plus initial state radiation of a jet or photon covers the lowest mass region [113], the low mass dijet trigger level analysis covers the mid mass region [114], and this analyses covers the high mass region. M_{DM} and g_{DM} are kept fixed at 10 GeV and 1.5, respectively.

This provides phenomenologists with the ability to directly use the limits provided, without the need for information on detector response. Any new theory would then in principle only need to apply fiducial selections and non-perturbative corrections, and choose the folded Gaussian width and mass that most closely resembles the new particle [92].

4.9.1 Jet Energy Folding

First, events that pass both the fiducial selection at truth level and the corresponding selection at reco level fill a 2D distribution $N_{ij}^{matched}$. This can then be normalized to produce a folding matrix (Eq. 4.13), which gives the probability of an event in a truth bin i to be reconstructed in a reco bin j. In each truth (reco) bin, a truth (reco) efficiency defined as the fraction of events that pass both the truth and reco selections can be constructed as Eq 4.14 (Eq 4.15). The folding relationship between truth distribution $f(m_{jj}^T)$ and reconstructed level distribution $F(m_{jj}^R)$, is then given in Eq 4.16, where $\tilde{A}_{ij}$ is the global transfer matrix, which takes into account matching inefficiencies caused by detector effects.

$$A_{ij}^{matched} = \frac{N_{ij}^{matched}}{\sum_k N_{ik}^{matched}} \tag{4.13}$$

$$\epsilon_i^T = \frac{\sum_k N_{ik}^{matched}}{\sum_k N_{ik}^{matched} + N_i^{truthonly}} \tag{4.14}$$

$$\epsilon_i^R = \frac{\sum_k N_{ik}^{matched}}{\sum_k N_{ik}^{matched} + N_i^{recoonly}} \tag{4.15}$$

$$f_i \mapsto F_j = \sum_i f_i \times \epsilon_i^T \times A_{ij}/\epsilon_j^R \equiv \sum_i f_i \times \tilde{A}_{ij} \tag{4.16}$$

For signal samples, such as the Gaussian shapes, the global folding matrix is computed

using QCD MC. The Gaussian is then folded with the detector effects indicated in the folding matrix. When the resolution is small, the effects of folding are more noticeable, as detector effects are not perfectly Gaussian, and a perfect Gaussian was being used in the reco Gaussian limits. At larger resolution, this effect fades as the Gaussian width is much larger then the effect of the detector resolution. To improve limits, an approximation of a Gaussian resolution effect and a finer truth binning is used in the computation of the global folding matrix.

4.9.2 Results

The final limits are presented in Figure 4.7, where the observed limits for various widths of the Gaussian signal are shown in different colored lines, and the expected limit for the $\sigma/M = 0$ Gaussian is shown as a black dashed line, with 1σ and 2σ uncertainty on the expected limit shown as green and yellow bands. The limits are shown on $\sigma \times A \times BR$ for a hypothetical Gaussian shaped signal with cross section σ and unspecified branching ratio (BR) to jets.

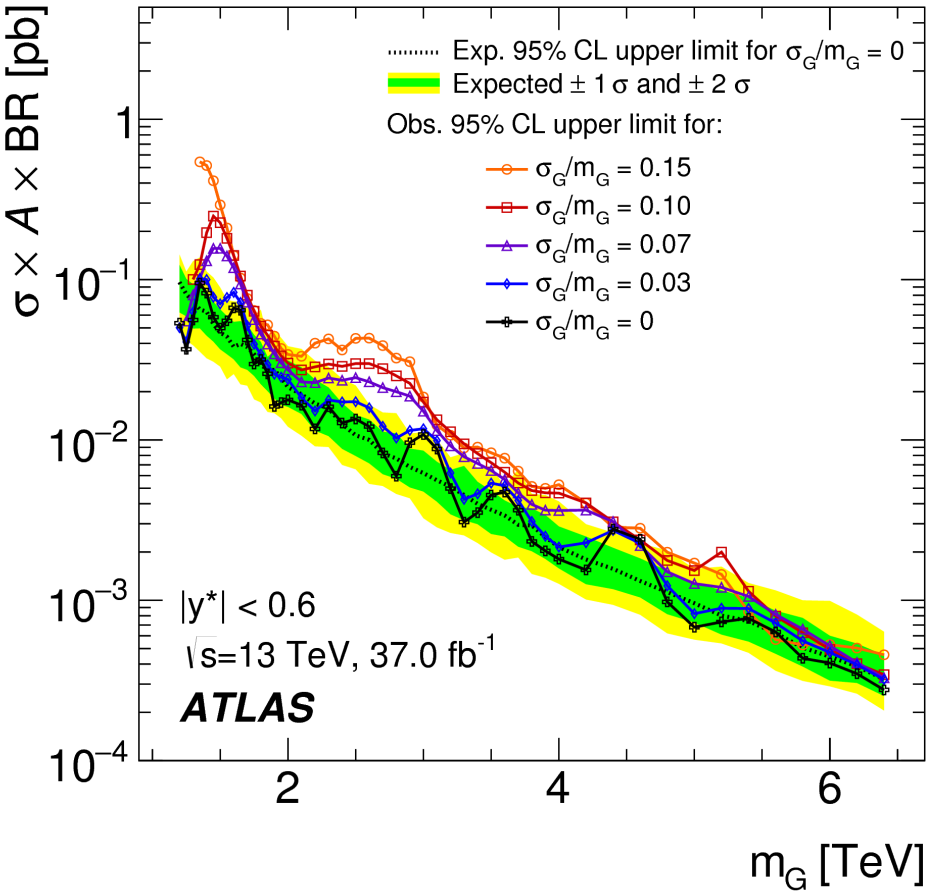

Figure 4.7: The 95% CL upper limits on cross-section times acceptance times branching ratio to two jets, $\sigma \times A \times BR$, for a hypothetical signal with a cross-section σ_G that produces a Gaussian contribution to the particle-level m_{jj} distribution, as a function of the mean of the Gaussian mass distribution m_G. Observed limits are obtained for five different widths, from a narrow width to 15% of m_G. The expected limit and the corresponding $\pm 1\sigma$ and $\pm 2\sigma$ bands are also indicated for a narrow-width resonance [106].

Chapter 5

Gaussian Processes

5.1 Gaussian Process Approach

As mentioned in Section 4.4, the polynomial fit to data will no longer be a viable option for a background estimation as more data is collected. As a more stable alternative to SWiFt, Gaussian Processes were tested as a new background fitting procedure. A Gaussian Process is defined as "a collection of random variables, any finite number of which have a joint Gaussian distribution" [115, 116]. Conceptually, Gaussian Processes provide generalization of the background fit $f(x)$ that is not tied to a particular functional form with a fixed number of parameters. Instead, the number of events at x is modeled as a Gaussian and the relationship between the intensity at different points is encoded in the *covariance kernel* $\Sigma(x, x')$. In this way, GPs allow for the description of a much broader set of functions (see Fig. 5.1) and provide a natural way to incorporate auxiliary information and prior knowledge.

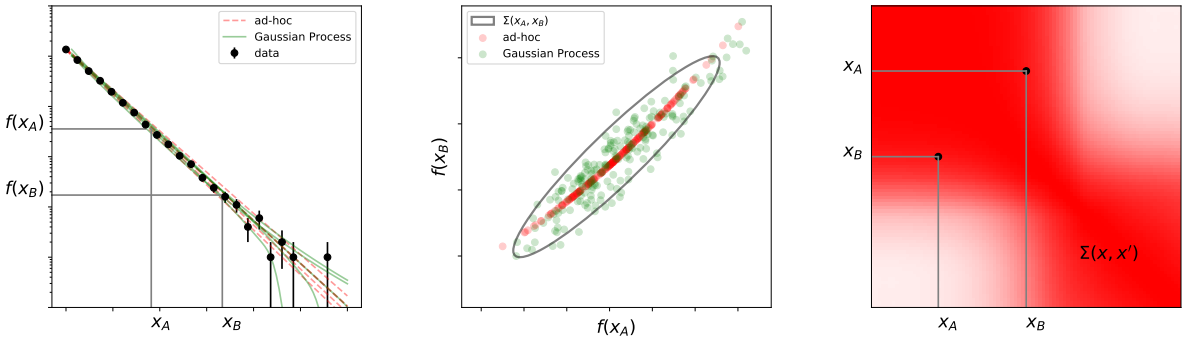

Figure 5.1: Schematic of the relationship between an ad-hoc function and the GP. An example toy dataset is shown (left) with samples from the posterior for an ad-hoc 1-parameter function (red) and a GP (green). Each posterior sample is an entire curve $f(x)$, which corresponds to a particular point in the (center) plane of $f(x_A)$ vs. $f(x_B)$. The red dots for the ad-hoc 1-parameter function trace out a 1-dimensional curve, which reveals how the function is overly-rigid. In contrast, the green dots from the GP relax the assumptions and fill a correlated multivariate Gaussian (with covariance indicated by the black ellipse). The covariance kernel $\Sigma(x, x')$ for the GP is shown (right) with $\Sigma(x_A, x_B)$ corresponding to the black ellipse of the center panel.

5.1.1 Gaussian Process Formulation

In an ideal case of background fitting, the background intensity $f(x)$ as a function of observable x would be known exactly. In this scenario, the expected total number of events is $\nu \equiv \int f(x)dx$ and the probability density $p(x) \equiv f(x)/\nu$, which leads to the unbinned extended maximum likelihood for a dataset $\mathcal{D} = \{x_1, \ldots, x_N\}$ with N observed events

$$p(\mathcal{D}) = \text{Pois}(N|\nu) \prod_{i=1}^{N} p(x_i) \; . \tag{5.1}$$

In the dijet analysis, this intensity $f(x)$ is a background model such as the four parameter polynomial fit function discussed in Section 4.4. This can be represented as some functional form with free parameters θ, given by $f(x|\theta)$. For the studies presented here, the functional form will be the 3 parameter fit function given in Eq. 5.7, as it was the fit function used in the Run I dijet analysis [94], which is used here as it was the most recent publicly available dataset at the time of this work. In the dijet case, the parameters θ are only constrained by the data $\mathcal{D}$; but more generally some auxiliary information $\mathbf{a}$ (eg calibration measure-

ments, theoretical considerations, etc) may be used to constrain the parameters through an additional constraint term leading to the likelihood

$$p(\mathcal{D}, \mathbf{a}|\theta) = \text{Pois}(N|\nu(\theta)) \prod_{e=1}^{N} p(x_e|\theta) \cdot p_{\text{constr.}}(\mathbf{a}|\theta) \; . \tag{5.2}$$

$$f(x|\theta) = \theta_0(1-x)^{\theta_1} x^{\theta_2} x^{\theta_3 \log x} \tag{5.3}$$

In addition to constraint terms in the likelihood corresponding to auxiliary measurements $\mathbf{a}$, it can be useful to incorporate terms in the likelihood that reflect prior knowledge; in the dijet case, this could be uncertainties on cross section measurements or JES.

In situations with many events, the likelihood can be approximated with a binned likelihood where the Poisson counts in each bin y_i are accurately approximated with a Gaussian distribution. In that case, the likelihood of Eq. 5.2 can be approximated as

$$\begin{aligned} p(\mathbf{y}, \mathbf{a}|\theta) = & \quad \textstyle\prod_{i=1}^{n} \text{Pois}(y_i|\bar{f}(x_i|\theta)) \cdot p_{\text{constr.}}(\mathbf{a}|\theta) \\ \approx & \quad \text{Gaus}(\mathbf{y}|\bar{f}(\mathbf{x}|\theta), \sigma^2) \cdot \text{Gaus}(\bar{f}(\mathbf{x}|\theta)|\mu, \mathbf{\Sigma}) \, , \end{aligned} \tag{5.4}$$

where $\mathbf{x}$ are the bin centers, $\mathbf{y}$ are the observed bin counts, and $\bar{f}(\mathbf{x}|\theta)$ are the expected bin counts from averaging $f(x|\theta)$ within the corresponding bin. The first term of Eq. 5.5 is the per-bin Poisson statistical fluctuation, while the second term is an $n \times n$ multivariate Gaussian distribution that approximates the effect of $p_{\text{constr.}}(\mathbf{a}|\theta)$ propagated to the expected bin counts $\bar{f}(\mathbf{x}|\theta)$.

Gaussian Processes provide a natural way to expand around the overly restricted parametrized model and fill in the full space of possibilities. Instead of providing a parametric form, the mean is modeled directly as (μ) and covariance functions (Σ) of the Gaussian process defined

as

$$\mu(x) = \mathbf{E}[f(x)] \tag{5.5}$$

$$\Sigma(x, x') = \mathbf{E}[(f(x) - \mu(x))(f(x') - \mu(x'))] \, . \tag{5.6}$$

This covariance *kernel* Σ is then augmented with the diagonal (uncorrelated) statistical component $\sigma^2(\mathbf{x})\mathbf{I}$ to provide the likelihood for the observed bin counts $\mathbf{y}$.

To use a GP for high-energy physics, the kernel should directly encode our understanding of the underlying physics, which is manifest as covariance among the bin counts.

5.1.2 Covariance Structures from Physical Quantities

One such physical quantity that can be encoded into the *kernel* is JES. As seen in Section 3.1.6, the ATLAS JES uncertainty is only a few percent for jets with p_{T} of around 1 TeV where data are plentiful, while the the limited size of observed examples for higher-p_{T} jets requires an alternate approach to estimating the JES. The resulting JES uncertainty therefore grows rapidly with m_{jj} and has an impact of at most 15% [88]. To illustrate the covariance due to the JES uncertainty, consider a simplified two-parameter model for the impact on the m_{jj} distribution: $\mathrm{J}(z, \theta) = 1 + 15\% \, \theta_1 z^4 + 5\% \, \theta_2 (1 - z)$, where z is the true dijet invariant mass and $z_{\mathrm{max}} = 7$ TeV. The best fit 3-parameter fit to data (as shown in Figure 5.2)is used as a proxy for $f(z)$ and a smearing is applied to mimick real data with $W(x|z, \theta) = \mathrm{Gaus}(x|z \, \mathrm{J}(z/z_{\mathrm{max}}, \theta), \sigma_x)$, where $\sigma_x = 2\% z$ is the dijet invariant mass resolution [106].

By assuming a uniform prior and an appropriate scaling for θ, samples can be drawn from the posterior $\mathrm{Gaus}(\theta_1|0, 1)\mathrm{Gaus}(\theta_2|0, 1)$ and propagate the uncertainty in θ through to the

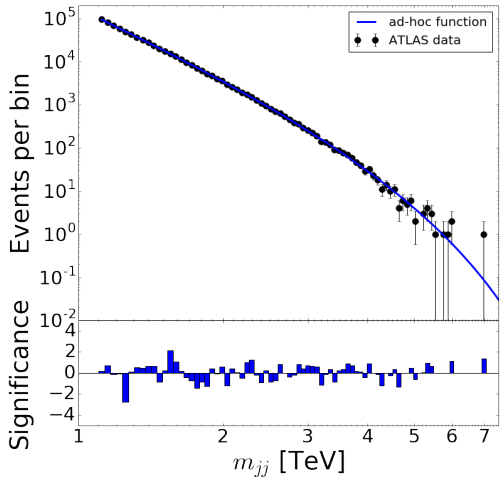

Figure 5.2: Invariant mass of dijet pairs reported by ATLAS [94] in proton-proton collisions at $\sqrt{s} = 13$ TeV with integrated luminosity of 3.6 fb^{-1}. The blue line is a fit using the first three terms of Eq. 5.7. The bottom pane shows the significance of the residual between the data and the fit.

predicted bin counts $\bar{f}(\mathbf{x}|\theta)$ as in Eqs. 5.4 and 5.5. This allows the covariance matrix Σ to be built using the simulation shown in Fig. 5.3. As expected, there is roughly a block-diagonal structure defined by low and high mass regions.

Similarly, the uncertainty in the theoretical distribution arising from PDF uncertainty can be added to the *kernel*, such as that in the ATLAS 7 TeV analysis [117, 118]. Figure 5.3 corresponds to the PDF uncertainties described in Ref. [119] for NLO calculations from `POWHEG-BOX` [120, 121] using the $\mathcal{S}_{\text{no-jet}}$ PDF sets provided in `NNPDF3.0` [122]. In this case, sum rules in the PDFs lead to anti-correlation between low- and high-mass regions.

5.1.3 Implicit covariance in current background models

It is also instructive to examine the effective covariance implied by current approaches: the 3 parameter fit and the SWiFt. Again this is studied through the relationship of Eqs. 5.4 and

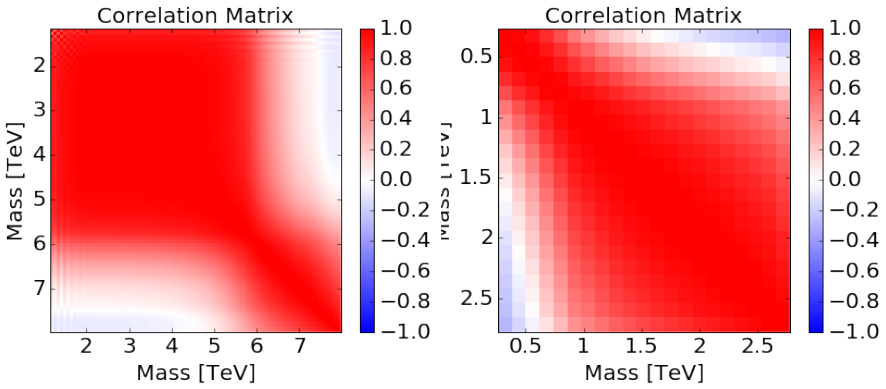

Figure 5.3: Correlation coefficients between pairs of mass bins due to variations in the jet energy scale (left) or parton distribution functions (right). These demonstrate the broad but smoothly varying influence of these effects on the mass spectrum.

5.5. In the case of the 3 parameter fit function of Eq. 5.7, the posterior can be constructed for p given the ATLAS data shown in Fig. 5.2 and a uniform prior on p. The posterior is sampled using `emcee` [123], a Python implementation of the affine-invariant ensemble sampler for Markov Chain Monte Carlo (MCMC) [124]. From the posterior samples of $p \sim p(\theta|\mathbf{y})$ the covariance matrix Σ can be built, and is shown in Fig. 5.4. The global structure of the covariance resembles those arising from PDF uncertainties, but recall that the model only sweeps out a 3-dimensional subspace in the much larger space of functions with this same covariance.

$$f(x) = p_1(1-x)^{p_2}x^{p_3} \tag{5.7}$$

In the case of the SWiFt approach, the covariance is estimated from a table of $f(x_i)$ values, but instead of posterior samples, a single fit for each of 50 mass windows is performed. For the k^{th} window, if the bin is outside the window the fit recorded is 0, otherwise $f(x_i|\hat{p}_k)$ is recorded, where $\hat{p}_k$ is the best fit value of p for the fit restricted to the window. The covariance is calculated from these recorded values. This method should create a covariance structure which is limited to the diagonal band, as each fit includes only a small portion of the distribution – indeed this is what is seen in Figure 5.4. While the SWiFt approach

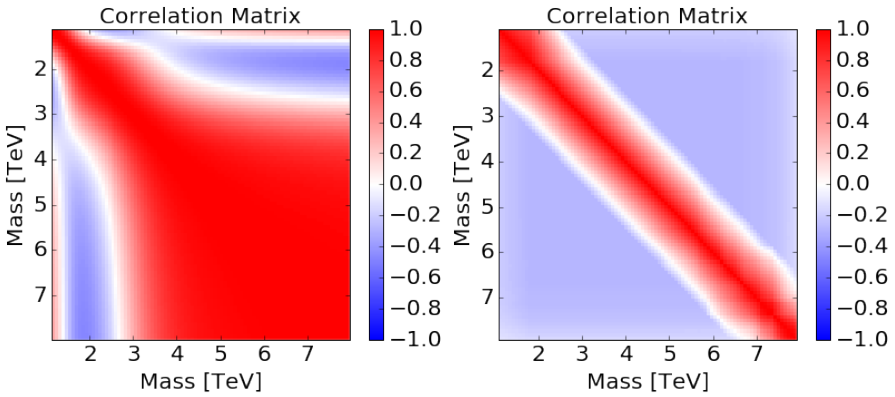

Figure 5.4: Correlation coefficients between pairs of mass bins from many samples of the global ad-hoc fit (left) and the sliding window fit (right). The plot of the global fit reveals non-physical pivot points where the ad-hoc function is less flexible. The sliding window fit has a strictly limited correlation, by construction.

provides more flexibility and better scaling to high luminosities than a global fit, the piecewise approach to background modeling complicates the downstream statistical analysis.

5.1.4 Kernel construction

This kernel describes a maximal covariance with amplitude A that falls off with a length-scale l. If $|x - x'| \gg l$, then the covariance is very small. The parameters of the kernel are traditionally referred to as *hyperparameters*, and the values of the hyperparameters can be fit either a priori (eg by considering simulated or control samples), or to the data simultaneously with the hypothesis test itself.

For the dijet analysis, it is clear that a varying length scale is needed. For this reason, we start with the Gibbs kernel [115, 125], which has a non-constant length scale $l(x)$. In this case, a length scale which increases with mass is used to describe the tightening smoothness requirements in the low-statistics tail, and to accommodate the dijet mass data from ATLAS, which has bins whose width increases with mass. For this reason, the length scale function used is linear with mass, given by $l(x) = (bx + c)$. The definition of the length

scale is critical, as it defines the smoothness of the GP description, which prevents the background model from accommodating the localized deviations from smoothness which are the resonance signals. Finally, an amplitude term is used to model the variance with a falling exponential term. The final kernel is:

$$\Sigma(x,x') = Ae^{\frac{-(x+x')+d}{2a}}\sqrt{\frac{2l(x)l(x')}{l(x)^2+l(x')^2}}e^{-\frac{(x-x')^2}{l(x)^2+l(x')^2}} \tag{5.8}$$

The parameters of the kernel (A, a, b, c, d) become the hyperparameters of the GP, and will be determined during the fit to the data, described below.

5.1.5 Mean function

It is common to use $\mu(x) = 0$ for the mean of a GP, partially because once conditioned on the observations $\mathbf{y}$, the posterior mean usually adapts to this offset remarkably well. However, the background fit is very large, which would make modeling the background as fluctuations around a zero mean would be quite difficult. Also, there already exists a reasonable background estimate in the three-parameter fit function, so there is no reason not to use it. Therefore, the three parameter fit function is used as the mean $\mu(x)$ of the GP, which contributes an additional three hyper-parameters, $(\theta_0, \theta_1, \theta_2)$. The results are very robust to the choice of the mean, as the key to the performance is really in the choice of the kernel.. Rather, the mean only needs to roughly correspond to the underlying structure of the distribution, while the covariance function encodes the smoothness.

In the case of signal-plus-background hypothesis testing with a known signal model $f_s(x|\theta_s)$, the mean function also includes the signal contribution. Due to the linear relationship between $\mathbf{y}$ and $\mu(\mathbf{x})$ in the Gaussian, this is numerically equivalent to subtracting the signal expectation from the observation and modeling the residuals with the background-only

GP.

5.1.6 Incorporating GPs into the statistical procedure

GPs are most commonly presented in a Bayesian formalism where the mean and covariance kernel are interpreted as a prior distribution over the space of functions. Then given the observations $\mathbf{y}$ the GP is updated to represent a posterior distribution over the space of functions. Because both the prior and the posterior are Gaussians there are explicit formula for the posterior mean and covariance that rely on basic linear algebra [115]. In particular

$$\mu(\mathbf{x}_*|\mathbf{y}) = \mu(\mathbf{x}_*) + \Sigma(\mathbf{x}_*, \mathbf{x})[\Sigma(\mathbf{x}, \mathbf{x}) + \sigma^2(\mathbf{x})\mathbf{I}]^{-1}(\mathbf{y} - \mu(\mathbf{x})) \tag{5.9}$$

and

$$\begin{aligned} \Sigma(\mathbf{x}_*, \mathbf{x}'_*) &= \Sigma(\mathbf{x}_*, \mathbf{x}'_*) \\ &- \Sigma(\mathbf{x}_*, \mathbf{x}')[\Sigma(\mathbf{x}, \mathbf{x}') + \sigma^2(\mathbf{x})\mathbf{I}]^{-1}\Sigma(\mathbf{x}, \mathbf{x}'_*) \ , \end{aligned} \tag{5.10}$$

where $\mathbf{x}_*$ are the values where the posterior GP is being evaluated and $\mathbf{x}$ are the values being conditioned on. In a typical binned analysis $\mathbf{x}$ and $\mathbf{x}_*$ would both be the the bin centers. In addition, fitting the hyperparameters of a GP is usually based on maximizing the marginal likelihood, which has the explicit form

$$\log L = -\frac{1}{2}\log|\Sigma| - (\mathbf{y} - \mu(\mathbf{x}))^T\Sigma^{-1}(\mathbf{y} - \mu(\mathbf{x})) - \frac{n}{2}\log 2\pi \ . \tag{5.11}$$

In order to take advantage of the closed form solutions above and fast linear algebra implementations, the statistical fluctuations are typically approximated as $\sigma^2(\mathbf{x}) = \mathbf{y}$ instead of the more accurate Poisson mean.

5.1.7 Fitting Procedure

In the studies below the marginal likelihood of Eq. 5.11 is used for fitting the hyperparameters, which are optimized using MINUIT [102]. In later studies, a another approach is used. This is a two-step process where one first calculates the posterior mean of Eq. 5.9 and then uses $\mu(x)$ as the intensity for the Poisson likelihood of Eq. 5.1 or its corresponding binned version. The background model can be conditioned on the signal hypothesis being tested, since the signal's parameters are present in the prior mean function.

The software package GEORGE [126] is used for the GP regression, which has been extended by implementing the custom kernel.

The posterior mean and posterior correlation matrix from fitting the GP to the ATLAS dataset are shown in Figs. 5.5 and 5.6. By visual inspection, the mean function fits the data well and the correlation is constrained near the diagonal, with the off diagonal dying off quickly. This structure reflects the locality of the GP, where nearby bins are closely connected but bins far from each other in mass are uncorrelated.

5.2 Performance studies

Figures 5.5 and 5.6 demonstrate the fit (posterior mean) of the GP to a single dataset collected by ATLAS in proton-proton collisions at $\sqrt{s} = 13$ TeV with integrated luminosity of 3.6 fb^{-1} [94]. More important is the characterization the GP approach from fits to an ensemble of datasets with independent statistical fluctuations and increasing luminosity. Toy samples are constructed by smoothing the ATLAS data, scaling it to the desired luminosity, and generating independent samples by adding Poisson noise to each bin.

Below, the performance of the GP approach in these datasets is presented under two

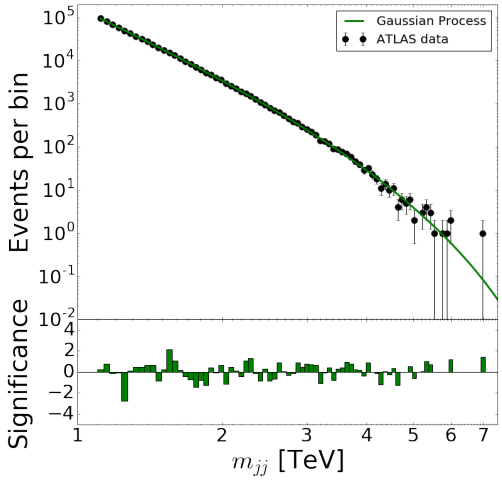

Figure 5.5: Invariant mass of dijet pairs reported by ATLAS [94] in proton-proton collisions at $\sqrt{s} = 13$ TeV with integrated luminosity of 3.6 fb^{-1}. The green line shows the resulting Gaussian process background model. The bottom pane shows the significance of the residual between the data and the GP model.

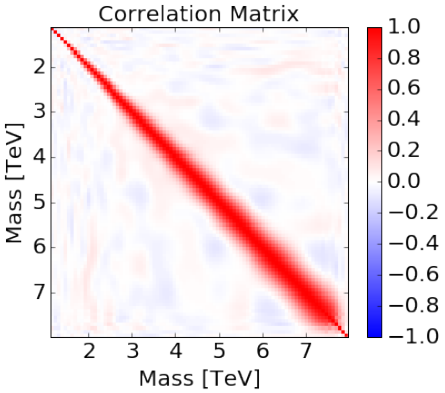

Figure 5.6: Correlation between pairs of mass bins from the GP fit, which shows the largely diagonal nature, with increasing length scale at higher mass.

aspects of hypothesis testing:

- Background-only tests: these studies test whether the GP has sufficient flexibility to describe the typical background spectrum, assuming no signal.
- Signal-plus-background tests: these studies combine a GP background with a specific signal model and tests the power of a hypothesis test based on the GP background. This requires that the GP model not be so flexible that it can absorb the localized signal into the background model.

5.2.1 Background only tests

The performance of the GP background model is evaluated in the toy datasets described above. For each toy dataset, the GP is fit to the dataset, the posterior mean from Eq. 5.9 is extracted, and a χ^2 quantity from $\sum_i (y_i - \mu(x_i|\mathbf{y}))^2/\mu(x_i|\mathbf{y})$ is evaluated; note that in this test the posterior covariance matrix of Eq. 5.10 is not incorporated. Figure 5.7 shows the $\pm 1\sigma$ about the average $\mu(\mathbf{x}|\mathbf{y})$ from these toys, with the ATLAS data to guide the eye, and the ad-hoc fit for comparison. The GP based on the kernel in Eq. 5.8 has more flexibility at high mass, but also provides a superior fit, as measured by the χ^2/dof statistic. The number of degrees of freedom for the ad-hoc fit is 3, while the GP has 8 hyperparameters (3 from the mean function and 5 from the kernel). Figure 5.8 shows the distribution of χ^2/dof, which peaks near $\chi^2/\text{dof} = 1$ for the GP model and is significantly larger than unity for the ad-hoc function.

A critical test of the Gaussian process model is its robustness with increasing luminosity, where the ad-hoc approach has failed in collider data [94, 106]. In Figure 5.9, the mean and standard deviation of the χ^2/d.o.f. are shown as a function of integrated luminosity in the toy data, demonstrating the robustness of the GP approach.

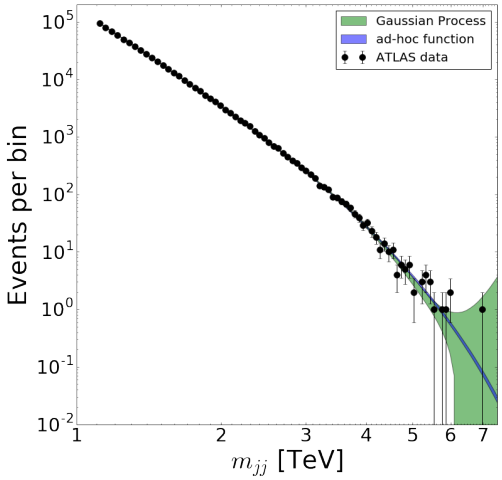

Figure 5.7: Tests of the Gaussian process and three-parameter ad-hoc function in toy data generated from the ATLAS data. Shown are the $\pm 1\sigma$ band about the mean background models, with the ATLAS data overlaid for reference.

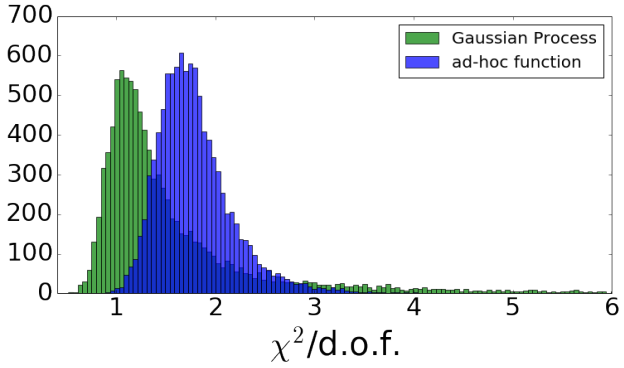

Figure 5.8: The distribution of χ^2 per degree of freedom in toy data generated from the ATLAS data at luminosity of 3.6 fb^{-1}. While the goodness of fit for the ad-hoc function degrades with more data, the GP is robust.

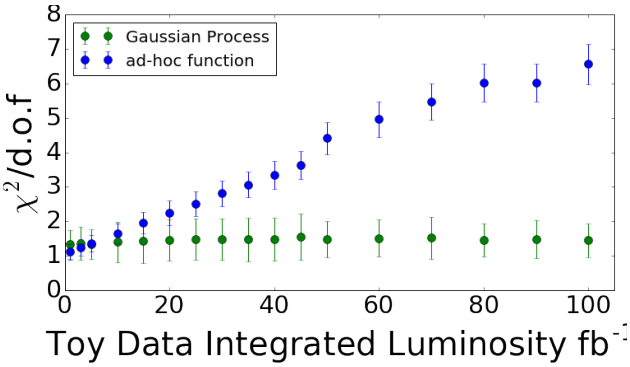

Figure 5.9: Mean and standard deviation of the χ^2/d.o.f. measure in toy data generated from ATLAS collisions, as a function of integrated luminosity, for the ad-hoc fit and the Gaussian process.

5.2.2 Background plus signal fits

Adding more flexibility to the background model guarantees a better fit to background-only toys; however, this generally comes at the loss of power in a search for a signal. A background model that is flexible enough to incorporate a signal contribution will have no discovery power.

Here, the GP model's performance is tested in the toy data constructed as described earlier, but with signal injected as well.

A generic Gaussian resonance is used as the injected signal, and performed tests with various values for the signal mass, width and amplitude. The hyperparameters of the GP (both for the background mean and kernel functions) are fixed from the fit to the ATLAS dataset; in a realistic application, these would be fixed from fits to simulated samples. Only the three parameters (amplitude, mass, and width) of the Gaussian signal are fit. For the parametric fit, all six parameters are fit: the three fit function parameters and three signal parameters. An example of this background-plus-signal fit is shown with an injected 2.5 TeV Gaussian signal shape in the top panel of Fig. 5.10.

This single example is illustrative and qualitative, but the statistical test for the presence

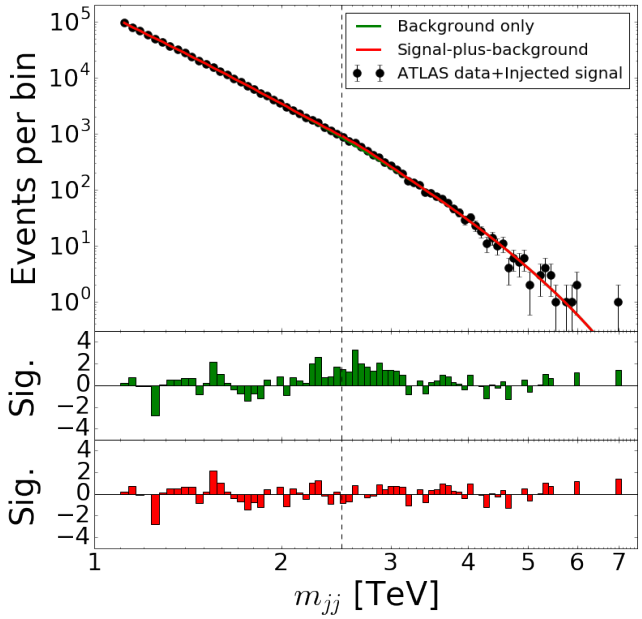

Figure 5.10: Invariant mass of dijet pairs reported by ATLAS [94] in proton-proton collisions at $\sqrt{s} = 13$ TeV with integrated luminosity of 3.6 fb^{-1} with a false signal injected at $m_{jj} = 2.5$ TeV. The green line is the Gaussian process background-only model; the red line is the signal-plus-background model. The central pane shows the significance of the residual between the data and the background fit; the bottom-pane shows the significance of the residual between the data and the background-plus-signal fit.

of a signal in observed data relies on the likelihood ratio Λ between the background-only and the signal-plus-background hypotheses. The likelihood ratio between the two hypotheses in cases background-only toy data as well as background-plus-signal toy data is calculated. This involves the use of Eq. 5.9 twice, as the posterior mean background prediction is different for the background-only and signal-plus-background fits. This is analogous to the profile likelihood ratio where there are two fits and the conditional maximum likelihood estimate of the background in the background-only case is generally different from the background estimate in the signal-plus-background fit.

The distribution of $-2\log\Lambda$ is shown in Figure 5.11 for background-only toys for both the 3-parameter ad-hoc function and the GP. In these fits the signal mass and width were fixed and the signal strength was treated as the parameter of interest. In the parametric case, Wilks' theorem can be invoked, which says this distribution should follow a chi-square distribution if the true distribution generating the data corresponds to some point in the parameter space of the background model [127]. However, in this case, the background-only toys were not generated from the ad-hoc function, instead they were generated from a smoothed version of the ATLAS data. Nevertheless, the distribution closely tracks a chi-square distribution.

In the case of the GP, there is an issue in that the likelihood of Eq. 5.1 only reflects the Poisson fluctuations, while the constraint terms the kernel encodes are not reflected in this likelihood. In this case there is not significant tension between the data and the covariance kernel so the likelihood ratio distribution also tracks a chi-square distribution. In general, this will need to be checked explicitly.

Next the power of the search is addressed by considering the distribution of $-2\log\Lambda$ for signal-plus-background toys with signals of various masses. Figure 5.12 shows the mean of the $-2\log\Lambda$ distribution for the ad-hoc function and the GP model. The added flexibility of the GP does not degrade the power of the search – in fact, the GP has more sensitivity to a

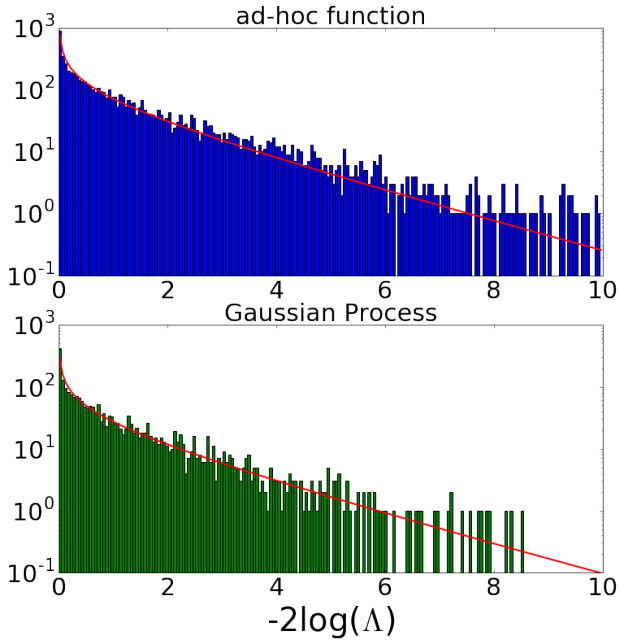

Figure 5.11: Distribution of $-2\log(\Lambda)$, where Λ is the likelihood ratio between the background-only and the background-plus-signal hypotheses, for toy data with no signal present, shown for both the ad-hoc fit (top) and the Gaussian process background model (bottom). Overlaid in red is a χ^2 distribution with one degree of freedom.

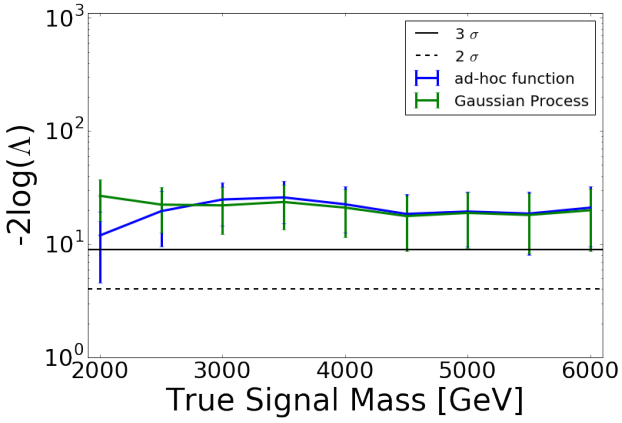

Figure 5.12: Mean log likelihood ratio (Λ) between the background-only and the background-plus-signal hypotheses, shown both for the of Gaussian process model and the ad-hoc fit, in 1000 toy data sets for varying injected signal mass. Solid and dashed lines indicate the threshold for 3σ significance and for an α-level of 0.05.

signal at low mass, while the two methods are comparable at high mass. This gain in power is logically possible because the distribution used to true generate the background (which is normally unknown) does not correspond to the ad-hoc function exactly. In this case the GP background model is able to more accurately follow the true background (generated from smeared ATLAS data) than the ad-hoc function.

If a signal is detected, it is also vital to be able to extract the signal parameters. For a two choices of signal mass (m_{jj} = 3 and 5 TeV), fits to signal-plus-background toys are performed by fitting the mass, width, and signal strength. Figure 5.13 shows that the extracted signal width and yield are reliable estimators of the true values.

5.3 Modeling generic localized signals

The search for specific resonances above a smooth background is only one type of search strategy. More broadly, a background fitting procedure should be sensitive to localized deviations that take different, potentially unanticipated shapes. For instance, a cascade decay can lead to triangular distributions with a sharp endpoint [128], though helicity correlations can modify this shape in detail. Searches like this require balancing a small number of tests of the background-only model using generic properties of a signal and a larger number of tests of the background-only model using more specific signal properties. A single number-counting search using the full mass range is very generic, but has very little power. Conversely, an enormous scan over specific hypothesized signals individually have more power, but this strategy suffers from a large look-elsewhere effect.

Historically, the search for generic signals over a background model uses BumpHunter [103], as done in the dijet analysis. This approach imposes only minimal structure on the signal: that it is a localized, contiguous excess. This approach can be effective, but it has signifi-

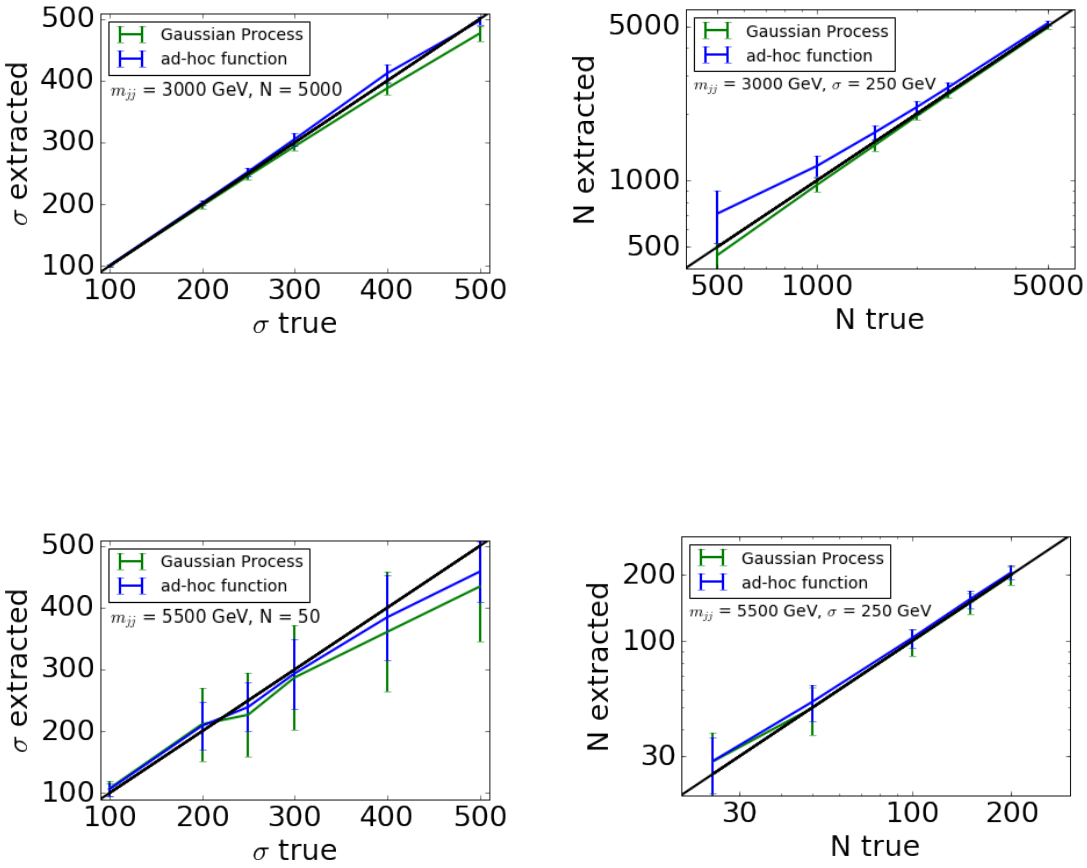

Figure 5.13: Extracted signal parameters versus true parameters for an injected Gaussian signals with m_{jj} = 3 TeV (top) and m_{jj} = 5.5 TeV (bottom). Left: the extracted signal width (σ) for a fixed signal yield. Right: the extracted signal yield (N) for a fixed signal width (σ = 250 GeV). Results are shown for both the Gaussian Process background model (green) and the ad-hoc fit function (blue).

cant practical drawbacks as it contains many ad-hoc algorithmic elements. For example, in common usage BumpHunter requires that the excess be localized to at least two bins, and at most half of the bins. This algorithmic characterization of the signal is effective, but it is difficult to interpret and characterize statistically. Secondly, to address the look-elsewhere effect, this approach explicitly accounts for multiple testing and calibrates the distribution of the test statistic by applying the entire procedure to background-only toys. This requires a global background-only prediction, which is complicated when relying on the data to help fit the background model. In particular, if a signal is present in the data, it is unclear how this impacts the background estimate. Thus far, the main strategy has been an iterative background estimation procedure that defines a signal region and extrapolates the background fit into this region. This approach introduces a coupling of algorithmic decisions with the statistical considerations. Similarly, in the context of a sliding window background model, the procedure is further complicated by the fact that there is not a single global background prediction, but a set of correlated background predictions specific to the signal window under consideration.

In this section, an alternative approach is considered, which uses a GP to model a generic localized signal. In this case, the basic physical requirement of the localized signal can be encoded directly in the kernel of the signal GP, rather indirectly through ad-hoc algorithmic choices. This approach allows signal-plus-background fits where the signal GP absorbs the localized excess and the background GP accounts for the background. The background component from such a fit can provide global background estimate to be used in the context of a BumpHunter approach even when a signal is present in the data. More importantly, this approach enables hypothesis tests of the background-only model against a weakly specified signal-plus-background model directly based on the likelihood ratio or Bayes factor.

The study of this approach is initiated with a specific signal GP described by the following

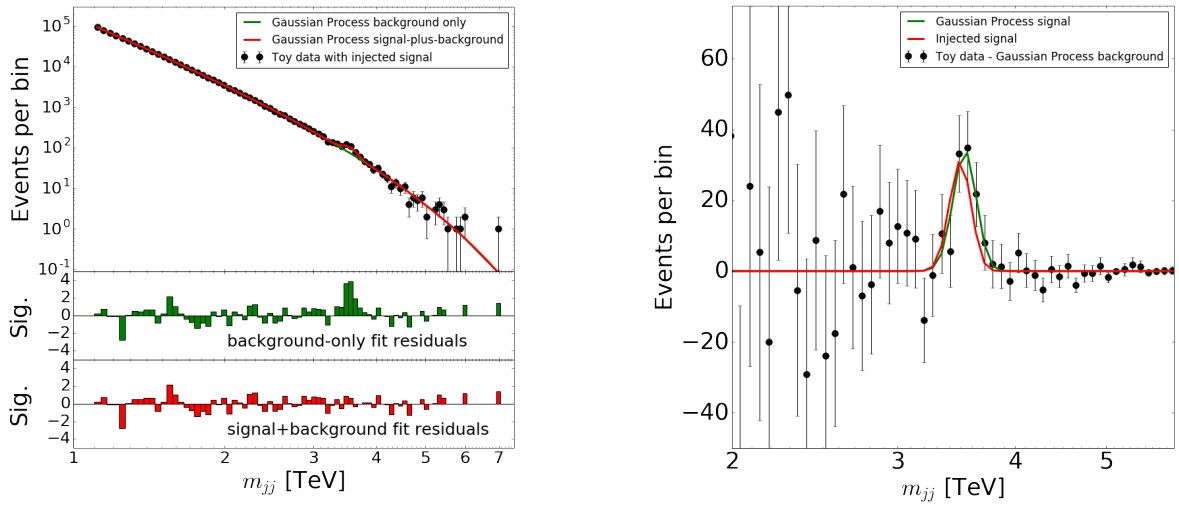

Figure 5.14: Top, an example fit with both a GP background and signal model to toy data with injected triangular signal. The panes below show the significance of residuals between the toy data and the background model, the toy data and the background-and-signal model. Bottom, the residuals between the toy data and the background model, overlaid with the injected signal and the fitted GP signal.

kernel

$$\Sigma(x, x') = Ae^{-\frac{1}{2}(x-x')^2/l^2} e^{-\frac{1}{2}((x-m)^2+(x'-m)^2)/t^2}, \tag{5.12}$$

which has three main terms. The first term A is an overall amplitude for the signal. The second term is the standard exponential-squared kernel with length scale l. The third term is an envelope that localizes the signal around a mass m with a width t, which is analogous to the mass window.

To demonstrate the flexibility of this kernel, signal-plus-background fits for a variety of signal shapes were performed. Figure 5.14 shows the background extraction on both a linear piecewise triangular signal and Figure 5.15 shows a square signal; both have been smeared to model detector jet energy resolution effects. These studies indicate the GP signal is able to accommodate a wide variety of signal shapes leaving the background model responsible for for the smoother background-only component.

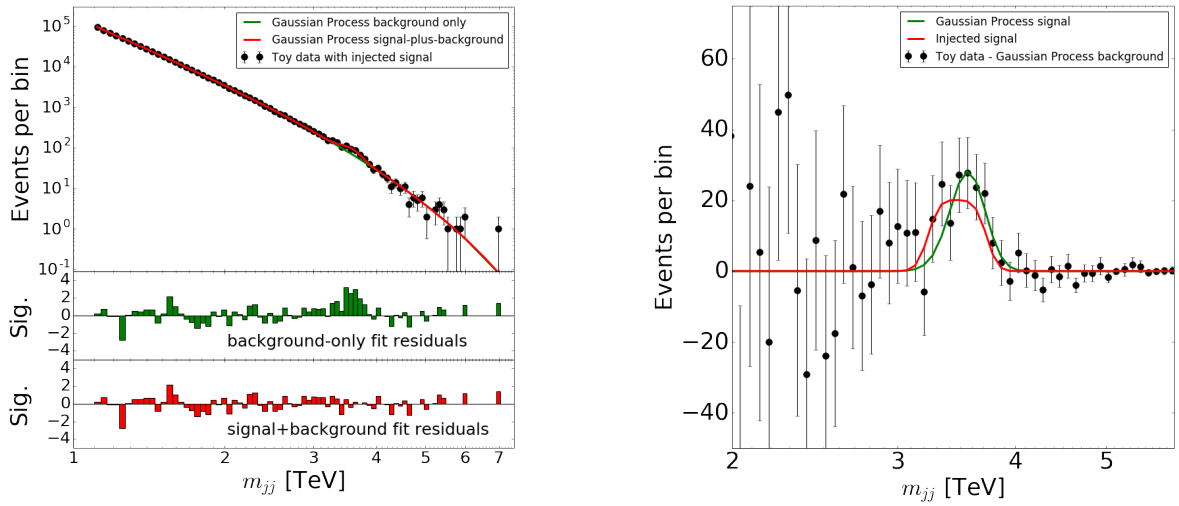

Figure 5.15: Top, an example fit with both a GP background and signal model to toy data with injected square signal. The panes below show the significance of residuals between the toy data and the background model, the toy data and the background-and-signal model. Bottom, the residuals between the toy data and the background model, overlaid with the injected signal and the fitted GP signal.

5.3.1 Look-elsewhere effect

This approach does not eliminate the look-elsewhere effect that arises from considering multiple signal hypotheses. Instead of a finite number of search windows or signal hypotheses, the GP describes a continuous family of signal hypotheses. This is not fundamentally different than the look-elsewhere effect that arises from considering a signal model with an unknown mass or width, though it is in a non-parametric setting. While both GP and the the simple example of an unknown mass correspond to an infinite number of signal hypotheses, they are highly correlated and the effective trials factor is finite [104, 129].

Fundamentally, the fact that some parameters of the signal model (eg mass and width) have no effect in the background only-case (in statistics jargon, they are *not identified under the null* [130]) means that the conditions necessary for Wilks's theorem are not satisfied and the log likelihood ratio distribution will not take on the chi-square form. While there are

approaches to estimate the asymptotic distribution of the likelihood ratio test statistic for signal models with one or a few parameters [104, 129], we are not aware of an asymptotic theory in the case of GPs. The lack of an asymptotic theory has little practical impact since even in the case of signal models with a few parameters, the asymptotic distributions are only accurate for very significant ($\gtrsim 4\sigma$) excesses, and background-only toys are usually used in the interesting region of $2-5\sigma$.

The effective trials factor will depend on the specific background model and the kernel used for the signal GP. To illustrate this, the log-likelihood ratio distribution for an ensemble of background-only toys is evaluated, similar to what was done in Fig. 5.11. In this case the mass hyperparameter m is fit in the range 2-5 TeV and the hyperparameter $t = 600$ GeV is fixed, which specifies that the signal is localized roughly to a 600 GeV region. Naively, the trials factor from allowing the mass to float (range over width) to be about 6. In addition two different values for the length scale are considered: $l = t$ and $l = t/3$. Smaller values for l allow the signal GP more flexibility within the effective mass resolution, and thus further increase the trials factor. Figure 5.16 shows the log-likelihood ratio distribution from these tests, confirms the intuition that smaller values of l imply a larger look-elsewhere effect, and demonstrates that it is straight forward to directly calculate the *global* p-value from background-only toy Monte Carlo.

5.4 Conclusion

This analysis presented results of the resonant dijet analysis with Run II data, totally $37 fb^{-1}$. Improved limits were set on the mass of four new physics signal models, as well as limits on mass and coupling of a dark matter model. Also, a new folding procedure was implemented to allow for more interpretable limits on generic Gaussian signal models. Finally, a new background fitting procedure was designed and tested. This Gaussian Process Regression

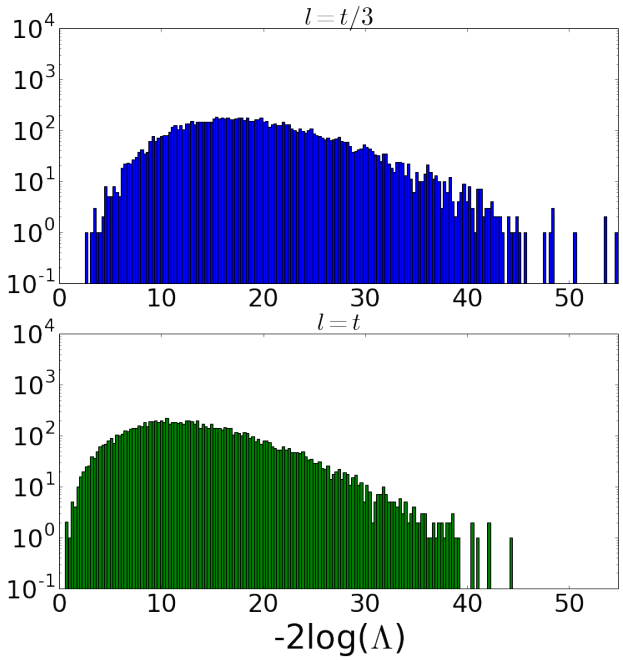

Figure 5.16: Distribution of $-2\log(\Lambda)$, where Λ is the likelihood ratio between the background-only and the background-plus-signal hypotheses, for toy data with no signal present. The deviation from the χ^2_1 distribution is due to the look-elsewhere effect. The top plot corresponds to a signal GP with $l = t/3$, which has more flexibility and a larger trials factor than the bottom plot with $l = t$.

demonstrated it's potential to replace current background estimation techniques by consistently outperforming the standard dijet fit function. In future analyses, Gaussian Processes will be thoroughly vetted as a background estimation, and will hopefully be able to replace the current approach and become the standard background estimation procedure.

Bibliography

[1] A. Collaboration, "Observation of a new particle in the search for the standard model higgs boson with the atlas detector at the lhc," *Physics Letters B*, vol. 716, no. 1, pp. 1 – 29, 2012.

[2] C. Collaboration, "Observation of a new boson at a mass of 125 gev with the cms experiment at the lhc," *Physics Letters B*, vol. 716, no. 1, pp. 30 – 61, 2012.

[3] A. Purcell, "Go on a particle quest at the first cern webfest. le premier webfest du cern se lance à la conquête des particules," p. 10, Aug 2012.

[4] J. Goldstone, "Field theories with superconductor solutions," *Il Nuovo Cimento (1955-1965)*, vol. 19, pp. 154–164, Jan 1961.

[5] Y. Nambu, "Axial vector current conservation in weak interactions," *Phys. Rev. Lett.*, vol. 4, pp. 380–382, Apr 1960.

[6] J. Goldstone, A. Salam, and S. Weinberg, "Broken symmetries," *Phys. Rev.*, vol. 127, pp. 965–970, Aug 1962.

[7] N. Arkani-Hamed, S. Dimopoulos, and G. Dvali, "The hierarchy problem and new dimensions at a millimeter," *Physics Letters B*, vol. 429, no. 3, pp. 263 – 272, 1998.

[8] N. Arkani-Hamed, S. Dimopoulos, and G. Dvali, "Phenomenology, astrophysics, and cosmology of theories with submillimeter dimensions and tev scale quantum gravity," *Phys. Rev. D*, vol. 59, p. 086004, Mar 1999.

[9] L. Randall and R. Sundrum, "Large mass hierarchy from a small extra dimension," *Phys. Rev. Lett.*, vol. 83, pp. 3370–3373, Oct 1999.

[10] G. Bertone and D. Hooper, "A History of Dark Matter," *Submitted to: Rev. Mod. Phys.*, 2016.

[11] K. Thorne, "Nonspherical gravitational collapse and spacetime singularities," in *J.R. Klauder, Magic Without Magic*, vol. 231, San Franscisco, 1972.

[12] D. M. Gingrich, "Quantum black holes with charge, color and spin at the lhc," *Journal of Physics G: Nuclear and Particle Physics*, vol. 37, no. 10, p. 105008, 2010.

[13] X. Calmet, W. Gong, and S. D. Hsu, "Colorful quantum black holes at the lhc," *Physics Letters B*, vol. 668, no. 1, pp. 20 – 23, 2008.

[14] D.-C. Dai, G. Starkman, D. Stojkovic, C. Issever, E. Rizvi, and J. Tseng, "Blackmax: A black-hole event generator with rotation, recoil, split branes, and brane tension," *Phys. Rev. D*, vol. 77, p. 076007, Apr 2008.

[15] D. Abercrombie *et al.*, "Dark Matter Benchmark Models for Early LHC Run-2 Searches: Report of the ATLAS/CMS Dark Matter Forum," 2015.

[16] A. Albert, M. Backovic, A. Boveia, O. Buchmueller, G. Busoni, A. De Roeck, C. Doglioni, I. John, T. DuPree, M. Fairbairn, M.-H. Genest, S. Gori, G. Gustavino, K. Hahn, U. Haisch, P. C. Harris, D. Hayden, V. Ippolito, F. Kahlhoefer, and M. Zinser, "Recommendations of the lhc dark matter working group: Comparing lhc searches for heavy mediators of dark matter production in visible and invisible decay channels," 03 2017.

[17] M. Chala, F. Kahlhoefer, M. McCullough, G. Nardini, and K. Schmidt-Hoberg, "Constraining dark sectors with monojets and dijets," *Journal of High Energy Physics*, vol. 2015, p. 89, Jul 2015.

[18] C. Alpigiani, "Searches for Dark Matter in ATLAS," Tech. Rep. ATL-PHYS-PROC-2017-112, CERN, Geneva, Aug 2017. Proceedings of the Fifth Annual LHCP.

[19] U. Baur, I. Hinchliffe, and D. Zeppenfeld, "Excited Quark Production at Hadron Colliders," *Int. J. Mod. Phys.*, vol. A2, p. 1285, 1987.

[20] U. Baur, M. Spira, and P. M. Zerwas, "Excited-quark and -lepton production at hadron colliders," *Phys. Rev. D*, vol. 42, pp. 815–824, Aug 1990.

[21] P. Langacker, R. W. Robinett, and J. L. Rosner, "New heavy gauge bosons in pp and $p\,\bar{p}$ collisions," *Phys. Rev. D*, vol. 30, pp. 1470–1487, Oct 1984.

[22] G. Altarelli, B. Mele, and M. Ruiz-Altaba, "Searching for New Heavy Vector Bosons in $p\bar{p}$ Colliders," *Z. Phys.*, vol. C45, p. 109, 1989. [Erratum: Z. Phys.C47,676(1990)].

[23] M. V. Chizhov, V. A. Bednyakov, and J. A. Budagov, "A unique signal of excited bosons in dijet data from pp collisions," *Physics of Atomic Nuclei*, vol. 75, pp. 90–96, Jan 2012.

[24] M. Chizhov and G. Dvali, "Origin and phenomenology of weak-doublet spin-1 bosons," *Physics Letters B*, vol. 703, no. 5, pp. 593 – 598, 2011.

[25] J. M. Campbell, J. W. Huston, and W. J. Stirling, "Hard interactions of quarks and gluons: a primer for lhc physics," *Reports on Progress in Physics*, vol. 70, no. 1, p. 89, 2007.

[26] G. D. S. Bethke and G. P. Salam, "Quantum chromodynamics."

[27] J. C. Collins and D. E. Soper, "The theorems of perturbative qcd," *Annual Review of Nuclear and Particle Science*, vol. 37, no. 1, pp. 383–409, 1987.

[28] A. D. Martin, W. J. Stirling, R. S. Thorne, and G. Watt, "Parton distributions for the LHC," *Eur. Phys. J.*, vol. C63, pp. 189–285, 2009.

[29] H.-L. Lai, M. Guzzi, J. Huston, Z. Li, P. M. Nadolsky, J. Pumplin, and C.-P. Yuan, "New parton distributions for collider physics," *Phys. Rev. D*, vol. 82, p. 074024, Oct 2010.

[30] R. D. Ball, V. Bertone, S. Carrazza, C. S. Deans, L. D. Debbio, S. Forte, A. Guffanti, N. P. Hartland, J. I. Latorre, J. Rojo, and M. Ubiali, "Parton distributions with lhc data," *Nuclear Physics B*, vol. 867, no. 2, pp. 244 – 289, 2013.

[31] G. Altarelli and G. Parisi, "Asymptotic Freedom in Parton Language," *Nucl. Phys.*, vol. B126, pp. 298–318, 1977.

[32] J. P. Ellis, "Tikz-feynman: Feynman diagrams with tikz," *Computer Physics Communications*, vol. 210, no. Supplement C, pp. 103 – 123, 2017.

[33] A. Khalil and W. A. Horowitz, "Initial state factorization and the kinoshita-lee-nauenberg theorem," *Journal of Physics: Conference Series*, vol. 889, no. 1, p. 012002, 2017.

[34] B. R. Webber, "Fragmentation and hadronization," *Int. J. Mod. Phys.*, vol. A15S1, pp. 577–606, 2000. [eConfC990809,577(2000)].

[35] B. Andersson, G. Gustafson, G. Ingelman, and T. Sjostrand, "Parton Fragmentation and String Dynamics," *Phys. Rept.*, vol. 97, pp. 31–145, 1983.

[36] S. Höche, "Introduction to parton-shower event generators," in *Proceedings, Theoretical Advanced Study Institute in Elementary Particle Physics: Journeys Through the Precision Frontier: Amplitudes for Colliders (TASI 2014): Boulder, Colorado, June 2-27, 2014*, pp. 235–295, 2015.

[37] L. Evans and P. Bryant, "LHC Machine," *JINST*, vol. 3, p. S08001, 2008.

[38] C. Lefèvre, "The CERN accelerator complex. Complexe des accélérateurs du CERN." Dec 2008.

[39] P. L. Rocca and F. Riggi, "The upgrade programme of the major experiments at the large hadron collider," *Journal of Physics: Conference Series*, vol. 515, no. 1, p. 012012, 2014.

[40] A. Collaboration, "The atlas experiment at the cern large hadron collider," *Journal of Instrumentation*, vol. 3, no. 08, p. S08003, 2008.

[41] A. Collaboration, "Luminosity public results."

[42] U. Mets501, "Pseudorapidity." CC BY-SA 3.0, July 2012.

[43] *ATLAS inner detector: Technical Design Report, 1.* Technical Design Report ATLAS, Geneva: CERN, 1997.

[44] M. S. Alam *et al.*, "ATLAS pixel detector: Technical design report," 1998.

[45] M. Capeans, G. Darbo, K. Einsweiller, M. Elsing, T. Flick, M. Garcia-Sciveres, C. Gemme, H. Pernegger, O. Rohne, and R. Vuillermet, "ATLAS Insertable B-Layer Technical Design Report," Tech. Rep. CERN-LHCC-2010-013. ATLAS-TDR-19, Sep 2010.

[46] "Alignment of the ATLAS Inner Detector and its Performance in 2012," Tech. Rep. ATLAS-CONF-2014-047, CERN, Geneva, Jul 2014.

[47] *ATLAS liquid-argon calorimeter: Technical Design Report.* Technical Design Report ATLAS, Geneva: CERN, 1996.

[48] *ATLAS tile calorimeter: Technical Design Report.* Technical Design Report ATLAS, Geneva: CERN, 1996.

[49] K. Sliwa, ""ATLAS Overview and Main Results"," in *Proceedings, International School on High Energy Physics : Workshop on High Energy Physics in the near Future. (LISHEP 2013): Rio de Janeiro, Brazil, March 17-24, 2013*, 2013.

[50] A. Straessner, "The atlas liquid argon calorimeter read-out system," in *14th IEEE-NPSS Real Time Conference, 2005.*, pp. 5 pp.–, June 2005.

[51] W. W. Armstrong *et al.*, "ATLAS: Technical proposal for a general-purpose p p experiment at the Large Hadron Collider at CERN," 1994.

[52] A. A. et. al., "The atlas forward calorimeter," *Journal of Instrumentation*, vol. 3, no. 02, p. P02010, 2008.

[53] J. Snuverink, *The ATLAS Muon Spectrometer: Commissioning and Tracking.* PhD thesis, Twente U., Enschede, 2009.

[54] R. Voss and J. W. (CERN), eds., *ATLAS Muon Spectrometer Technical Design Report.* Technical Design Report ATLAS, Geneva: CERN, May 1997.

[55] F. Bauer *et al.*, "Construction and Test of MDT Chambers for the ATLAS Muon Spectrometer," *Nucl. Instrum. Meth.*, vol. A461, pp. 17–20, 2001.

[56] T. Argyropoulos, K. A. Assamagan, B. H. Benedict, V. Chernyatin, E. Cheu, J. Deng, A. Gordeev, I. G. Eschrich, V. Grachev, K. Johns, S. Junnarkar, A. Kandasamy, V. Kaushik, A. Khodinov, A. Lankford, X. Lei, R. M. Garcia, K. Nikolopoulos, P. O'Connor, C. L. Parnell-Lampen, W. Park, V. Polychronakos, R. Porter, M. Purohit, M. Schernau, B. K. Toggerson, and D. Tompkins, "Cathode strip chambers in atlas : Installation, commissioning and in situ performance," in *2008 IEEE Nuclear Science Symposium Conference Record*, pp. 2819–2824, Oct 2008.

[57] S. Majewski, G. Charpak, A. Breskin, and G. Mikenberg, "A thin multiwire chamber operating in the high multiplication mode," *Nuclear Instruments and Methods in Physics Research*, vol. 217, no. 1, pp. 265 – 271, 1983.

[58] G. Aielli *et al.*, "The RPC first level muon trigger in the barrel of the ATLAS experiment," *Nucl. Phys. Proc. Suppl.*, vol. 158, pp. 11–15, 2006. [,11(2006)].

[59] *ATLAS level-1 trigger: Technical Design Report*. Technical Design Report ATLAS, Geneva: CERN, 1998.

[60] R. Blair, J. Dawson, G. Drake, W. Haberichter, J. Schlereth, J. Zhang, M. Abolins, Y. Ermoline, and B. Pope, "The ATLAS High Level Trigger Region of Interest Builder," *Journal of Instrumentation*, vol. 3, p. 04001, Apr. 2008.

[61] W. Wiedenmann and the Atlas Collaboration, "The atlas online high level trigger framework: Experience reusing offline software components in the atlas trigger," *Journal of Physics: Conference Series*, vol. 219, no. 2, p. 022024, 2010.

[62] M. Cacciari, G. P. Salam, and G. Soyez, "The anti- k t jet clustering algorithm," *Journal of High Energy Physics*, vol. 2008, no. 04, p. 063, 2008.

[63] A. Collaboration, "Topological cell clustering in the atlas calorimeters and its performance in lhc run 1," *The European Physical Journal C*, vol. 77, p. 490, Jul 2017.

[64] "2015 start-up trigger menu and initial performance assessment of the ATLAS trigger using Run-2 data," Tech. Rep. ATL-DAQ-PUB-2016-001, CERN, Geneva, Mar 2016.

[65] T. Sjostrand, S. Mrenna, and P. Z. Skands, "A Brief Introduction to PYTHIA 8.1," *Comput. Phys. Commun.*, vol. 178, pp. 852–867, 2008.

[66] "ATLAS Run 1 Pythia8 tunes," Tech. Rep. ATL-PHYS-PUB-2014-021, CERN, Geneva, Nov 2014.

[67] S. A. et al., "Geant4—a simulation toolkit," *Nuclear Instruments and Methods in Physics Research Section A: Accelerators, Spectrometers, Detectors and Associated Equipment*, vol. 506, no. 3, pp. 250 – 303, 2003.

[68] A. Collaboration, "The atlas simulation infrastructure," *Eur. Phys. J. C*, vol. 70, no. 3, pp. 823–874, 2010.

[69] *ATLAS Computing: technical design report*. Technical Design Report ATLAS, Geneva: CERN, 2005.

[70] J. Alwall, R. Frederix, S. Frixione, V. Hirschi, F. Maltoni, O. Mattelaer, H. S. Shao, T. Stelzer, P. Torrielli, and M. Zaro, "The automated computation of tree-level and next-to-leading order differential cross sections, and their matching to parton shower simulations," *JHEP*, vol. 07, p. 079. 158 p, May 2014. Comments: 158 pages, 27 figures; a few references have been added.

[71] W.-K. Tung, "New generation of parton distributions with uncertainties from global QCD analysis," *Acta Phys. Polon.*, vol. B33, pp. 2933–2938, 2002. [,199(2002)].

[72] A. Belyaev, N. D. Christensen, and A. Pukhov, "CalcHEP 3.4 for collider physics within and beyond the Standard Model," *Comput. Phys. Commun.*, vol. 184, pp. 1729–1769, 2013.

[73] S. Catani, Y. L. Dokshitzer, M. H. Seymour, and B. R. Webber, "Longitudinally invariant K_t clustering algorithms for hadron hadron collisions," *Nucl. Phys.*, vol. B406, pp. 187–224, 1993.

[74] Y. Dokshitzer, G. Leder, S. Moretti, and B. Webber, "Better jet clustering algorithms," *Journal of High Energy Physics*, vol. 1997, no. 08, p. 001, 1997.

[75] A. Collaboration, "Jet energy measurement with the atlas detector in proton-proton collisions at $\sqrt{s} = 7$ tev," *The European Physical Journal C*, vol. 73, p. 2304, Mar 2013.

[76] A. Collaboration, "Monte Carlo Calibration and Combination of In-situ Measurements of Jet Energy Scale, Jet Energy Resolution and Jet Mass in ATLAS," 2015.

[77] T. Barillari, E. Bergeaas Kuutmann, T. Carli, J. Erdmann, P. Giovannini, K. J. Grahn, C. Issever, A. Jantsch, A. Kiryunin, K. Lohwasser, A. Maslennikov, S. Menke, H. Oberlack, G. Pospelov, E. Rauter, P. Schacht, F. Spanó, P. Speckmayer, P. Stavina, and P. Strízenec, "Local Hadronic Calibration," Tech. Rep. ATL-LARG-PUB-2009-001-2. ATL-COM-LARG-2008-006. ATL-LARG-PUB-2009-001, CERN, Geneva, Jun 2008. Due to a report-number conflict with another document, the report-number ATL-LARG-PUB-2009-001-2 has been assigned.

[78] A. Collaboration, "Pile-up subtraction and suppression for jets in ATLAS," 2013.

[79] M. Cacciari and G. P. Salam, "Pileup subtraction using jet areas," *Physics Letters B*, vol. 659, no. 1, pp. 119 – 126, 2008.

[80] A. Collaboration, "Jet energy scale measurements and their systematic uncertainties in proton-proton collisions at $\sqrt{s} = 13$tev with the atlas detector," *Phys. Rev. D*, vol. 96, p. 072002, Oct 2017.

[81] "Tagging and suppression of pileup jets with the ATLAS detector," Tech. Rep. ATLAS-CONF-2014-018, CERN, Geneva, May 2014.

[82] A. Collaboration, "Jet global sequential corrections with the ATLAS detector in proton-proton collisions at $\sqrt{s} = 8$ TeV," 2015.

[83] "Data-driven determination of the energy scale and resolution of jets reconstructed in the ATLAS calorimeters using dijet and multijet events at $\sqrt{s} = 8\ TeV$," Tech. Rep. ATLAS-CONF-2015-017, CERN, Geneva, Apr 2015.

[84] A. Collaboration, "Determination of the jet energy scale and resolution at ATLAS using Z/γ–jet events in data at $\sqrt{s} = 8$ TeV," 2015.

[85] A. Collaboration, "Jet energy measurement and its systematic uncertainty in proton-proton collisions at $\sqrt{s} = 7$ TeV with the ATLAS detector," *Eur. Phys. J.*, vol. C75, p. 17, 2015.

[86] A. Collaboration, "A measurement of single hadron response using data at s=8tev with the atlas detector," Tech. Rep. ATL-PHYS-PUB-2014-002, CERN, Geneva, Mar 2014.

[87] A. Collaboration, "Single hadron response measurement and calorimeter jet energy scale uncertainty with the atlas detector at the lhc," *The European Physical Journal C*, vol. 73, p. 2305, Mar 2013.

[88] A. Collaboration, "A measurement of the calorimeter response to single hadrons and determination of the jet energy scale uncertainty using LHC Run-1 *pp*-collision data with the ATLAS detector," *Eur. Phys. J.*, vol. C77, no. 1, p. 26, 2017.

[89] D. Boerner, "A method for the construction of strongly reduced representations of ATLAS experimental uncertainties and the application thereof to the jet energy scale," Tech. Rep. ATL-PHYS-PROC-2016-272, CERN, Geneva, Oct 2016.

[90] A. Collaboration, "Jet energy resolution in proton-proton collisions at $\sqrt{s} = 7$tev recorded in 2010 with the atlas detector," *The European Physical Journal C*, vol. 73, p. 2306, Mar 2013.

[91] "Selection of jets produced in 13TeV proton-proton collisions with the ATLAS detector," Tech. Rep. ATLAS-CONF-2015-029, CERN, Geneva, Jul 2015.

[92] "Search for new phenomena in dijet events with the atlas detector at s=13 tev using 2015 and 2016 data," Tech. Rep. ATL-COM-PHYS-2016-1495, CERN, Geneva, 2016 2016.

[93] R. M. HARRIS and K. KOUSOURIS, "Searches for dijet resonances at hadron colliders," *International Journal of Modern Physics A*, vol. 26, no. 30n31, pp. 5005–5055, 2011.

[94] A. Collaboration, "Search for new phenomena in dijet mass and angular distributions from *pp* collisions at $\sqrt{s} = 13$ TeV with the ATLAS detector," *Phys. Lett.*, vol. B754, pp. 302–322, 2016.

[95] "Search for new phenomena in dijet events with the atlas detector at $\sqrt{s} = 13$ tev with the full 2015 dataset," Tech. Rep. ATL-COM-PHYS-2015-1205, CERN, Geneva, Sep 2015.

[96] T. Aaltonen *et al.*, "Search for new particles decaying into dijets in proton-antiproton collisions at s**(1/2) = 1.96-TeV," *Phys. Rev.*, vol. D79, p. 112002, 2009.

[97] A. Collaboration, "Search for new particles in two-jet final states in 7 tev proton-proton collisions with the atlas detector at the lhc," *Phys. Rev. Lett.*, vol. 105, p. 161801, Oct 2010.

[98] C. Collaboration, "Search for resonances in the dijet mass spectrum from 7 tev pp collisions at cms," *Physics Letters B*, vol. 704, no. 3, pp. 123 – 142, 2011.

[99] A. Collaboration, "A search for new physics in dijet mass and angular distributions in pp collisions at $\sqrt{s} = 7$tev measured with the atlas detector," *New Journal of Physics*, vol. 13, no. 5, p. 053044, 2011.

[100] A. Collaboration, "Search for new phenomena in the dijet mass distribution using $p-p$ collision data at $\sqrt{s} = 8$ TeV with the ATLAS detector," *Phys. Rev.*, vol. D91, no. 5, p. 052007, 2015.

[101] A. M. Sirunyan *et al.*, "Search for dijet resonances in proton–proton collisions at $\sqrt{s}$ = 13 TeV and constraints on dark matter and other models," *Phys. Lett.*, vol. B769, pp. 520–542, 2017. [Erratum: Phys. Lett.B772,882(2017)].

[102] F. James and M. Roos, "Minuit: A System for Function Minimization and Analysis of the Parameter Errors and Correlations," *Comput. Phys. Commun.*, vol. 10, pp. 343–367, 1975.

[103] G. Choudalakis, "On hypothesis testing, trials factor, hypertests and the BumpHunter," in *Proceedings, PHYSTAT 2011 Workshop on Statistical Issues Related to Discovery Claims in Search Experiments and Unfolding, CERN,Geneva, Switzerland 17-20 January 2011*, 2011.

[104] E. Gross and O. Vitells, "Trial factors or the look elsewhere effect in high energy physics," *Eur. Phys. J.*, vol. C70, pp. 525–530, 2010.

[105] G. Choudalakis and D. Casadei, "Plotting the differences between data and expectation," *The European Physical Journal Plus*, vol. 127, p. 25, Feb 2012.

[106] A. Collaboration, "Search for new phenomena in dijet events using $37 fb^{-1}$ of pp collision data collected at $\sqrt{s} = 13$tev with the atlas detector," *Phys. Rev. D*, vol. 96, p. 052004, Sep 2017.

[107] A. Collaboration, "Luminosity determination in pp collisions at $\sqrt{s} = 8$ tev using the atlas detector at the lhc," *The European Physical Journal C*, vol. 76, p. 653, Nov 2016.

[108] S. van der Meer, "Calibration of the Effective Beam Height in the ISR," 1968.

[109] J. Heinrich, C. Blocker, J. Conway, L. Demortier, L. Lyons, G. Punzi, and P. K. Sinervo, "Interval estimation in the presence of nuisance parameters. 1. Bayesian approach," 2004.

[110] L. E. Eberly and G. Casella, "Estimating bayesian credible intervals," *Journal of Statistical Planning and Inference*, vol. 112, no. 1, pp. 115 – 132, 2003. Special issue II: Model Selection, Model Diagnostics, Empirical B ayes and Hierarchical Bayes.

[111] A. Caldwell, D. Kollár, and K. Kröninger, "Bat – the bayesian analysis toolkit," *Computer Physics Communications*, vol. 180, no. 11, pp. 2197 – 2209, 2009.

[112] N. Metropolis and S. Ulam, "The monte carlo method," *Journal of the American Statistical Association*, vol. 44, no. 247, pp. 335–341, 1949. PMID: 18139350.

[113] "Search for new light resonances decaying to jet pairs and produced in association with a photon or a jet in proton-proton collisions at $\sqrt{s} = 13$ TeV with the ATLAS detector," Tech. Rep. ATLAS-CONF-2016-070, CERN, Geneva, Aug 2016.

[114] "Search for light dijet resonances with the ATLAS detector using a Trigger-Level Analysis in LHC pp collisions at $\sqrt{s} = 13$ TeV," Tech. Rep. ATLAS-CONF-2016-030, CERN, Geneva, Jun 2016.

[115] C. E. Rasmussen and C. K. Williams, *Gaussian processes for machine learning*, vol. 1. MIT press Cambridge, 2006.

[116] S. Golchi and R. Lockhart, "A bayesian search for the higgs particle," *arXiv preprint arXiv:1501.02226*, 2015.

[117] A. Collaboration, "Measurement of dijet cross sections in *pp* collisions at 7 TeV centre-of-mass energy using the ATLAS detector," *JHEP*, vol. 05, p. 059, 2014.

[118] S. Alioli *Private Communication*, 2017.

[119] S. Alioli, M. Farina, D. Pappadopulo, and J. T. Ruderman, "Precision Probes of QCD at High Energies," *JHEP*, vol. 07, p. 097, 2017.

[120] S. Alioli, P. Nason, C. Oleari, and E. Re, "A general framework for implementing NLO calculations in shower Monte Carlo programs: the POWHEG BOX," *JHEP*, vol. 06, p. 043, 2010.

[121] S. Alioli, K. Hamilton, P. Nason, C. Oleari, and E. Re, "Jet pair production in POWHEG," *JHEP*, vol. 04, p. 081, 2011.

[122] R. D. Ball *et al.*, "Parton distributions for the LHC Run II," *JHEP*, vol. 04, p. 040, 2015.

[123] D. Foreman-Mackey, D. W. Hogg, D. Lang, and J. Goodman, "emcee: The mcmc hammer," *Publications of the Astronomical Society of the Pacific*, vol. 125, no. 925, p. 306, 2013.

[124] J. Goodman and J. Weare, "Ensemble samplers with affine invariance," *Communications in applied mathematics and computational science*, vol. 5, no. 1, pp. 65–80, 2010.

[125] M. N. Gibbs, *Bayesian Gaussian processes for regression and classification*. PhD thesis, University of Cambridge Cambridge, England, 1998.

[126] S. Ambikasaran, D. Foreman-Mackey, L. Greengard, D. W. Hogg, and M. O'Neil, "Fast Direct Methods for Gaussian Processes and the Analysis of NASA Kepler Mission Data," 2014.

[127] S.S. Wilks, "The large-sample distribution of the likelihood ratio for testing composite hypotheses," *Ann. Math. Statist.*, vol. 9, pp. 60–62, 1938.

[128] B. C. Allanach *et al.*, "The Snowmass points and slopes: Benchmarks for SUSY searches," *Eur. Phys. J.*, vol. C25, pp. 113–123, 2002.

[129] O. Vitells and E. Gross, "Estimating the significance of a signal in a multi-dimensional search," *Astropart. Phys.*, vol. 35, pp. 230–234, 2011.

[130] R. B. Davies, "Hypothesis testing when a nuisance parameter is present only under the alternative," *Biometrika*, vol. 74, no. 1, pp. 33–43, 1987.